Validation and Extension of Emissivity and Reflectivity Models for Forests at Microwave Application to ESA SMOS Mission

by Rachid Rahmoune

Department of Computer Science, Systems and Production

University of Rome Tor Vergata, Italy

Submitted in total fulfilment of the requirements of the degree of

Doctor of Philosophy

January 2011

Supervisor: Prof. Paolo ferrazzoli

Co-Supervisor: Prof. Leila Guerriero

thesis committee: Prof. Domenico Solimini

Dr. Simonetta Paloscia

Dr.

Dr.

Day of the defense:

Signature from head of PhD committee:

Abstract

Soil moisture in the top few meters of the Earth's surface has an important role in regulating the energy and water balance at the soil surface and it is therefore a crucial variable for many environmental disciplines which are concerned with atmospheric and land surface processes such as meteorology, hydrology and climatology. Passive microwave data at L-band (1.4 GHz,21cm wavelength) measurements are shown to be a very effective observation for surface soil moisture retrieval. The first space-borne L-band mission dedicated to observing soil moisture, the European Space Agencys (ESA) Soil Moisture and Ocean Salinity (SMOS) mission, was launched on 2nd November 2009. SMOS carry an L-band (1.4GHz) microwave radiometer and is providing near-surface soil moisture estimates with global coverage, three-days revisit time and spatial resolution of approximately 40km. Due to this coarse spatial resolution, significant spatial heterogeneity in land surface conditions will exist within SMOS footprints. The soil moisture retrieval algorithm adopted for SMOS partially accounts for the land surface heterogeneity by modeling the microwave emission of different fractions of the footprint having different vegetation types.

The principal objectives of this research are to (i) test and improve the existing microwave models for the emission of natural surfaces, specially the forest modeling and exploitation the potential of SMOS radiometers to monitor the moisture of forest covered soils. (ii) investigate the sensitivity of L-band signal above forests to below-canopy and surface variables such as soil moisture, and litter and understory biomass and water content which could aid in future studies on the ecology and hydrological state of the canopy and understory.

Aircrafts and ground datas used in this study were collected during several campaigns and provided an unprecedented data set for investigation of passive microwave soil moisture remote sensing techniques, which puts this study in the forefront of international research on this topic.

Before testing the SMOS algorithm at the SMOS footprint scale, in this study the core radiative transfer model of the algorithm is evaluated for the Australian conditions using high-resolution (62.5m) airborne data.

To my familly

God enrich me with knowledge. It's from Quran 20:114

Acknowledgements

Contents

List of Figures

List of Tables

Glossary

AF or EAF Array Factor or Equivalent Array Factor

AFP Antenna Foot Print

AMSR-E Advanced Microwave Scanning Radiometer - Earth Observing System

ASL Above Surface Layer

ATBD Algorithm Theoretical Baseline Document

DAP Data Analysis Product

DFFG Discrete Flexible Fine Grid

DFG Discrete Fine Grid

DGG Discrete Global Grid: the SMOS grid

ECMWF European Centre for Medium-range Weather Forecasting

ESA European Space Agency

FOV SMOS alias-free Field of View

L1c SMOS Level 1c processor or Data Products

L2 SMOS Level 2 processor or Data Products

LAI Leaf Area Index

LAI$_{Max}$ Maximum value of the LAI over one year for a forest stand

NAFE National Airborne Field Experiment

PLMR Polarimetric L-Band Multibeam Radiometer

RFI Radio Frequency Interference

RMSE Root Mean Square Error

RTE,RT Radiative Transfer Equation, Radiative Transfer

SM Soil volumetric Moisture content

SMPPD Soil Moisture Prototype Processor Development

TB Short notation for brightness temperatures

TGRD Table Generation Requirements Document

UDP User Data Product

SMOS Soil Moisture and Ocean Salinity

1

Introduction

This chapter describes the role of microwave remote sensing modeling to monitor soil and vegetation properties at global scale which is the subject of several studies in the recent decades. Special interest is given to the European Space Agency Soil Moisture and Ocean Salinity (SMOS) Mission, since this Ph.D Thesis has been performed as part of preparatory and commissioning activities for the Soil moisture retrieval algorithm.

1.1 Background

1.1.1 Monitoring soil moisture

Microwave remote sensing provides a unique capability for soil moisture estimation by measuring the electromagnetic radiation in the microwave region between 0.5 and 100 cm. The fundamental basis of microwave remote sensing for soil moisture is the large contrast between the dielectric properties of water (~ 80) and soil particles (< 4). As the moisture increases, the dielectric constant of the soil-water mixture increases, and this change is detectable by microwave sensors (Njoku and Kong, 1977; Dobson et al., 1985). Both passive and active microwave remote sensing techniques have demonstrated a promising ability for globally monitoring soil moisture variations.

Previous research has shown that passive microwave remote sensors can be used to monitor surface soil moisture over land surfaces (Eagleman and Lin, 1976; Ulaby et al., 1986; Schmugge and Jackson, 1994; Jackson et al., 1995; Wigneron et al., 2004). These sensors measure the intensity of microwave emission from the soil, which is proportional to the brightness temperature, a product of the surface temperature and emissivity. This observed

emission is related to its moisture content, due to the large differences in the dielectric constant of dry soil and water (Moran et al., 2004). Recent and near future spaceborne passive microwave sensors for soil moisture measurements include the Scanning Multichannel Microwave Radiometer (SMMR) on Nimbus-7, the Special Sensor Microwave/Imager (SSM/I) on Defense Meteorological Satellite Program (DMSP), the Tropical Rainfall Measuring Mission Microwave Imager (TRMM-TMI), the Advanced Microwave Scanning Radiometer-EOS (AMSR-E) on Aqua, the recent launched soil moisture and ocean salinity (SMOS) mission by the European Space Agency (ESA), and the upcoming NASA hydrospheric states (HYDROS) mission, and Soil Moisture Active and Passive (SMAP) mission.

A better understanding and modelling of the Earth climate implies a good knowledge of the global water cycle (Entekhabi et al., 1999). Although soil moisture is one of the main parameters used in climate models, in-situ measurements of soil moisture are sparse and their values are only representative of limited areas, since soil moisture temporal and spatial variation is large. SMOS will provide estimates of the soil moisture content in the top soil layer. This layer can be seen as the interface between the vegetation and the hydrological system: surface soil moisture determines hydrological processes such as evaporation, infiltration and run-off, while vadose zone soil moisture controls the uptake of water by the vegetation, as this unsaturated zone includes the root zone of the vegetation layer. Figure 1.1 illustrates this continuous water motion which is called the water (or hydrologic) cycle. Many works in the scientific literature conclude that mirowave radiometry at L-Band is optimal to estimate soil moisture, because the emissivity is sensitive to this variable, but also because it provides all-weather coverage, since the atmosphere at lower microwave frequencies may be considered nearly transparent, and vegetation is semi-transparent [Wang Choudry, 1981, Jackson Schmugge, 1991, 1995, Kerr et al., 2000].

1.1.2 Monitoring biomass and vegetation variables

The dielectric constant or permittivity of a material is a measure of its polarity and thus of its response to the electric field resulting from electromagnetic radiation. Below the frequency of 10 GHz, the dielectric constant of water is around 80, whereas that of a dry soil is about 3 and that of air is 1. The large difference between the permittivities of soil and water explains why microwaves are especially well-suited to monitor soil moisture content. The more water is present in the soil, the less the polar H2O molecules will be bound to the soil particles and the more they will be free to move about, thus increasing the dielectric constant of the

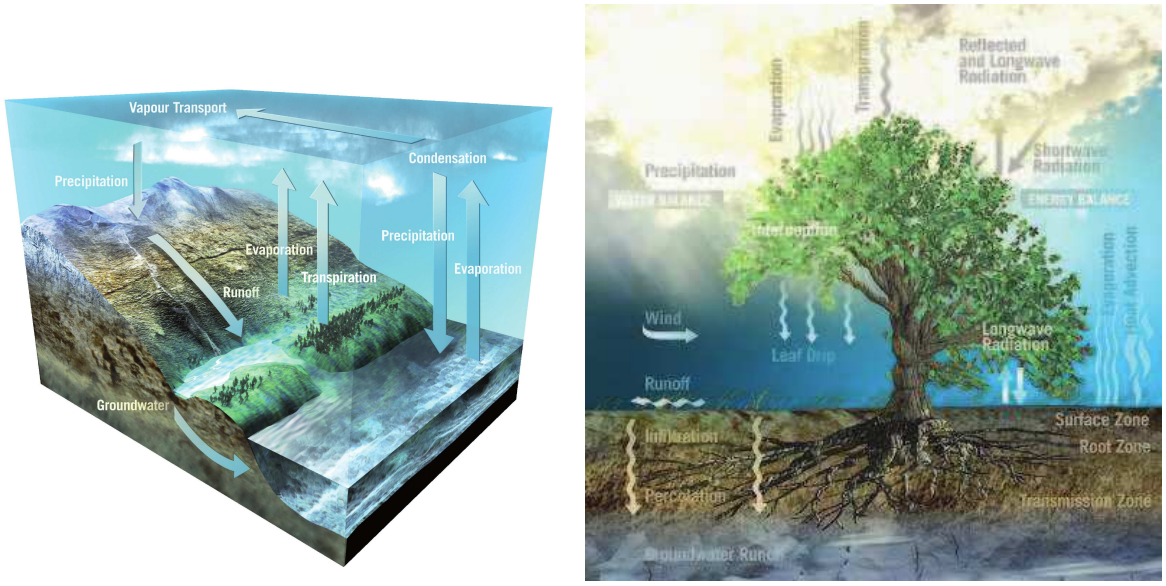

Figure 1.1: Earth's water cycle (credits: ESA)

soil medium. The L-band (1-2 GHz) frequency is especially well-suited to measure the water content of materials as the radiation frequency of the neutral hydrogen atom lies around 1.4 GHz.

Observed passive microwave radiation is expressed as brightness temperature (T_B), which depends on both the emissivity (e) and physical temperature (T) of the observed material. Soil and vegetation layers show different emission behaviours with increasing moisture, due to the different types of medium concerned in both cases. Because a soil layer forms a rather dense medium, so-called 'surface-effects' become more important in the radiative transfer. The main influence of H2O in soil is through an increase in dielectric constant, which reflects a change in the density of the soil medium relative to that of the air above, and thus an increase in reflectivity (R), which is related to emissivity by e = 1-R. If reflectivity at the soil-air interface becomes veryhigh, upwelling soil emission will become quite low. Thus, dry soil emission is very high ($\sim$ 0.8), but wet soil emission is much lower ($\sim$ 0.5), with exact values also depending on soil type.

A vegetation layer forms a much less dense medium than soil, and can be seen as a cloud of air, vegetation and water particles. In this case, 'volume effects' play a greater role. An increase in water content of this layer will have much less effect on the dielectric properties of the medium as a whole. Instead, vegetation emission will increase directly through the

increase of H2O molecules within the layer.

Besides emitting its own radiation, a vegetation layer will also affect the upwelling radiation emitted by the soil layer. Part of the soil emission will be transmitted through the vegetation volume, while the other part will be lost by scattering and absorption within the vegetation canopy.

1.1.3 The role of active, passive and bistatic systems

Recent advances in remote sensing have demonstrated the ability to measure the spatial variation of surface soil moisture under a variety of topographic and land cover conditions using both active and passive microwave measurements, each with its own strength and weakness. Active sensors, although having the capability to provide high spatial resolution in the order of tens of meters, have a poor resolution in time with repeat time excess of 1 month. On the other hand, the spaceborne passive systems can provide spatial resolutions only in the order of tens of kilometers but with a higher temporal resolution. In spite of the disadvantages of SAR or passive-based soil moisture retrieval, the ALOS-PALSAR and the proposed SMOS and SMAP mission offer the opportunity of retrieving soil moisture in a combined passive/active microwave approach, which is expected to increase the accuracy of the retrievals and can yield high-resolution soil moisture products.

Also, the bistatic systems GNSS-Reflectometry is gaining increasing interest in the remote sensing community. A Collection of GNSS signal reflections over land may represent a valuable tool to monitor the vegetation biomass, complementing the already well assessed capability of GNSS-R over the sea surface.

1.1.4 The contribution of physical models

A model may be defined as a relationship linking the radar output or the emissivity to the observation parameters (i.e., frequency, look angle, polar-ization) and to N surface variables. The backscattering coefficient

$$\sigma^0 = F(f, \theta, \psi_r, \chi_r, \psi_t, \chi_t, a_1, a_2, ..., a_N) \tag{1.1}$$

and the emissivity

$$\sigma^0 = G(f, \theta, \psi_r, \chi_r, \psi_t, \chi_t, a_1, a_2, ..., a_N) \tag{1.2}$$

are defined in several texts (Ulaby et al., 1986), f is the radar frequency, θ is the observation angle, ψ_r and χ_r are the rotation and ellipticity angle of the received electromagnetic field, ψ_t and χ_t, which are present only for the backscattering coefficient, are the rotation and ellipticity angle of the transmitted field (Ulaby and Elachi, 1990). The N variables (a_1 , a_2 and a_N) represent soil and vegetation properties. Variables influencing microwave measurements may be classified according to the scheme indicated below. Most of them may be used as inputs for models:

- Bare soils
  - Variable related to dielectric properties: permittivity $\epsilon_s = \epsilon'_s + j\epsilon''_s$, depending on soil moisture content (SMC), soil texture, bulk density, temperature and salinity.
  - Variables related to surface roughness: in a single-scale description, surface roughness is characterized by its autocorrelation function (ACF) and by two variables, such as height standard deviation and correlation length.
- Vegetation covered soils
  - The same soil variables defined above
  - Variables related to the amount of vegetation matter per unit area. The most commonly used are fresh biomass, plant water content (PWC) and plant density. For agricultural fields and the dry biomass for forests a correct description of electromagnetic effects, it is important to single out the fraction of vegetation components, such as stems, ears, leaves, pods, petioles for agricultural fields or trunks and branches for forests. For leaves, also the leaf area index (LAI) is often adopted.
  - Variable related to permittivity of vegetation elements: $\epsilon_v = \epsilon'_v + j\epsilon''_v$, related to gravimetric moisture, dry matter density,temperature and salinity.
  - Variables related to vegetation geometry: height and diameter for stems and trunks, length, width and thickness for leaves, and corresponding distributions of orientations are required.

1.1.5 Research objectives

Estimation of soil moisture from radiometric measurements is not simple since there are many soil and vegetation parameters affecting the land emission. The development of algorithms to compute bio/geophysical variables from brightness temperature measurements and the assessment of the impact of each of the involved parameters is crucial to have accurate soil moisture estimations.

This PhD research was done as part of the background research for the SMOS mission. At the spatial resolution of SMOS, many pixels over land will contain a certain percentage of forest cover. Forests usually consist of rather thick and dense vegetation layers. However modelling studies have shown that it might be possible to retrieve soil moisture with the required accuracy in moderately dense forests and parts of the pixel if forest emission can be modelled accurately. To this end, a discrete emission model at L-Band developed at Tor vergata University (Ferrazzoli and Guerriero 1996), was used to model forest emissivity at both polarization and several incidence angles. Then the physical model was used to calibrate the parameters of a simple radiative transfer model of first order, to be used in the SMOS retrieval algorithms.

These background aspects formed the motivation for this research and show the main goal of this work: to better understand and model forest emission properties at L-band in view of the SMOS mission. The focus hereby was on obtaining a greater knowledge of the angular and polarization dependence of the L-Band emissivity for various forest categories. A second objective was to investigate the sensitivity of the L-band signal above forests to below-canopy and surface variables such as soil moisture, and litter and understory biomass and water content. This could aid in future studies on the ecology and hydrological state of the canopy and understory.

To this end, emissivity values simulated by the model have been compared with values collected in the framework of several campaigns.

Field experiments were set up in Italy (Tuscany region) in summer 2000 and winter 2002, over various broadleaf forests, spanning a wide range of biomass. Model simulations reproduced well the main features of experimental data, such as the increasing trend of emissivity with biomass (at L-Band) and with frequency. The forest with lower biomass showed an appreciable seasonal variation of emissivity at L-Band, which was reproduced by the model only partially.

L-band measurements were made by the AMIRAS demonstrator in June 2006 over dense forests in Finland. In this case, inputs to the model were given on the basis of ECOCLIMAP. The absolute values of emissivity were well reproduced for both deciduous and coniferous forests, with a slight underestimation of the difference between V and H polarization.

Then a useful set of multitemporal airborne measurements were collected in the Eucalyptus forest of Roscommon, in Australia, in November 2005, in the framework of the NAFE 2005 campaign. The forest was moderately dense. Variations of soil moisture produced a variation of brightness temperature of about 20 k, which was reproduced by the model. Also measured values of polarization difference were in agreement with simulated ones.

These experiments formed a good inside point of this PhD research and was later followed up by additional AMSR-E and SMOS signatures at large scale for a variety of forest category around the world.

1.1.6 Organisation of the thesis

This Ph.D. Thesis focuses on forest emission modelling and soil moisture retrieval, and it is organised as follows:

Chapter 2 describes the properties of soils and vegetation, and revises the land emission models which are used at present in soil moisture retrieval algorithms from microwave remote sensing data.

Chapter 3 introduces and discusses the basic properties of Tor Vergata electromagnetic model, with the recent refinements introducing the new aspects on litter and soil. Then the theoretical model was tested against radiometric signatures collected in various forest sites.

Chapter 4 describes and explains the effects on selected AMSR-E channels of the rainstorm events, occurred in the Grand Chaco forest, Argentine.

Chapter 5 investigates the capability of SMOS MIRAS radiometer to monitor soil moisture over forests of South and North America, central Africa.

Chapter 6 reports some results of a study focused on the definition of an operational methodology to monitor routinely the calibration of the innovative instrument "Microwave Image Radiometer using Aperture Synthesis (MIRAS)" by investigating the possibility to use Amazon Rain forest as target to obtain long term information on the MIRAS instrument calibration stability.

Chapter 7 investigates the potential of GNSS-Reflectometry to monitor forest areas, using model simulations.

Chapter 8 Conclusions are presented, and future research lines exposed.

2

State of the art from microwave emission

This chapter describes the properties of soils and vegetation, and revises the land emission models which are used at present in soil moisture retrieval algorithms from microwave remote sensing data.

2.1 Emission from Land

Microwave remote sensing is based on the measurement of the thermal radiation or brightness temperature of a target, which is determined by its physical temperature and emissivity. The emissivity of land covers depends on soil moisture, but also on soil temperature [Choudhury et al., 1982, Wigneron et al., 2001, Holmes et al., 2006], soil surface roughness [Mo Schmugge, 1987, Wigneron et al., 2001, Escorihuela et al., 2007], vegetation canopy [Brunfeldt Ulaby, 1984, Jackson Schmugge, 1991, Ferrazzoli et al., 2002, Della Vecchia et al., 2006], snow cover [Schwank et al., 2004], relief [Matlzler Standley, 2000, Talone et al., 2007], etc.

During this PhD Thesis a series of comparisons between model simulations and experiental measurement were performed to determine the impact of some of the above mentioned parameters in the measured emission of land. The fundamentals of microwave emission from land covers are presented hereafter.

2.1.1 Bare Soils

Based on the energy conservation law, the emissivity is given by:

$$e_{gp} = 1 - r_{gp} \tag{2.1}$$

where r_{gp} is the total reflectivity. The uniform half space model with smooth surface is adopted. The total reflectivity in (2.2) is related to the reflection coefficient given by the Fresnel formulation:

$$r_{bH} = |\frac{\mu_s \cos\theta - \sqrt{\mu_s\epsilon_s - \sin^2\theta}}{\mu_s \cos\theta + \sqrt{\mu_s\epsilon_s - \sin^2\theta}}|^2, r_{bV} = |\frac{\epsilon_s \cos\theta - \sqrt{\mu_s\epsilon_s - \sin^2\theta}}{\epsilon_s \cos\theta + \sqrt{\mu_s\epsilon_s - \sin^2\theta}}|^2 \tag{2.2}$$

where μ_s is the soil magnetic permeability, assumed to be unity, ϵ_s is the complex, bare soil dielectric constant.

Then, for smooth bare soil, the up-welling soil brightness temperature may be written as a function of the soil effective temperature Tg and soil reflectivity r_{bp} computed from the Fresnel equation:

$$TB_p = (1 - r_{bp})T_g \tag{2.3}$$

According to the Dobson model and using the Peplinki's formulation, the dielectric constant of wet soil can be calculated as:

$$\epsilon_b = (1 + \frac{\rho_b}{\rho_s}(\epsilon_{pa}^{\alpha} - 1) + SM^{\beta'}\epsilon_{fw}^{'\alpha} - SM)^{\frac{1}{\alpha}} - j(SM^{\beta'}\epsilon_{fw}^{''\alpha})^{\frac{1}{\alpha}} \tag{2.4}$$

where

- ϵ_b=soil dielectric constant of the soil
- ρ_b= soil bulk density, and function of soil texture
- ρ_s= soil particle density, typically 2.664 gcm^-3, usually considered as constant
- dielectric constant of solid particles. For "normal" soils :

  $\epsilon_{pa} = (CPA_1 + CPA_2 * \rho_s)^2 + CPA_3$; yielding ϵ_{pa}=4.7
- $\alpha = 0.65$
- $\beta = \beta' - j\beta''$ is an empirically-derived complex function of soil texture parameter
- SM = soil moisture, volumetric water content of soil (m^3m^{-3})

- $\epsilon_{fw} = \epsilon'_{fw} - j\epsilon''_{fw}$ dielectric constant of free water

with

$$\epsilon'_{fw} = \epsilon_{w\,\mathrm{inf}} + \frac{\epsilon w0 - \epsilon_{w\,\mathrm{inf}}}{1 + (2\pi f r\tau_w)^2} \epsilon''_{fw} = \frac{2\pi f r\tau_w(\epsilon_{w0} - \epsilon w\,\mathrm{inf})}{1 + (2\pi f r\tau_w)^2} + \frac{\sigma_{eff}}{2\pi f\epsilon_0} \frac{\rho_s - \rho_b}{\rho_s SM} \tag{2.5}$$

where:

- ϵ_{w0} is the static dielectric constant of water
- $\epsilon_{w\,\mathrm{inf}}$ is the high frequency limit of the dielectric constant of water
- f is the frequency (Hz),
- $r\tau_w$ is the relaxation time of water,
- ϵ_0 is the permittivity of free space (8.854 10^{-12} Fm^{-1})

2.1.2 Soil surface roughness

When the surface is not flat and assuming that only surface scattering occurs, it is possible to estimate, from the flat bare surface reflectivity r_{bp}, an expression for the rough surface reflectivity r_{gp}. The most accepted formulation is an empirical relationship. As surface roughness increases, the angular signature of TB is affected, requiring to correct the Fresnel law with the following empirical phenomenological expression:

$$r_{gp}(\theta) = ((1 - Q_R)r_{bp} + Q_R r_{bq})exp(-H_R(SM)\cos^{N_{Rp}}(\theta)) \tag{2.6}$$

where

- Q_R is a polarization coupling factor, related to the fact that roughness tends to induce polarization mixing
- H_R is an effective surface roughness dimensionless parameter: $H_R = (2k\sigma)^2$ where k is the wave number, σ is the surface RMS height
- f is the frequency (Hz),
- N_{Rp} is an integer used to parameterize the dependence of the roughness effects on incidence angle.

- r_{bq} designates the smooth surface reflectivity for alternate polarisationq designates the smooth surface reflectivity for alternate polarisation

When the HR parameter is retrieved, then its reference value computed as indicated here will be used as a prior value in the retrieval scheme.

The value of N_{Rp} is found to be between 0 and 2 from experimental data [Wigneron et al, 2001] (originally, it was considered that N_{Rp}=2). Recent results indicated that the N_{Rp} exponent is also polarization dependent.

Polarization coupling effects are generally found to be rather weak at low frequencies. Therefore, it is often considered that Q_R=0 at L-band and this value increases slightly with increasing frequency [Wigneron et al, 2001].

2.1.3 Vegetation covered soil

The measured brightness temperature depends not only on the soil, but also on vegetation, since vegetation radiates its own energy and, moreover, attenuates and scatters the soil radiation. Chukhlantsev [2006] revised the theory and conducted experimental research over vegetated areas. The common practice is to use approximate formulas or semi-empirical models in which the different components of the brightness temperature could be differentiated. The emissivity of a soil covered by vegetation is usually estimated as the contribution of three terms:

- the radiation from the soil that is attenuated by the overlying vegetation
- the upward radiation from the vegetation
- the downward radiation from the vegetation, reflected by the soil, and attenuated by the canopy [Ulaby et al., 1986, p. 888]:

$$TB_p = (1-\omega)(1-\gamma)(1+\gamma r_{qp})T_c + (1-r_{gp})\gamma T_g \tag{2.7}$$

where T_g and T_c are the effective soil and vegetation temperatures, r_{qp} is the soil reflectivity, ω the single scattering albedo, γ the vegetation attenuation factor.

This last term can be computed from the nadir optical depth τ as:

$$\gamma_p = exp(\frac{-\tau}{\cos\theta}) \tag{2.8}$$

This formulation is known as the $\omega - \tau$ model Van de Griend and Wigneron [2004] and is based on the single scattering approach proposed in Kirdiashev et al. [1979]. The optical depth is related to the vegetation properties and the frequency. The single scattering albedo describes the scattering of the emitted radiation by the vegetation, and is a function of plant geometry.

2.1.4 Soil moisture retrieval algorithms

The brightness temperature of land covers is influenced by many variables,the most important being soil moisture and temperature, and vegetation characteristics. The challenge is to reconstruct the environmental parameters from the measured signal by using a minimum of ancillary data.

The basis approach was adopted in an ESA Study on soil moisture retrieval for SMOS . The principle is to find the best-suited set of soil moisture (SM) and vegetation characteristics by minimizing the differences between modelled and measured brightness temperature (TB) data.

$$CF = \frac{\sum_1^N (T_B^\circ(\theta, P) - T_B(\theta, P))^2}{\sigma_{T_B}^2} + \sum_1^n \frac{\sum_1^N (p_i - p_i^{ini})^2}{\sigma_{p_i}^2} \tag{2.9}$$

In the first term, T_B° indicates the measured value of T_B, P is polarization. In the second term, p_i is the value of the retrieved parameter and p_i^{ini} the initial value of each parameter in the retrieval process corresponding to an a priori estimate of a parameter p_i. σ^2 in the first term is the variance of the simulated values of T_B, σ^2 in the second term is a fixed variance which can be used to constrain the model to a greater or lesser degree.

2.1.5 Forest Studies

A better understanding of forest emission is important for Soil Moisture (SM) retrieval from spaceborne radiometers. Experiments using both ground based and airborne radiometers have provided an insight into the problem [Lang et al, 2001]-[Santi et al, 2001], but only a limited number of forests have been observed. Some experimental investigations, carried out over coniferous forests, or deciduous forests in cold climates, indicate that the effects of soil moisture variations on radiometric signatures are very low, even at L band [Guglielmetti et al, 2008], [Grant et al, 2007]. Other experiments in temperate climates indicate that a moderate sensitivity to variations of soil moisture exists, at least at L band [Santi et al, 2001], [Grant

et al, 2010], [Rahmoune et al, 2010]. Since definitive conclusions have not yet been reached, it is useful to make further investigations, covering a variety of climatic conditions and forest environments.

The objective of the present study is to better assess the potential of passive microwave radiometry to estimate land surface charecteristics in forest areas. Forests cover a very large part of the land surface and represent most of the terrestrial phytomass. Therefore, forest covers are an important component of the global carbon budget. Remote sensing observations can be used to monitor forest canopies over very large geographic areas, with a good temporal repetition. The penetration of depth of low frequency measurements can exceed the crown layer, and the scattering processes which contribute to Emission involve the crown layer (mostly branches), tree trunk and the ground surface.

Numerous studies have analysed to date the surface microwave emission for a variety of agricultural fields. Yet, few works have been carried out over forests at L-band. At that time, the possibility of retrieving soil moisture underneath forests or in partially forested areas was mostly evalueted on a few theoretical studies. Experimental observations were still lacking, especially long-term experimental data sets, which were virtually non-existent. These were necessary for validation of the then existing models and theoretical assumptions, and for calibration over forests in view of the SMOS mission. Long-term forest experiments at L-band were therefore started more or less simultaneously in France and Germany, while modelling work in Italy can provide a physically- based calibration (Ferrazzoli et al.2001). Comparable and complementary experiments have since also been conducted in the USA.

3

Microwave Modeling

The previous chapter has introduced an overview of the microwave modeling approaches used to monitor soil and vegetation properties. The present Chapter aims at giving more information about the electromagnetic model developed at Tor Vergata University, particulary for forests with the recent refinements introducing the new aspects on litter and soil. In the framework of SMOS project, a procedure has been developed to estimate the input dataset when only general information about forests is available. The reader will find the description of the theoretical approach used to model vegetation signatures collected by passive systems. Finally the theoretical model was tested against radiometric signatures collected in various forest sites.

3.1 Introduction

The model developed at the University of Rome "Tor Vergata" uses the radiative transfer theory to describe the interaction between the incoming electromagnetic wave and the vegetation (Bracaglia et al., 1995). It can compute both the backscattering coefficient (Ferrazzoli and Guerriero, 1995) and the emissivity (Ferrazzoli and Guerriero, 1996b) by using the energy conservation law. To represent the vegetation geometry, a discrete approach is adopted, and dielectric bodies with suitable shapes are used to describe the geometric properties. Figure 3.1 depicts both the scheme adopted to represent a generic forest.

Different assumptions about dimensions, orientations and dielectric properties of the scatteres can be done to distinguish different kinds of canopyes. The model is currently used to compute backscattering and emissvity for agricultural fields (Della Vecchia et al., 2006b) and

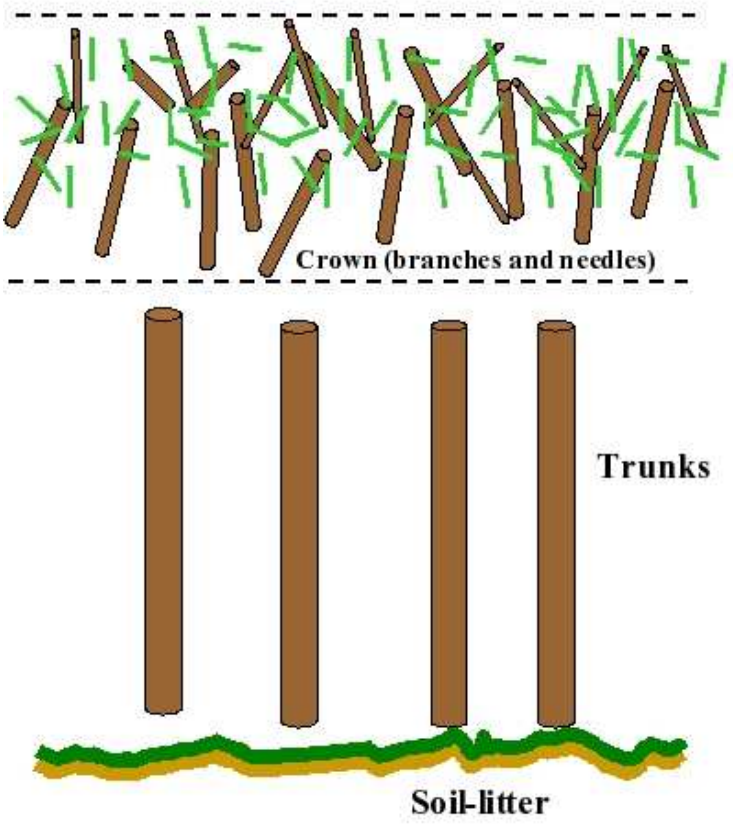

Figure 3.1: Example of geometric structure adopted for a generic vegetated soil. Forest sketch.

forests (Della Vecchia et al., 2006d, Della Vecchia et al., 2010). Once a geometric representation is chosen, the bistatic scattering and extintion coefficients for each scatterer are computed. Finally, all contributions are combined by means of the "Matrix Doubling Algorithm".

The model includes the multiple interactions among the different dielectric bodies which compose the vegetation and the soil. The last step consists in the assessment of the overall backscattering coefficient, for the active version of the model, or the emissivity for the passive one.

3.2 Model Description

This section provides further details about the model, in order to get a complete and exhaustive description of the theoretical formulation.

3.2.1 Single Scatterer Characterization

Similarly to other discrete models, the first step required by Tor Vergata Model (TVM) is detailed information about the geometric properties of the vegetation. After its decomposition into elementary components (leaves, petioles, stems for agricultural fields, or trunks, branches and leaves for forests) a detailed knowledge of the following variables is required:

- Geometric variables such as shape, dimension and orientation of ears, leaves, stems, branches and trunks.
- Permittivity values, which are related to moisture and dry matter density for vegetation, moisture and texture for soil
- Number of elements per unit area
- Soil variables such as moisture, surface height standard deviation and correlation length

First of all, the single elements are characterized. Due to the complex geometry, it is necessary to adopt some simplifications. The collection of suitable shapes adopted for the dielectric scatterers is a critical step. Furthermore, the choice of a reliable electromagnetic approximation is strictly correlated to the ratio between wavelength and scatterer dimensions. Mostly used single scatterer approximations are here reported

- Leaves are represented as discs and ellipses. It is possible to use the Rayleigh-Gans approximation (Eom and Fung, 1984), when at least one dimension of the scatterer is small with respect to the wavelength. For higher ratios between physical dimensions and wavelength, the physical optics approximation (Le Vine et al., 1983) is more reliable. Also the resistive approximation may be used.
- Cylinders may represent the stems, petioles, ears, trunks, branches and needles. The Rayleigh-Gans approximation can be used for thin cylinders, and the infinite length approximation (Karam and Fung, 1988) can be adopted when the length of the cylinder is much higher than the diameter.

- The soil is represented through a dielectric half-space with rough interface, and the integral equation model may be used to compute the bistatic scattering coefficient using the formulation of Fung (1994). For particulary smooth soils with respect to the wavelength, the small perturbation approximation is used, while the geometrical optics approximation is adopted for very rough, with respect to wavelength, surfaces.

3.2.2 Sublayer Characterization

To combine the interactions among the different dielectric scatterers which compose the vegetation, the numerical "Matrix Doubling" algorithm is used. This approach allows us to take into account the multiple scattering effects inside a volume filled with dielectric bodies. The idea is to divide the canopy layer into several sub-layers and then compute the multiple reflections among them. To characterize the scattering in the upper and lower half-spaces associated to the generic sublayer, as depicted in Figure 3.2, the electromagnetic behaviour of the dielectric bodies, which compose the sublayer, must first be characterized. To this aim, the scattering cross section matrix

$$\sigma = 4\pi \begin{pmatrix} < |f_{vv}|^2 > & < |f_{hv}|^2 > \\ < |f_{vh}|^> & < |f_{hh}|^2 > \end{pmatrix}$$

(3.1)

and the extinction cross section matrix are computed

$$\sigma_{\mathbf{e}} = 4\pi/k \begin{pmatrix} < \Im\{f_{vv}^F\} > & 0 \\ 0 & < \Im\{f_{hh}^F\} > \end{pmatrix}$$

(3.2)

k (m^-1) is the electromagnetic wave number, f_{vv}, f_{hv}, f_{vh}, f_{hh} are the scattering amplitude functions, averaged by considering the possible geometrical orientations of the single scatterer, described by the Eulerian angles α, λ and β. The forward scattering theorem is adopted to compute the extinction cross section, and the amplitude scattering function in the forward direction is used.

The scattering functions are continuous functions of the incident and scattering angles, but due to the enhanced computational complexity, this continuity is not kept by the algorithm.

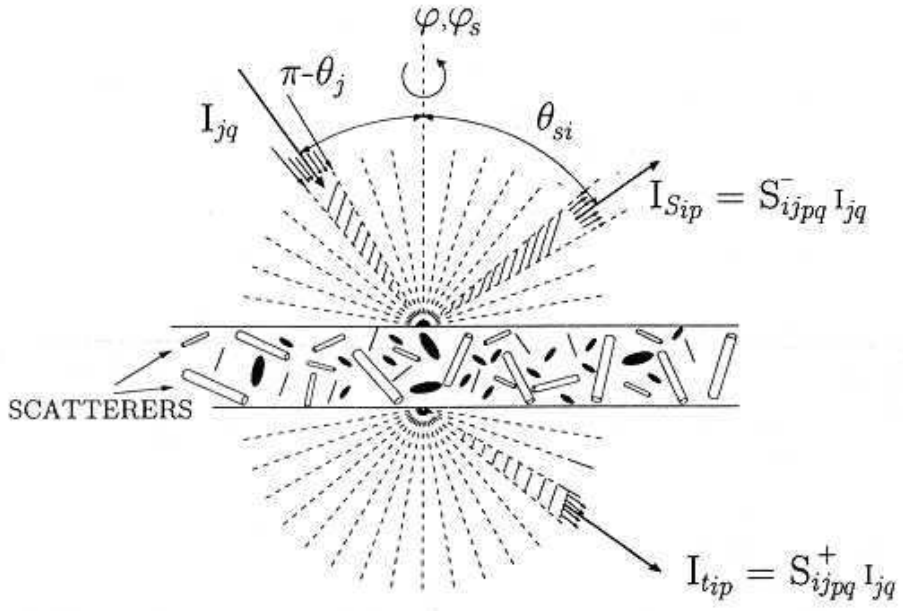

Figure 3.2: Scatter mechanism in the matrix doubling algorithm

A reasonable discretization of the space is mandatory in order to get an acceptable computing time. The discretization of the functions is obtained in the elevation plane, by subdividing the $\pi/2$ elevation range into N_θ intervals of width $\Delta\theta$, and the 2π azimuth range into Nϕ intervals of width $\Delta\phi$. In this way the incoming and scattered fields are belonging respectively to the jth and ith elevation interval ($1 \leq (i,j) \leq N\theta$), while ($\phi_s - \phi$) represents the difference between scattering and incident azimuth angles, with ($0 \leq (\phi_s - \phi) \leq 2\pi$).

Once the electromagnetic behaviour of all the elements, composing the sublayer, is known, it is possible to proceed to the second step, the sublayer electromagnetic characterization. To describe the scattering propreties the $\mathbf{S}^-$ and $\mathbf{S}^+$ matrices are adopted. The first one represents the upward scattering specific intensity I_{ip} ($\phi_s - \phi$) ($W/m^2 st$), in the i^{th} elevation angular interval and ϕ_s azimuthal angle, at p ($p = v, h$) polarization,due to an incident power, uniformly distributed within a cone of width $\Delta\theta \sin\theta$ dϕ of intensity $I_{jq}(\phi)$ ($W/m^2 st$), coming from the angular interval j^{th} with polarization q ($q = v, h$).

$$S^-_{ijpqm} = \frac{n\Delta z \Delta\theta \sin\theta_j}{4\pi \cos\theta_{si}} . a_m F_m \{\sigma^-_{ijpq}(\phi_s - \phi)\} \tag{3.3}$$

$$S^{+}_{ijpqm} = \frac{n\Delta z \Delta\theta \sin\theta_j}{4\pi \cos\theta_{si}} . a_m F_m\{\sigma^{+}_{ijpq}(\phi_s - \phi)\} \tag{3.4}$$

A further hypothesis of independence, among the scatterers belonging to the same volume of thickness Δz, make of the elements of Stokes matrix directly proportional to the scatterers density n (m^{-3}). The F_m {} indicates the m^{th} term of Fourier series, adopted to express the dependence on $\phi_s - \phi$, and a_m represents the Fourier coefficient, which is equal to 2π for the zero-th order term and π for the higher ones. By means of a readjustment of the previous matrices, a further form is proposed for both of them in equation (3.5).

$$\mathbf{S^{\pm}_{m}} = \begin{bmatrix} \mathbf{S^{\pm}_{vvm}} & \mathbf{S^{\pm}_{vhm}} \\ \mathbf{S^{\pm}_{hvm}} & \mathbf{S^{\pm}_{hhm}} \end{bmatrix} \tag{3.5}$$

where $\mathbf{S^{\pm}_{pqm}}$, whose dimension is 2 N_θ $\times$N$_\theta$, contain the $\mathbf{S^{\pm}_{ij}}$ coefficients for each polarization pair. In order to consider the overall electromagnetic interaction, it is needed to estimate the electromagnetic field which propagates through the vegetation. Thus, the transmission matrix is represented in equation (3.6).

$$\mathbf{T^{+}} = \mathbf{1} - \begin{bmatrix} \mathbf{k_{evv}} & 0 \\ 0 & \mathbf{k_{ehh}} \end{bmatrix} \tag{3.6}$$

The elements of the transmission matrix, of dimention $2N_\theta \times 2N_\theta$, are obtained directly from the extinction matrix, equation (3.2), and they are expressed as

$$k_{ejjpq} = \frac{n\Delta z}{\cos\theta_j} \sigma_{eijpq} \tag{3.7}$$

Once the sublayer downward scattering matrix $\mathbf{S^{+}_{m}}$ is substituted by the transmission matrix expressed as $\mathbf{T_m} = \mathbf{S^{+}_{m}} + \mathbf{T^{+}_{m}}$, and the matrix scattering in the upward direction is known, the single sublayer characterization is completed.

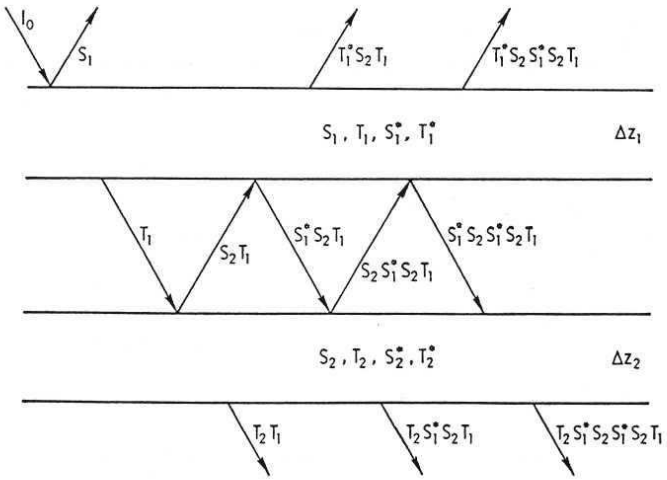

Figure 3.3: Multiple reflections among sublayers

3.2.3 Matrix Doubling Algorithm

In order to take into account the multiple interactions among several sublayers, the approach proposed by Eom and Fung (1984) is adopted. In Figure 3.3 all possible paths that the energy fluxes can follow, are depicted. The total upward scattering of two sublayers is expressed as:

$$\mathbf{S_m} = \mathbf{S_{1m}}+\mathbf{T_{1m}^*S_{2m}T_{1m}}+\mathbf{T_{1m}^*S_{2m}S_{1m}^*S_{2m}T_{1m}}+... = \mathbf{S_{1m}}+\mathbf{T_{1m}^*S_{2m}}(\mathbf{I}-\mathbf{S_{1m}^*S_{2m}})^{-\mathbf{1}}\mathbf{T_{1m}} \tag{3.8}$$

whereas the total downward scattering and transmission matrices are obtained by means of the following expression

$$\mathbf{T_m} = \mathbf{T_{2m}}[\mathbf{I}+\mathbf{S_{1m}^*S_{2m}}+(\mathbf{S_{1m}^*S_{2m}})^{\mathbf{2}}+...]\mathbf{T_{1m}} = \mathbf{T_{2m}}(\mathbf{I}-\mathbf{S_{1m}^*S_{2m}})^{-\mathbf{1}}\mathbf{T_{1m}} \tag{3.9}$$

In the evaluation of the matrices it is assumed that the impinging field comes from the upper half-space, whereas, for started matrices an impinging field coming from the lower half-space is assumed. If each sublayer is symmetric, $\mathbf{S}^* = \mathbf{S}$ and $\mathbf{T}^* = \mathbf{T}$. The whole canopy scaterring matrix $\mathbf{S_{vm}}$ and transmissivity matrix $\mathbf{T_{vm}}$ are computed for all the Fourier terms, by reiteration of the procedure.

3.2.4 Backscattering Coefficient Computation

Once the scattering and attenuation properties of the canopy are known, and represented as shown in 3.2.2, it is possible to proceed with the last step, i.e. the estimation of the overall backscattering coefficient. To this aim the matrix doubling algorithm is used again, but now between the vegetation layer and the soil, which shows only one upward scattering matrix. So, the following procedure is observed

$$\mathbf{S_{vgm}} = \mathbf{S_{vm}} + \mathbf{T^*_{vm}}\mathbf{S_{gm}}(\mathbf{I} - \mathbf{S^*_{vm}}\mathbf{S_{gm}})^{-\mathbf{1}}\mathbf{T_{vm}} \tag{3.10}$$

where $\mathbf{S_{vm}}$ and $\mathbf{T_{vm}}$ represent the upward and downward scattering matrices of the whole vegetation layer, whereas $\mathbf{S_{gm}}$ represents the bistatic scattering of the soil. Since all the matrices are in the Fourier domain, an inverse transformation is needed, which allows us to come back to the original system. The equation (3.11) shows the procedure

$$\sigma^o_{jjpq} = \frac{4\pi}{\Delta\theta}\cot\theta_j \sum_{m=0}^{N_\phi/2+1} \frac{1}{a_m}\mathbf{S_{vgjjpqm}}\cos(\mathbf{m}(\phi_\mathbf{s} - \phi)) \tag{3.11}$$

where $\phi_s - \phi$ is the generic azimuthal scattering angle, and in the particular case of backscattering it is equal to π.

3.2.5 Emissivity Computation

A previously mentioned, the model may be used to estimate the scattering, in all directions. In the previous section, the backscattering computation has been shown, but similar expressions can be obtained for bistatic scattering, which is needed to compute the emisivity. Mainly there are two different ways to estimate the emissivity of a vegetated soil. The first one is to consider directly the energy fluxes emitted, and subsequently scattered, by the elements which compose the canopy. The second one is based on the energy conservation law. This last method is adopted in the present model. There are two steps: the first one is the computation of the bistatic scattering of the whole upper half-space, as described in the previous section, and the second one is the application of the energy conservation law. Since the emissivity is complementary to the reflectivity, it can be expressed by the integral in equation (3.12)

$$e_q(\theta) = 1 - \frac{1}{4\pi}\int_0^{2\pi}\int_0^{\pi/2}\sum_{p=1}^{2}\frac{\sigma^o_{pq}(\theta,\theta_s,\phi_s)}{\cos\theta}\sin\theta_s d\theta_s d\phi_s \tag{3.12}$$

Since in the model the space is discretized into angular intervals, the integral is transformed into a summation

$$e_{jq} = 1 - \sum_{i=1}^{N\theta} \sum_{p=1}^{2} \frac{\cos\theta_{si} \sin\theta_{si}}{\cos\theta_j \sin\theta_j} S_{ijpq0} \tag{3.13}$$

In the equation (3.13), only the $zero^{th}$ order term of the Fourier series is required, differently from the computation of the backscattering shown in equation (3.11).

3.3 Recent Aspects concerning Litter and Soil

Recently, the problem of litter received attention, and some litter models were developed (Della Vecchia et al, 2007), (Schwank et al, 2008). In this section, I have adopted the model published in Della vecchia et al, (2007), which considers the litter as a dielectric layer over the soil. At first, air-litter and soil-litter interfaces are assumed to be flat. The layer is a mixture of air and dielectric material. The weight of the dielectric material is the basic input, and can be related to the litter-fall by using relationships available in the literature (Cannell 1982). The litter moisture is related to soil moisture, using an empirical relationship based on recent measurements (Grant et al, 2007). The permittivity of the dielectric material is computed as a function of moisture, and the permittivity of the layer mixture is computed by means of the quadratic refractive model for mixtures (Ulaby et al, 1982). The overall reflectivity of this composite medium, made by soil and litter, is computed using a coherent multiple reflection model. In this approach, the litter/soil medium is considered as a two layer medium, and the overall reflectivity is computed taking into account both the magnitude and the phase of the fields reflected and transmitted at each layer boundary, as depicted in Figure 3.4 . Then, an equivalent homogeneous half-space is considered and its permittivity is computed by minimizing a cost function proportional to the rms difference between the set of reflectivity values computed for the composite medium and the one computed for this homogeneous equivalent medium. Finally, the roughness at the interface between air and the previously defined homogeneous half-space is introduced, and described by classical parameters, such as height standard deviation and correlation length. The bistatic scattering coefficient of the ensemble litter/soil is computed, and included in the previously described general model. Details about the procedure are given by Della Vecchia et al, 2007.

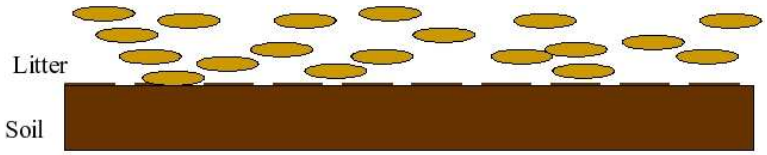

Figure 3.4: Sketch of litter model representation

The dry biomass of the dielectric material DDRY (kg/m^2) may be estimated by using litter-fall data available in Cannell (1982), and assuming two years of fall to be accumulated over the soil. This leads to the following empirical formulas, as given by Della Vecchia et al. (2006a), relating DDRY to the Leaf Dry Biomass LDB (kg/m^2):

$$DDRY = \begin{cases} 1.246.LDB & \text{for Hardwood (Broadleaf) forests.} \\ 0.250.LDB & \text{for Softwood (Coniferous) forests.} \end{cases} \tag{3.14}$$

The gravimetric moisture of dielectric material DMC (kg/kg) is related to volumetric soil moisture SMC (m^3/m^3) by an empirical linear relationship based on recent measurements (Grant et al., 2006a,b). The simple formula is:

$$DMC = \begin{cases} SMC & \text{for } 0 <= SMC < 0.1 \\ 3.0971.SMC - 0.1817 & \text{for } 0.1 <= SMC <= 0.35 \\ 0.85 & \text{for } SMC > 0.35 \end{cases} \tag{3.15}$$

The correlation coefficient for this relashionship is $R^2 = 0.84$. The permittivity of the dielectric material is compuetd as a function of moisture, using the same empirical formula adopted for vegetation (Ulaby and El-Rayes, 1987). The thickness (TL) of the layer, which is a mixture of air and dielectric material, is related to total fresh biomass of the dielectric material DT (kg/m^2) using an empirical linear relationshp derived by fitting the data published in Y. Sato et al.(2004).

$$TL = 0.5.DT \tag{3.16}$$

where TL is in cm.

The corresponding volume fraction values, of dielectric material within the layer, are spread into the interval [0.380.18], for litter moisture val- ues corresponding to a range of volumetric soil moisture values of [0.05 0.30]. At this point the permittivity of the layer mixture is computed by means of the quadratic "refractive model" for mixtures given in

Ulaby et al. (1986, pag. 2044). For soil permittivity, the dielectric model proposed in Hallikainen et al. (1985) is used.

3.4 Forest Structure, Geometrical relationships for Trunk and Crown

In this section, the approach used to give inputs to the discrete model at global scale is introduced. The approach is finalized to predict the signatures of SMOS radiometer, when only general information about ground data is available. The procedure assumes to know, besides soil variables, the following inputs:

- Maximum yearly value of Leaf Area Index contributed by forest leaves $LAI_F max$
- Actual Leaf Area Index LAI_F contributed by forest leaves
- Distribution of trunk diameters at breast height dbh [cm]: $p(dbh)$
- Moisture $[g/g]$ and dry matter density ρ_D [g/cm3] of trunks, branches and leaves.

If these variables are available, the input data set required by the model is obtained according to the procedure indicated below.

First of all, the dry biomass can be converted into woody volume, or viceversa. Since vegetation is composed of water and dry matter, we can establish relations between water content, dry matter and fresh matter for each tree component, i.e.:

$$W_w = VM.WW_D = (1 - VM).WW_w = \frac{VM}{1 - VW} W_D \tag{3.17}$$

VM (Vegetation moisture) is the fraction of water by weight $[g/g]$ (with respect to total fresh matter), W_w is the water weight per unit area $[kg/m^2]$ (i.e. column density), W_D is the dry matter weight per unit area $[kg/m^2]$ and W is the fresh matter weight per unit area $[kg/m^2]$. For each component (trunk, branch, leaf), the volume is given by:

$$V = V_D + V_W = \frac{W_D}{\rho_D} + \frac{W_w}{\rho_w} = \frac{1}{\rho_D} + \frac{1}{\rho_w} \frac{VM}{1 - VM} . W_D = \frac{1 - VM}{\rho_D} + \frac{VM}{\rho_w} . W \tag{3.18}$$

V is the fresh matter volume $[m^3/m^2]$, V_W and ρ_W are the water volume $[m^3/m^2]$ and density $[kg/m^3]$, respectively, V_D and ρ_D are the dry matter volume $[m^3/m^2]$ and density

$[kg/m^3]$, respectively. Equations (3.17) and (3.18) establish a relationship between V and W_D for each forest component. Typical values for dry matter density ρ_D are 0.3 g/cm^3 for leaves and 0.4 g/cm^3 for branches and trunks, whereas the typical values of moisture VM are 0.6 g/g for leaves and 0.5 g/g for woody matter, respectively (saleh et al, 2005), (Droesen et al, 1989).

Let the minimum and maximum values of dbh be defined as dbh_{min} and dbh_{max}, respectively. The $dbh_{max} - dbh_{min}$ range is subdivided into M_T intervals, of width given by:

$$\Delta dbh = \frac{dbh_{max} - dbh_{min}}{M_T} \tag{3.19}$$

For the i^{th} interval, the number N_{Ti} of trees per unit area $[ha^-1]$ with dbh value within the interval is given by:

$$N_{Ti} = N_T \int_{dbh_i}^{dbh_i + \Delta dbh} p(dbh) d(dbh) \tag{3.20}$$

N_T is the tree density $[ha^-1]$, and dbh_i is the value of dbh at the lower limit of the interval. In forest studies (e.g. (Jenkins et al, 2003)) it was found that some tree variables are related to each other by simple laws, where relative increases are proportional to each other. In particular, some pairs of variables (x and y) are related by a law of this kind:

$$\frac{dy}{y} = \frac{dx}{x} \tag{3.21}$$

where k is a coefficient. These kinds of allometric equations can also be useful for providing inputs to electromagnetic models. In particular for a given single tree, the total dry biomass and its subdivision into trunk, branch and leaf fractions, can be related to the diameter at breast height (dbh). For each interval i, the tree dry biomass DB_i (kg) is estimated by means of the allometric equation (Jenkins et al, 2003):

$$DB_i = exp[b_0 + b_1 \ln(dbh_i)] \tag{3.22}$$

b_0 and b_1 are coefficients depending on tree species. For deciduous forests, average coefficients are: $b_0 = -2.48$

$b_1 = 2.4835$

Other allometric equations give the biomass components (kg) contained in trunks (DB_{ti}), leaves (DB_{li}), and branches (DB_{bi}). For trunks:

$$DB_{ti} = DB_i exp(a_{t0} + \frac{a_{t1}}{dbh_i}) \tag{3.23}$$

with: $a_{t0} = -0.30, a_{t1} = -5.42$

For leaves:

$$DB_{li} = DB_i exp(a_{l0} + \frac{a_{l1}}{dbh_i}) \tag{3.24}$$

with: $a_{l0} = -4.08, a_{l1} = 5.88$

For branches:

$$DB_{bi} = DB_i - DB_{ti} - DB_{li} \tag{3.25}$$

The maximum yearly value of leaf dry biomass per unit area DBL (t/ha) can be derived as a function of LAI_{Fmax} by means of empirical formulas. We have adopted the formula given in (Bartelink 1997):

$$DBL = \frac{LAI_{Fmax}}{1.72} \tag{3.26}$$

The tree density N_T can be obtained by using (3.20) and by imposing:

$$DBL = 0.001. \sum_{i=1}^{N} N_{Ti} DB_{li} = 0.001. N_T \sum_{i=1}^{N} DB_{li} \int_{dbh_i}^{dbh_i + \Delta dbh} p(dbh).d(dbh) \tag{3.27}$$

At this point, all required variables for trunks, branches and leaves can be computed, as indicated below.

1) Trunks

Trunks are modelled as equivalent cylinders. For the i^{th} interval of dbh values, the cylinder diameter is assumed to be equal to dbh_i. The dry biomass DB_{ti} (kg) is computed by (3.22) and (3.23), and converted into woody volume WV_{ti} (m^3), according to the procedure described in equation 3.17 and 3.18. The height of the cylinders is given by:

$$DBL = \frac{WV_{ti}}{\pi(0.01.dbh_i/2)^2} \tag{3.28}$$

Since there is a trunk per tree, the number of trees with diameter equal to dbh_i is given by equation (3.22). Trunks are assumed to be vertical.

2) Branches

Branches are subdivided into sections, and sections are modelled as cylinders. For the i^{th} interval of dbh values, the branch dry biomass DB_{bi} can be computed by (3.22)-(3.25) and converted into woody volume WV_{bi}. Branches are subdivided into primary and secondary branches. The latter are assumed to contain 30% of the overall branch volume, according to the estimate given by (Saleh et al, 2005). For primary branches belonging to a tree with dbh equal to dbh_i, the maximum diameter db_{maxi} is assumed to be equal to 0.25 dbh_i. This coefficient, which is slightly higher than values measured in coniferous forests (Saleh et al, 2005), was derived by available photos of some deciduous forests. The branch diameters are assumed to follow a Gaussian pbi distribution, centered at $db_{maxi}/2$. The range between 0 and db_{maxi} is subdivided into M_{bi} intervals of width Δd. For the j^{th} interval, d_j is the central value, and p_{bij} gives the fraction of total branch volume filled by branches with diameter internal to the interval. This assumption is in general agreement with the measured data reported by [Saleh et al, 2005], although they were fitted by different functions. The length of the cylinder is equal to 50 d_j, with an upper limit at 25 cm (Saleh et al, 2005). Also for secondary branches the distribution of filled volumes p_{bsi} is assumed to be Gaussian. The average diameter is equal to 0.6 cm and the length is computed similarly to the case of primary branches. Finally, the total number of cylinders with diameter d_j is given by:

$$N_{bj} = \sum_{i=1}^{M_T} N_{Ti}(p_{bij} + p_{bsij}) \tag{3.29}$$

This distribution is used by the electromagnetic model as input. Both primary and secondary branches are assumed to be randomly oriented.

3) Leaves

Leaves are described as circular disks with a radius of 2 cm and a thickness of 0.02 cm [Ferrazzoli and Guerriero 1996], (Droesen et al, 1989). The number of disks is obtained as the ratio between actual LAI_F and disk area. Also disks are randomly oriented.

3.5 Parametric simulations and simplified model

Application of the SMOS algorithm over forests is accomplished by keeping in mind the considerations indicated below.

- A large fraction of land is covered by forests. All efforts aimed at fully exploiting the potential of SMOS over these areas must be done. Although it is commonly believed

that forest crowns are opaque, some experimental and theoretical studies indicate that the situation is more complex. At higher frequencies (C band and above) there is a strong contribution of leaves to crown attenuation. At L band, leaves are almost transparent, attenuation is mostly due to branches, and soil contribution may be still appreciable, unless the forest is dense.

- A simple empirical approach, based on τ and ω parameters fitted over experimental data is not appropriate to forests, due to two main reasons.
  - Only a limited amount of experimental brightness data is presently available at L band. Therefore, a statistically reliable fitting is not feasible. Several radar signatures would be available, but a direct reuse of these signatures to derive emission parameters is not reliable, due to some basic differences between emission and backscattering processes.
  - In forests, emission/scattering processes are complex, since trunks and branches are not small vs. λ. Therefore, multiple scattering effects are appreciable and a simple first-order approach is not reliable.
- Anyhow, the methodology to be adopted for forests must be harmonized with the general SMOS retrieval algorithm, and the complexity of the operational procedure must be kept limited.

By keeping in mind these considerations, the adopted approach is considered as follow:

The dbh distribution is assumed to be Gaussian, with an average value $< dbh >$ of 20 cm and a standard deviation of 5 cm. For the range of dbh values, I established a lower limit $dbh_m in$ equal the average $< dbh >$ minus three times the standard deviation, and an upper limit dbh_{max} equal to $< dbh >$ plus three times the standard deviation. The actual Leaf Area Index LAI_F and the maximum yearly value of Leaf Area Index LAI_{Fmax}, contributed by forest leaves, are derived by ECOCLIMAP.

The theoretical model was used to predict the trends of emissivity (in full leaf development) for the case of Decidous forests, as a function of maximum yearly value of LAI_{Fmax}. Examples of trends are given in Figure 3.5. Also the case of absence of litter was considered. As expected, the dynamic range is reduced by increasing LAI_{Fmax}, while it is still significant for $LAI_{Fmax} < 3$. The effects of litter are low for dry soils, but become important for moist soils. The simulation outputs were used to fit the equivalent parameters (τ_F and ω_F) of the

simple RT model of the SMOS Algorithm Theoretical Based Document (ATBD). The fitting procedure was subdivided into several steps. First of all, a height standard deviation of soil roughness equal to 1.5 cm was selected. The roughness factor h of the ATBD model was set by imposing the surface emissivity of the ATBD model to be equal to the surface emissivity of the physical model. The physical model was run at both polarizations, an angular range 5°-55° and a SMC range 5%-30%. Then, the ATBD model was run for the same conditions, and ω_F and τ_F were selected in order to have the minimum rms difference between outputs of the two models.

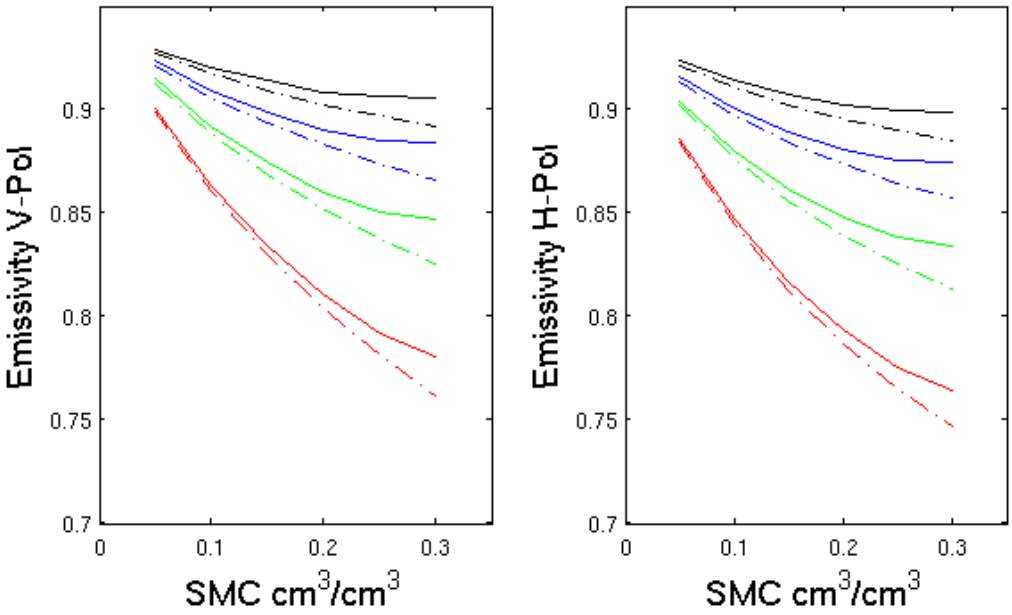

Figure 3.5: Simulated trends of emissivity vs. soil moisture for deciduous forests. Polarization: vertical (left), and horizontal (right).Maximum yearly value of forest LAI from 1 (lower curves) to 4 (upper curves). Continuous lines: with litter. Dashed lines: without litter. -

I have verified that the obtained results are scarcely affected by the initial choice about roughness, provided the same roughness is selected for the two models.

A general scheme of the procedure adopted to generate the input data set is given in Figure 3.6

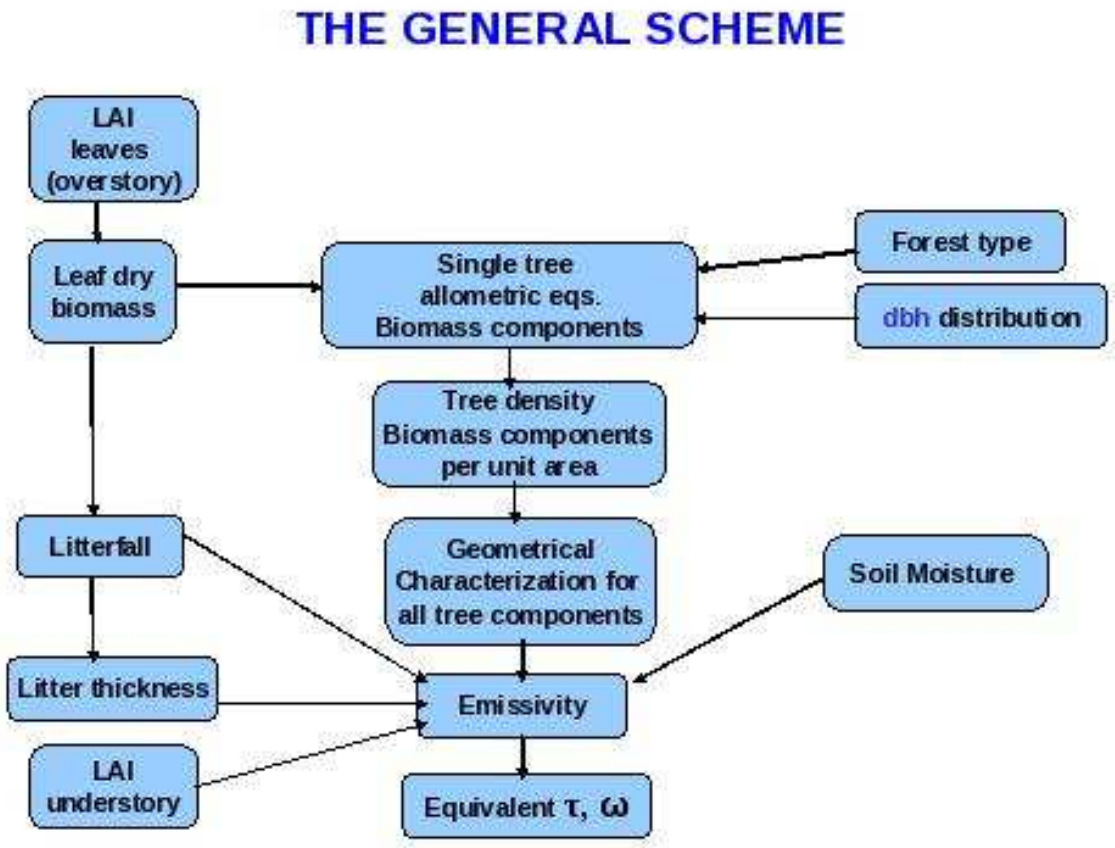

Figure 3.6: General scheme of the procedure. -

The trends of τ_F and ω_F as a function of LAI_{Fmax} are shown in Figure 3.7. Values of τ_F lower than about 0.6 are achieved for sparse forests with $LAI_{Fmax} < 2$. The albedo ω_F shows a decreasing trend vs. LAI_{Fmax} .

A further best fit procedure was applied, in order to obtain the coefficients of a linear relationship between optical depth and LAI_{Fmax}, such as:

$$\tau_F = b_F LAI_{Fmax} - s_F[\frac{(LAI_{Fmax} - LAI_F)}{LAI_{Fmax}}] \tag{3.30}$$

The first term gives the optical depth in full leaf development, while the second term gives the seasonal reduction due to the fall.

The fitting gives:

$b_F = 0.23$ in absence of litter;

$b_F = 0.29$ in presence of litter.

$s_F = 0.03$

The total optical depth, including contributions of both forest leaves and herbaceous vegetation is given by:

$$\tau = \tau_F + b_v LAI_v \tag{3.31}$$

In the SMOS Algorithm Theoretical Based Document (ATBD), and for low vegetation, the b_V value are set to 0.06, and LAI_V is available by ECOCLIMAP.

The average value of the albedo is:

$\tau_F = 0.106$ (but lower values fit better for dense forests)

3.6 Tests

This section shows model simulations of forest emissivity using the electromagnetic model described in section 3.2. The model has been combined with information available from forest literature. Using allometric equations and auxiliary information, the geometric and dielectric inputs required by the model have been related to global variables available at large scale, such as Leaf Area Index and forests biomass. Parametric simulations, as well as comparisons with radiometric signatures collected in various forest sites as indicated below:

- Airborne measurements were collected in summer 2000 and winter 2002 in Tuscany (Italy) over various broadleaf forests, spanning a wide range of biomass (Macelloni et

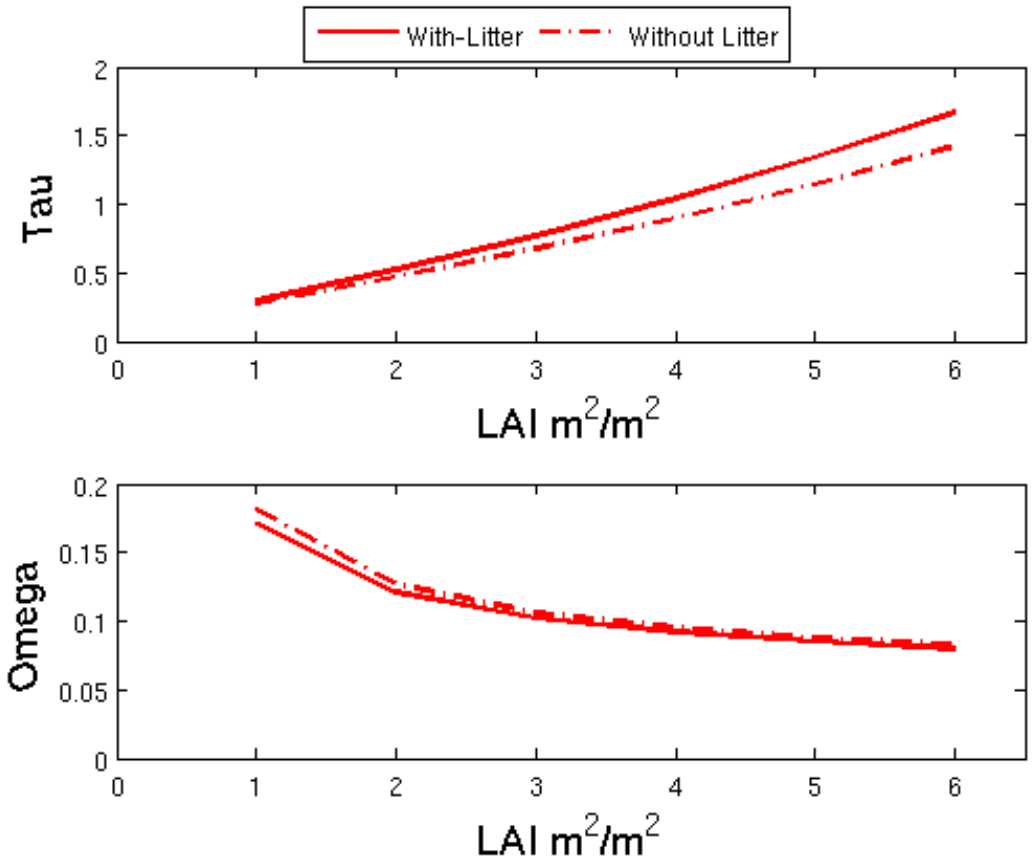

Figure 3.7: Trends of fitted RT parameters as a function of maximum yearly value of forest LAI, for deciduous forests. -

al, 2001). The radiometer operated at 30 ° incidence angle and Vertical polarization and at L, C and X bands. Ground truth covered some main forest variables, such as biomass, height, dbh distribution, and LAI.

- L-band measurements were made by the AMIRAS demonstrator in June 2006 over dense forests in Finland. In this case, inputs to the model were given on the basis of ECOCLIMAP.

- Multitemporal airborne measurements were collected in the Eucalyptus forest of Roscommon, in Australia, in November 2005, in the framework of the NAFE05 campaign (Panciera et al, 2009), (Grant et al, 2010). Ground measurements covered the soil moisture, the litter thickness, and the LAI. The forest was moderately dense, with a LAI of 2.5.

3.6.1 Multifrequency Emission of broadleaf forests in Toscany

3.6.1.1 The Experimental data set

Five broadleaved forests located in Tuscany (Italy) were observed on 29-30 June 1999 and on 7-10 January 2002 by a set of airborne microwave radiometers working at 1.4, 6.8, 10.0, 19.0, and 37.0 GHz and at 30° incidence angle (Macelloni et al, 2001), (Macelloni et al, 2003). L band measurements were carried out at vertical (V) polarization only, whereas both vertical and horizontal (H) data were available at the higher frequencies (Table 3.1). The thermal infrared brightness temperature was measured by using an infrared sensor in the 8-14 m band. A TV camera was also used as a reference. The radiometric accuracy was better than ± 1 K and The antenna footprint was of the order of 100 m, at all frequencies. The brightness temperatures were computed by averaging among the samples of each forest site. Considering that the integration time of radiometric acquisitions was 100 ms, and that the duration of flights over the forest sites was 240-300 s, the averaging was performed over a total number of samples in the order of 3000. For all sites radiometric signatures were collected in a central area of about 25 hectares.

Important forest variables were measured during the ground surveys (Cozzi et al, 1996), (Bartolozzi et al, 2002). These include: forest species, tree density, average dbh, forest height and leaf area index (LAI). Two forests (Teso, Vallombrosa) were dominated by

X	Ulignano	Colognole	Cala Violina	Teso	Vallombrosa
Tree density (ha^-1)	1424	1547	2052	348	396
Total woody volume (m^3/ha)	214	348	402	712	1433
Leaf Area Index (summer)	2.2	5.1	4.2	3.6	4.3
Average dbh (cm)	12.5	15.7	13.4	36	40.5
St.dev.dbh (cm)	6.25	7.85	6.7	9	10.125
Vol.soil.mois.in summer (m^3m^-3)	0.16	0.18	0.16	0.16	0.16
Vol.soil.mois.in winter (m^3m^-3)	0.25	0.18	0.18	0.25	0.25
Understory optical depth (summer)	0.2	0.2	0.1	0	0

Table 3.1: BASIC INPUT VARIABLES

beech, showed values of woody volume higher than 700 m^3/ha and an average dbh higher than 35 cm. Two forests (Cala Violina, Colognole) were mainly populated by Holm oak, but with an appreciable presence of other species. For these forests, the woody volume was in the range 300-400 m^3/ha, and the average dbh was lower than 15 cm. Finally, one forest (Ulignano) was dominated by Turkey oak. The woody volume (about 200 m^3/ha) was lower than the other ones, and the average dbh was lower than 15 cm. Details about ground measurements are available in (Macelloni et al, 2001), (Cozzi et al, 1996), and (Bartolozzi et al, 2002).

3.6.1.2 Model inputs

The model was run using forest parameters as input, and the corresponding outputs were compared with measured emissivities. The measured values of tree density and forest height were directly used as model inputs. For dbh, the average value $< dbh >$ was taken from the ground measurements (Bartolozzi et al, 2002). For each forest, the dbh distribution was assumed to be Gaussian. On the basis of data available in (Bartolozzi et al, 2002), the associated standard deviation was assumed to be equal to 0.25 times the average for the homogeneous beech forests, 0.5 times the average for the mixed sites of Ulignano, Colognole and Cala Violina. The values are given in Table 3.1.

Direct measurements of soil moisture were not available. In order to estimate this variable we computed, for each site, the Antecedent Precipitation Index (API) (Teng et al, 1995), using rainfall data of the closest meteorological stations, which are available in the meteorological website www.ilmeteo.it. For Ulignano, Teso and Vallombrosa the closest station was Florence, whose distance ranged from 25 km (for Vallombrosa) to 40 km (for Ulignano and Teso). In this station, the API was equal to 15.4 mm, for the flight of June 1999, and was equal to 36.5 mm, for the flight of January 2002. For Colognole the closest station was Pisa, at a distance of 20 km., In this station, the API values were 19.6 mm (flight of June 1999) and 21.0 mm (flight of January 2002). For Cala Violina the closest station was Grosseto, at a distance of 25 km. In this station, the API values were 15.2 mm (flight of June 1999) and 19.0 mm (flight of January 2002). Previous studies (e.g. Teng et al, (1995)) indicated API to be correlated with variations of soil moisture in single sites. The coefficients of the regression depend on the site and climatic conditions. In order to calibrate these coefficients, we used the

multitemporal SMC measurements carried out in another forest of the same Tuscany region, during the experiment described by Santi et al, (2007). Using a classical best-fit technique, we found a determination coefficient (R2) higher than 0.9, and the following relationship:

$$SMC = 10 + 0.43.API \tag{3.32}$$

By applying eq. 3.32 to the API values given above for the forest sites of this work, we found the values of SMC shown in Table 3.1. Ground surveys (Chiarucci et al, 1996) indicated the presence of a dense understory, in summer, in the sites of Ulignano and Colognole, and, to a lesser extent, in Cala Violina. The understory cover was 60%-70% in Ulignano and Colognole, while it was about 15% in Cala Violina. The understory was a mixture of grass and shrubs. In absence of more detailed information, we represented it as a thin absorbing layer over the soil, with values of optical depth indicated in Table 3.1. Using the simple formulas published in (Jackson et al, 1991) and the coefficients of grass at L band, the ratio between optical depth and plant water content is about 0.3 m^2/kg (Jackson et al, 1991). Under these approximations, the values of Table 2.1 correspond to about 0.7 kg/m^2 for Ulignano and Colognole, and 0.35 kg/m^2 for Cala Violina.

In summary, tree density, woody volume, $< dbh >$ and LAI have been directly taken by measurements (Macelloni et al ,2001), (Cozzi et al, 1996). I have been forced to adopt indirect estimates and assumptions for the standard deviation of dbh, the soil moisture and the understory. The ratio between dbh and the maximum branch diameter was fixed to 4, on the basis of available photos. The discrepancies in the comparisons with experimental data, which will be discussed in the next subsections, can be attributed to some approximations of the input data, besides the inaccuracies of the electromagnetic model itself. Starting from the data of Table 3.1, all the other inputs were computed using the procedure indicated in section 3.4. For the range of dbh values, we established a lower limit dbh_{min} equal the average $< dbh >$ minus three times the standard deviation, and an upper limit dbh_{max} equal to $< dbh >$ plus three times the standard deviation. Within this range, the operations indicated in formulas (3.19) and (3.20) were applied. The final computation of the emissivity was done by performing a weighted average over all dbh values, using the numbers computed by eq. (3.20) as weights.

The subdivision into trunk and branch volumes was made for each value of dbh using equations (3.22), (3.23). The condition that the overall forest volume was equal to the measured one was imposed by multiplying their estimated values by a normalization factor. Measured values of leaf area index in June were used to estimate leaf contribution and litter-fall. Table 3.2 shows a list of input variables computed using the procedure of Section 2.4, as well as the adopted methods and the relevant references.

X	Value or range	Method of estimate	References
Litter dry biomass (kg/m^2)	0.185-0.43	Related to LAI and litterfall by eq.	2052
Total woody volume (m^3/ha)	214	348	402
Leaf Area Index (summer)	2.2	5.1	4.2
Average dbh (cm)	12.5	15.7	13.4
St.dev.dbh (cm)	6.25	7.85	6.7
Vol.soil.mois.in summer (m^3m^-3)	0.16	0.18	0.16
Vol.soil.mois.in winter (m^3m^-3)	0.25	0.18	0.18
Understory optical depth (summer)	0.2	0.2	0.1
St.dev.dbh (cm)	6.25	7.85	6.7
Vol.soil.mois.in summer (m^3m^-3)	0.16	0.18	0.16
Vol.soil.mois.in winter (m^3m^-3)	0.25	0.18	0.18
Understory optical depth (summer)	0.2	0.2	0.1

Table 3.2: Basic input variables

3.6.1.3 Comparisons between simulated and measured data

Comparisons between simulated and measured values of emissivity at L band are shown in Table 3.3.

Site	Measured Emissivity V-Pol	Simulated Emissivity V-Pol
Ulignano (summer)	0.911	0.900
Colognole (summer)	0.914	0.914
Cala Violina (summer)	0.931	0.918
Teso (summer)	0.931	0.929
Vallombrosa (summer)	0.938	0.941
Ulignano (winter)	0.867	0.873
Teso (winter)	0.928	0.917

Table 3.3: Comparison between measured and simulated values of emissivity at L band. RMS error computed over all samples: 0.0076 emissivity units.

For summer measurements, the model reproduces the measurements for beech (Teso and Vallombrosa) with an error lower than 0.003 emissivity units. Some underestimations are observed for the sites of Ulignano and Cala Violina (0.011 and 0.013 emissivity units, respectively). This could be due to inaccuracies of the electromagnetic model, insufficient statistical characterization of the variability of forest properties, inaccuracy of soil moisture value, or underestimation of the understory effect. The rms error computed over all L band samples is equal to 0.0076 emissivity units (corresponding to about 2.0 K).

Comparisons at C band are shown in Table 3.4. The agreement between measured and simulated values is generally good. A comparison with L band values indicates that the model reproduces the increase of emissivity with frequency. Seasonal effects are low in both experimental and simulated data. Also polarization effects are low.

Comparisons at X band are shown in Table 3.5. The agreement is generally good for the summer samples. For winter samples, the emissivity is close to the unity, since leaves are absent and branches produce low scattering in the upper hemisphere, at the higher frequencies. The reasons for this are illustrated in (Ferrazzoli et al, 1995) and will be further discussed later. The rms errors, in emissivity units, are equal to 0.0074 over C band samples and 0.011 over X band samples (corresponding to about 2.0 K and 3.0 K, respectively). The discrepancies are mostly related to underestimations of emissivity of Holm oak forests, possibly due to incomplete representation of their leaf scattering.

Site	Measured Emissivity V-Pol	Simulated Emissivity V-Pol	Measured Emissivity H-Pol	Simulated Emissivity H-Pol
Ulignano (summer)	0.964	0.959	0.955	0.956
Colognole (summer)	0.972	0.956	0.962	0.953
Cala Violina (summer)	0.969	0.956	0.960	0.953
Teso (summer)	0.954	0.951	0.944	0.948
Vallombrosa (summer)	0.956	0.950	0.947	0.947
Ulignano (winter)	0.934	0.921	—	—
Cala Violina (winter)	0.959	0.955	—	—
Teso (winter)	0.948	0.943	—	—

Table 3.4: Comparison between measured and simulated values of emissivity at C band. RMS error computed over all samples: 0.0074 Emissivity Units.

Site	Measured Emissivity V-Pol	Simulated Emissivity V-Pol	Measured Emissivity H-Pol	Simulated Emissivity H-Pol
Ulignano (summer)	0.979	0.977	0.978	0.973
Colognole (summer)	0.984	0.967	0.983	0.962
Cala Violina (summer)	0.990	0.974	0.989	0.969
Teso (summer)	0.973	0.976	0.972	0.972
Vallombrosa (summer)	0.979	0.981	0.978	0.978
Ulignano (winter)	0.955	0.968	—	—
Cala Violina (winter)	0.971	0.979	—	—
Teso (winter)	0.970	0.987	—	—

Table 3.5: Comparison between measured and simulated values of emissivity at X band. RMS error computed over all samples: 0.011 Emissivity Units.

As illustrated above, some input variables, such as the ones indicated in the first four lines of Table 3.1, were given on the basis of direct measurements, and other variables were computed using formulas available by literature (see Table 3.2). For other variables, such as soil moisture, understory optical depth, and the ratio between dbh and the maximum branch diameter, some approximations were necessarily applied. In order to evaluate the influence of these variables, which are affected by some uncertainty, a sensitivity analysis was carried out. We assumed to have the following variations with respect to values of Tables 3.1 and 3.2: $\pm$ 0.05 m3/m3 for soil moisture, $\pm$ 0.05 for understory optical depth, $\pm$ 0.5 for the ratio between dbh and the maximum branch diameter. In Figure 3.8, the measured and simulated values of emissivity are plotted as a function of frequency for the five sites. The error bars in the simulated values are associated to the results of the sensitivity analysis. The lower end gives an emissivity obtained by assuming to have the highest value of SMC, the lowest value of understory optical depth and the highest value of the ratio between the dbh and the maximum branch diameter. The upper end gives an emissivity computed by using the opposite assumptions. For the sake of simplicity, only data at vertical polarization, which are available at all frequencies, are represented. The site of Ulignano, for which both summer and winter measurements are available, is characterized by the lowest biomass (see Table 3.1). In this site, seasonal effects are appreciable, and are attributed by the model to variations of soil moisture and understory, besides the fall of deciduous leaves. In this site, also a strong increase of emissivity with frequency is observed, in both seasons. For forests with higher values of biomass, the trend of emissivity versus frequency tends to become flat. In fact, emissivity at L band is larger than the one of Ulignano, while variations at higher frequencies are limited. The dense beech forest of Teso shows small seasonal effects. In this forest, the understory was sparse also in summer, and the variations of soil moisture are masked by the higher crown attenuation. The range limited by error bars is very low at C and X band. At L band the range is variable, depending on the forest properties and the season. The maximum uncertainty is observed in summer at Ulignano, Cala Violina and Colognole. In spite of some discrepancies, the model represents the main properties of experimental data. The influences on emissivity of forest biomass, seasonal properties and frequency are generally captured by the model. These physical effects are higher than the model errors, also considering the effects of some uncertainties about input variables, represented by the error bars in Figure 3.8.

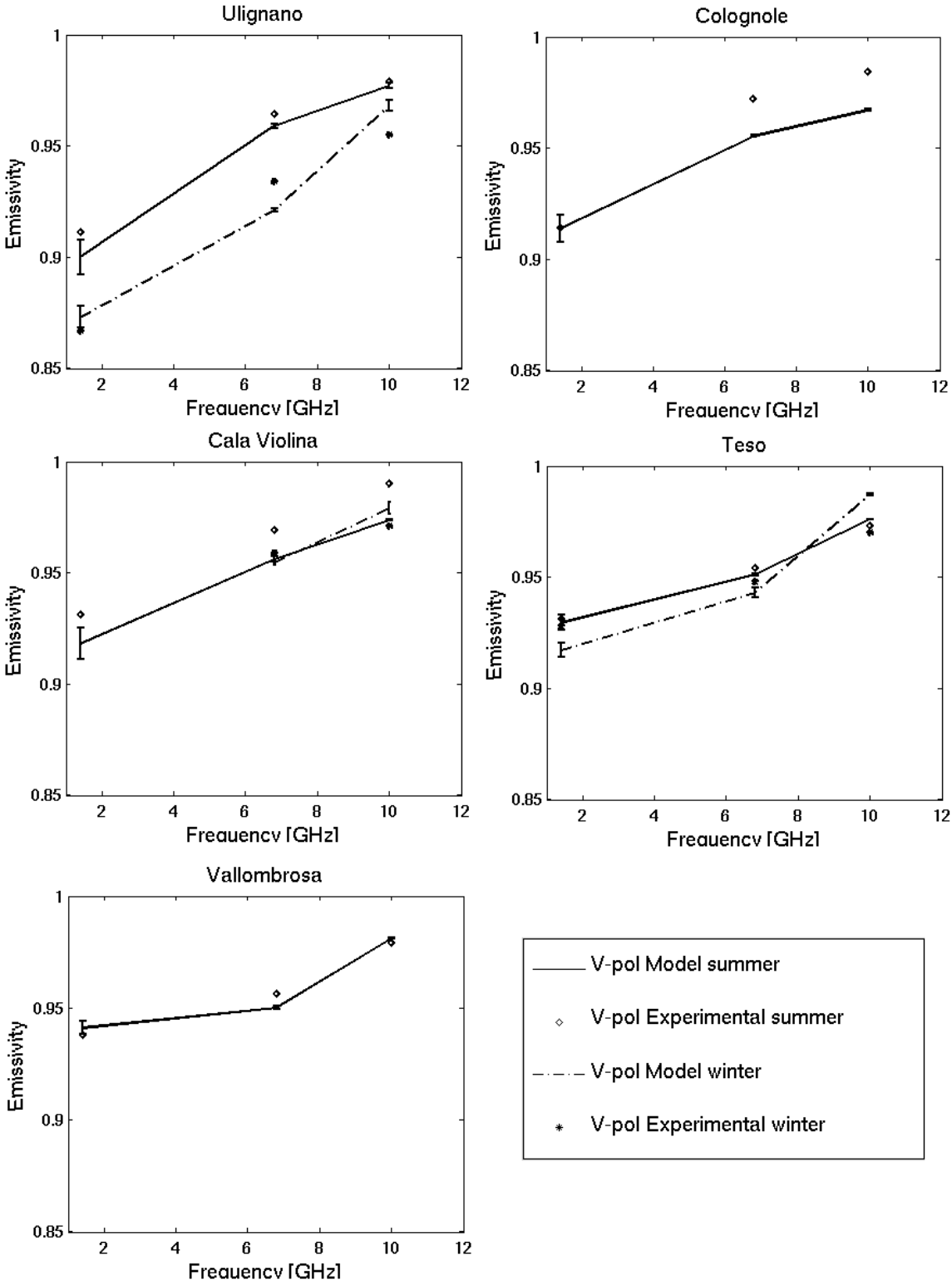

Figure 3.8: Measured and simulated trends of emissivity as a function of frequency for the five forests. 30° observation angle, vertical polarization. Error bars in simulated values indicate the effects of variations of input variables: $\pm 0.05 m^3/m^3$ for soil moisture ± 0.05 for understory optical depth, ± 0.5 for the ratio between dbh and the maximum branch diameter. -

3.6.1.4 Single components

In order to get an insight into the emission properties and their dependence on frequency, the contributions due to single forest components have been analyzed. The simulated trends as a function of the frequency of the overall emissivity at vertical polarization, and the single contributions due to crown and soil, are shown in Figure 3.9. Both summer and winter cases are considered. The soil contribution includes the effects of litter and, for summer samples, understory. The upper plot is for the Teso beech forest, characterized by a high woody volume. For this forest, the emissivity of crown dominates at all frequencies, although it is appreciably lower than the overall emissivity, especially at L band. Seasonal effects on crown emission, which are due to leaves, are very low at L band and clearly increase with frequency. All these results are in agreement with experimental data collected over a dense deciduous forest by both upward looking and downward looking radiometers (Guglielmetti et al, 2007, 2008), at L and X band.

The lower plot is for Ulignano forest, which is characterized by a lower woody volume. Here the difference between crown contribution and soil contribution is lower, at L band. The increase of crown contribution with frequency (from L to C band) is well evident in summer, due to the effect of leaves, but is less evident in winter. As expected, the trend of soil contribution is opposite with respect to the one of crown contribution. By removing litter and understory, the soil contribution is reduced by a factor of about 0.7 (in summer). At C and X band, this reduction has a limited impact on the overall emissivity, due to the high crown attenuation. At L band, the effects on the overall emissivity are appreciable, and will be investigated in the next Section.

3.6.1.5 Parametric analysis about soil moisture effects

We have simulated the effects of soil moisture variations under forests with the same properties of Ulignano and Teso sites, in both seasons. Results are shown in Figure 3.10. Under the dense beech forest of Teso, the dynamic range is low in both seasons, due to the high crown attenuation. However, the sensitivity to soil moisture variations is moderate also for the forest of Ulignano, which is characterized by a woody volume slightly higher than 200 m^3/ha. In winter, the emissivity decreases from about 0.89

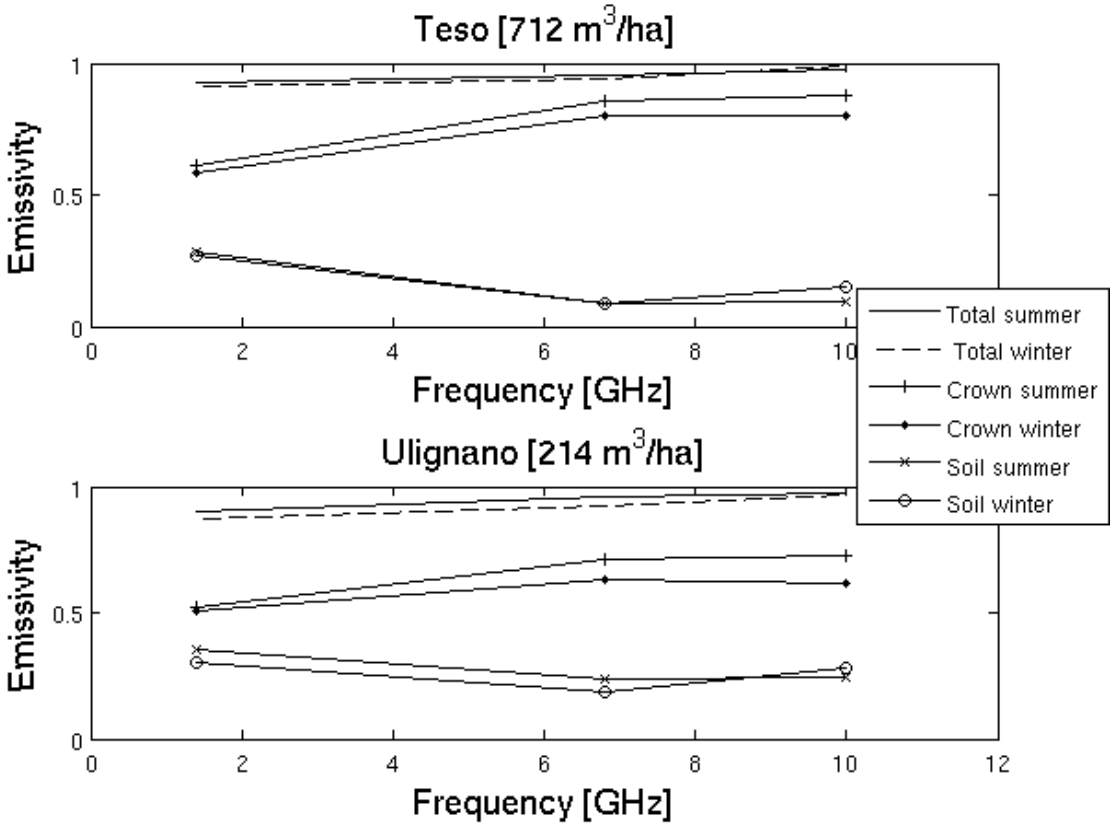

Figure 3.9: Simulated trends of overall emissivity and single components, as a function of the frequency. The soil component includes litter and understory contributions. Top: Teso beech forest. Bottom: Ulignano Turkey oak forest. 30°, vertical polarization -

to about 0.88 for an increase of SMC from 0.1 to 0.3 This result is related to the low value of the average $< dbh >$ measured in this forest (12.5 cm). In fact, according to the relations described in Section 3.4, a low dbh is associated to several small branches, which produce a higher attenuation with respect to few large branches, for a given overall woody volume. We have verified that, for the same woody volume of 200 m^3/ha, we obtain a better sensitivity to soil moisture variations for higher values of $< dbh >$. E.g., for a $< dbh >$ of 20 cm, the emissivity decreases by about 0.03 units, for an increase of SMC from 0.1 to 0.3. We repeated the simulations assuming absence of litter. Results are shown in the right side of Figure 3.10. As expected, the slope of the emissivity vs. SMC trend is increased in all cases, particularly for the highest values of SMC. For Ulignano site the dynamic range is lower in summer, due to understory attenuation. This is more evident in the right figure (absence of litter) since, in presence of litter, the dynamic range was already low by itself, also in winter.

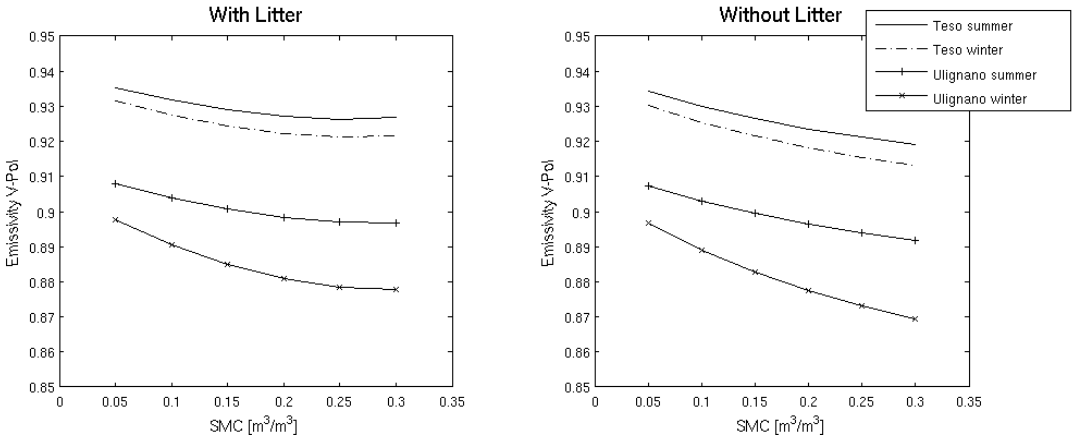

Figure 3.10: Model simulation of emissivity as a function of soil moisture for forests with the same properties of Teso (upper diagrams) and Ulignano (lower diagrams). L band, 30°, vertical polarization. Left: with litter. Right: without litter. -

3.6.1.6 Parametric analysis about woody volume and dbh

The data reported in Table 3.3 indicate that, on average, the emissivity tends to increase as a function of woody volume, at L band. This property is basically reproduced by

the model, although with some discrepancies. Ground measurements indicated that the highest values of woody volume (per hectare) were observed in beech forests, which were also characterized by high values of the average dbh. On the other hand, at Ulignano site both the woody volume (per hectare) and the average dbh were appreciably lower. The procedure described in Section 3.4 indicates that the dbh parameter is important, in that controls important geometrical properties, such as the maximum branch diameter and the ratio between the volume of branches and the overall volume.

In order to single out the effects of the overall volume and the dbh (which, in turn, controls important branch variables), we have considered the theoretical case of forests with equal trees and we have simulated the trend of emissivity vs. volume by assuming the increase of volume to be obtained by a simple increase in the number of trees. The simulations have been carried out at L band, 30 and vertical polarization, and have been repeated for four values of dbh, i.e. 10 cm, 20 cm, 30 cm and 40 cm. All tree variables have been related to dbh according to the procedure described in Section 3.4. The objective of this simulation is to get an insight into the relative importance of overall volume and dbh. This is important as a scientific investigation, but can be useful also for applications. In fact, allometric equations are valid only at single tree level. The number of trees per hectare is generally decreasing with biomass (while the average dbh is increasing) but there is a wide variability of cases, depending on environmental conditions. Therefore, the woody volume (per unit area) and the average dbh should be considered, in principle, as independent variables.

The results of this parametric simulation are shown in Figure 3.11. For values of woody volume lower than about 100 m^3/ha, the emissivity increases with the volume, and the effects of dbh (which controls tree geometry) are moderate. However, for dense forests, the influence of dbh becomes dominant. For the case of Tuscany forests considered in this paper, the dynamic range of emissivity values measured at L band is mostly related to a synergistic effect of variations of both woody volume and dbh. Both effects contribute to make the emissivity of beech forests higher than the other ones.

The results of Figure 3.11 indicate that the highest emissivity values are obtained in presence of trees with large values of dbh. On the other hand, the maximum branch diameter has been assumed to be proportional to the dbh itself, and at L band the emissivity is mostly contributed by branches (Ferrazzoli and Guerriero 1996). Therefore

the result of Figure 3.11, as well as the increasing trend of emissivity vs. frequency, can be associated to the branch dimensions. In order to investigate this effect, we have plotted the average bistatic scattering patterns of randomly oriented cylinders, having the same permittivity of branches, at L, C and X band. The plots have been done for the case of small diameters (0.6 cm, corresponding typically to secondary branches) and for the case of large diameters (2 cm). The plots are reported in Figure 3.12. The upper left plot indicates that, at L band and for a wave incoming from the upper half space over small cylinders, the scattering is mainly forward, but there is an appreciable fraction of scattering in the upper half-space. As discussed in (Ferrazzoli and Guerriero 1996), due to the energy conservation law, this produces a lowering of the emissivity. The upper right plot indicates that, at L band but for larger cylinders, the scattering is mostly directed downward. Therefore, the incoming power is either absorbed or scattered towards lower branches and soil, which will produce further absorption. The overall consequence is an increase of the emissivity. This is even more evident at the higher frequencies (central and lower plots). Here the upward scattering is very low, and the medium tends to behave as a black body.

These theoretical scattering patterns allow us to simply interpret the emissivity behavior with respect to both geometrical forest parameters and frequency. Furthermore, they highlight that forest emissivity is related to an important electromagnetic parameter, i.e. the ratio between the average branch diameter and the wavelength $\frac{d}{\lambda}$.

3.6.1.7 Further Applications

The results described in the previous sections have some implications with respect to microwave radiometry of land. In particular, two important topics can be considered: 1) the sensitivity to soil-moisture variations under forests and 2) the influence of forest biomass and geometrical factors on microwave emissivity. Results shown in Fig. 3.10 confirm that, at L-band, the sensitivity of forest emissivity to soil moisture is low, when compared with the case of crops or grass (see, e.g., Jackson et al (1991)). Crown attenuation, understory, and litter contribute to this effect in different ways. For Ulignano, the forest biomass is relatively low. However, since the average dbh is small (12.5 cm), there are several small branches, which produce high attenuation.

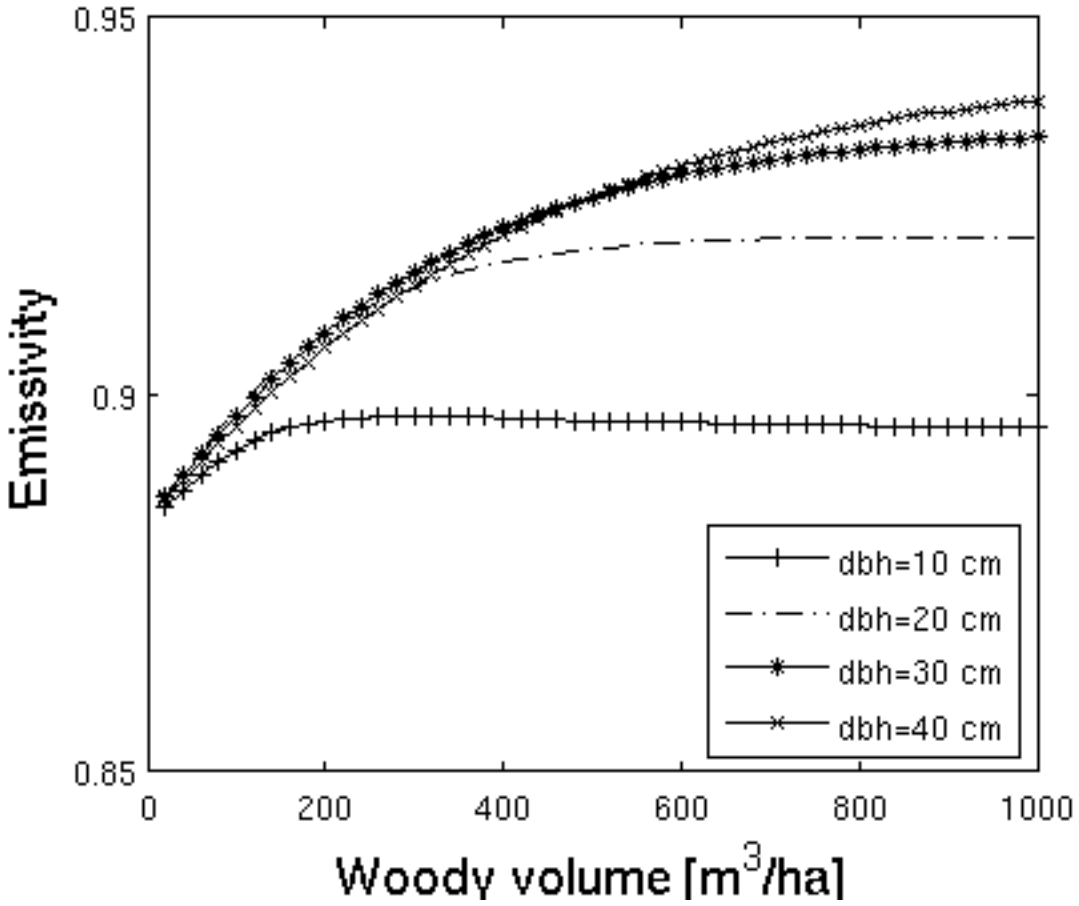

Figure 3.11: Emissivity as a function of woody volume (m^3/ha) for equal trees in four different cases of dbh (in cm). L band, 30°, vertical polarization. -

In summer, the effect is increased by the presence of the understory. For Teso, the attenuation of soil emission is related to the high biomass.

Results shown in Fig. 3.11 indicate that the average dbh, due to its indirect influence on branch properties, plays an important influence on the emissivity of developed forests. The old beech forest of Teso contains trees with higher dbh values and, hence, with larger branches, producing higher values of emissivity. This result can have various consequences for applications. The adoption of a simple model, considering the albedo as a unique constant, is not completely correct. In reality, the value of the albedo is dependent on the average dbh, which is normally related to the age of the forest. On the other hand, this result shows that L-band signatures have the potential to identify forests in which larger and older trees dominate. These properties can be smoothed at the scale of a spaceborne pixel.

3.6.2 AMIRAS SMOS Demostrator

3.6.2.1 Description

The small Airborne MIRAS (AMIRAS) is a reduced version of the MIRAS (Microwave Imaging Radiometer with Aperture Synthesis) instrument on board of SMOS satellite. It was developed in the framework of an ESA contract under the MIRAS Demonstrator Pilot Project 3 (MDPP-3) in 2005. The instrument is a Y-shaped two-dimensional interferometric aperture synthesis radiometer of 4 elements per arm with unit spacing 0.875 and a noise-injection radiometer in the center. Figure 3.13 shows the AMIRAS overall receiver layout. At the center of the array, there is a NIR of the Dicke type, which measures accurately the total power of the scene. Unlike the SMOS LICEF-2 receivers which measure the two polarizations sequentially, NIR has two parallel channels to measure both at the same time.

Two flights took place.

The Flight-1 was conducted on June 20^{th} 2006 in Finland from 20:00 to 21:39 UTC time. The route followed by the aircraft during the Flight-1 was Fagero Kalbadagrund Light House Sea Area East and West of Helsinki (along border zone) Lake Lohja. Figure 3.14 shows the area overflown by AMIRAS instrument.

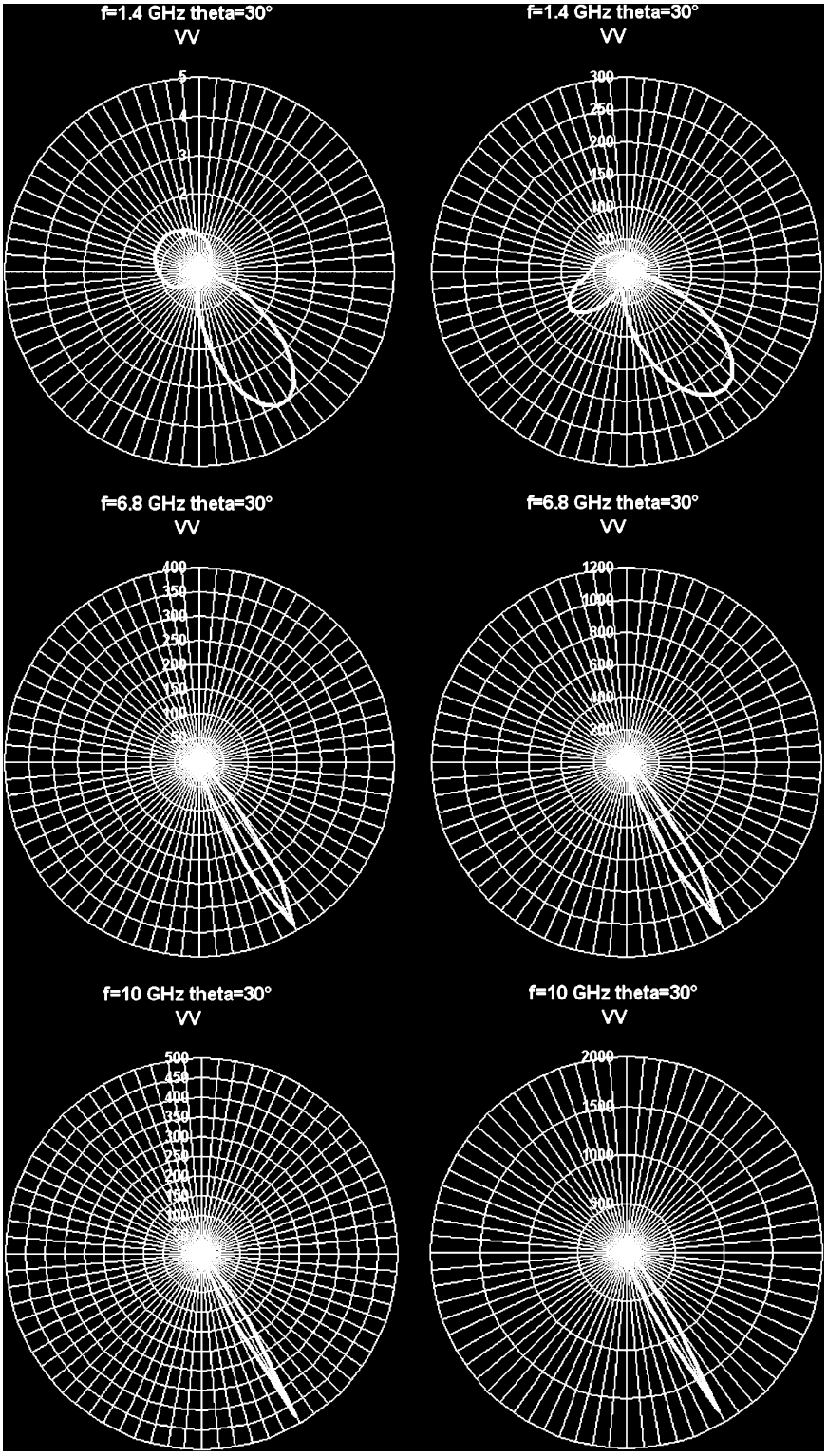

Figure 3.12: Averaged bistatic-scattering patterns of ensemble of cylinders for a wave incident at 30°, V polarization. Cylinder length: 25cm, Cylinder diameter: (left) 0.6cm, (right) 2cm. Upper patterns: L-band. central patterns:C-band. Lower patterns: X-band

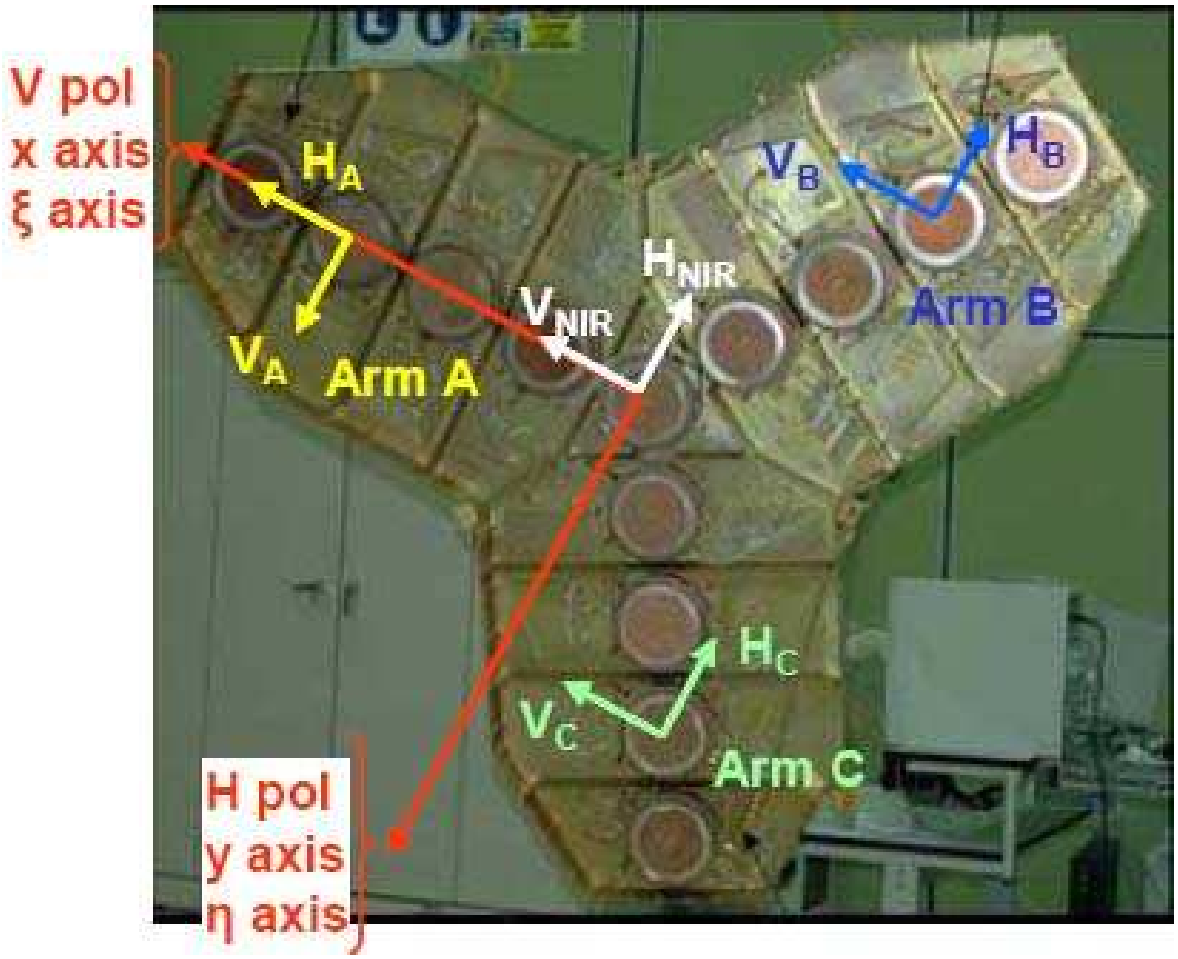

Figure 3.13: AMIRAS overall receiver layout. -

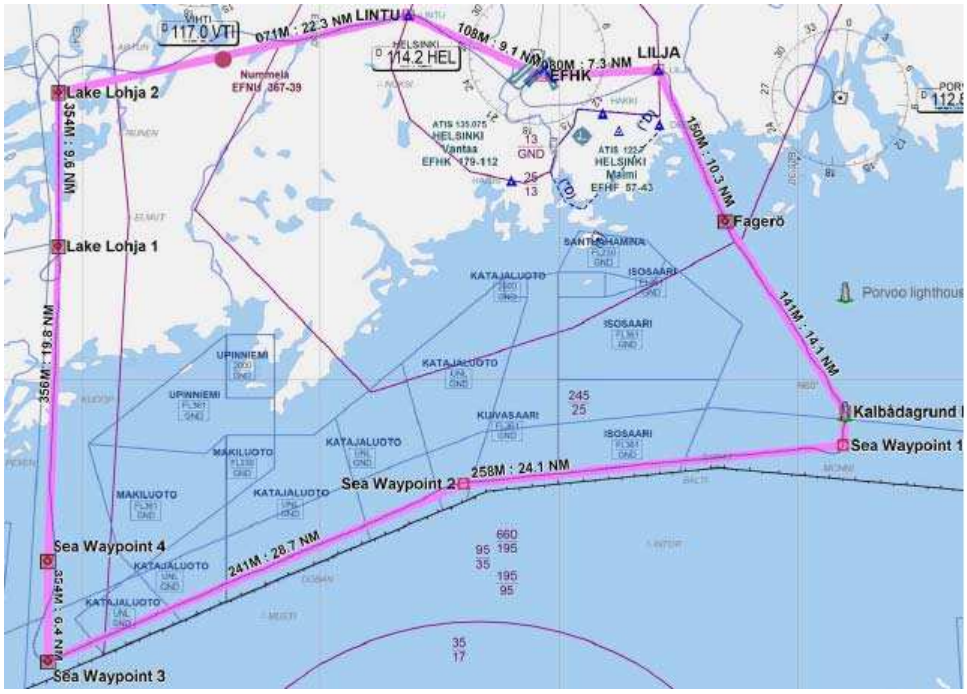

Figure 3.14: Surface overflown by AMIRAS

The flight profile consisted on point-to-point straight flight legs. While over land, the altitude was maintained at 300 m, over open water the altitude was raised to 600 m. The leg over Lake Lohja was repeated 3 times. During the 3rd overflight, the speed of the aircraft was increased and the aircraft flaps were lowered (18°) for a lower pitch and larger angle of incidence for the instrument. The measurements gathered during the Flight-1 are in dual polarization mode. The measured targets were:

- Bare soil.
- Vegetated soil
- Lake water
- Sea water

Flight altitudes ranging from 300 m to 600 m were selected using minimum applicable altitude to obtain measurements with finer ground resolution.

3.6.2.2 Product description

The instrument output, named L1C product is a compilation of the time-tagged measurements of brightness temperature located in a fixed grid with respect to the Earth surface, together with the information describing the geometry between the target and the sensor. The L1C product is split into three products according to the measured target: land, sea and coast. Each product is mapped on a specific grid which is computed according to the instrument resolution and the altitude of the aircraft. The area covered by each product is:

Product	Interval
L1C LAND	From EFHK to Lilja. From L1 to EFHK Airport
L1C SEA	From Fager to Sea Waypoint 4
L1C COAST	From Lilja to Fager. From Sea Waypoint 4 to L1

Table 3.6: Product description.

3.6.2.3 LAND SURFACE PARAMETER DATA

During the outbound and inbound legs from and to Helsinki international airport, land targets with diverse cover (from bare soil to forestry, including small lakes) were overflown in both flights. The classification of surface types was based on ECOCLIMAP , i.e. the same surface parameter global dataset which is used for the L2 SM algorithm of SMOS.

Figure 3.15 shows the sections of flight tracks in which the different classes of land were observed by Amiras based on ECOCLIMAP landcover classes.

3.6.2.4 ECOCLIMAP montly LAI (Leaf Area Index)

The monthly averaged LAI from ECOCLIMAP was aggregated to 0.0083333 degree spatial resolution. Figure 3.16 shows the LAI values of June for the land pixels flown by AMIRAS. Most of the pixels were covered by dense forests, with LAI values close to 4.

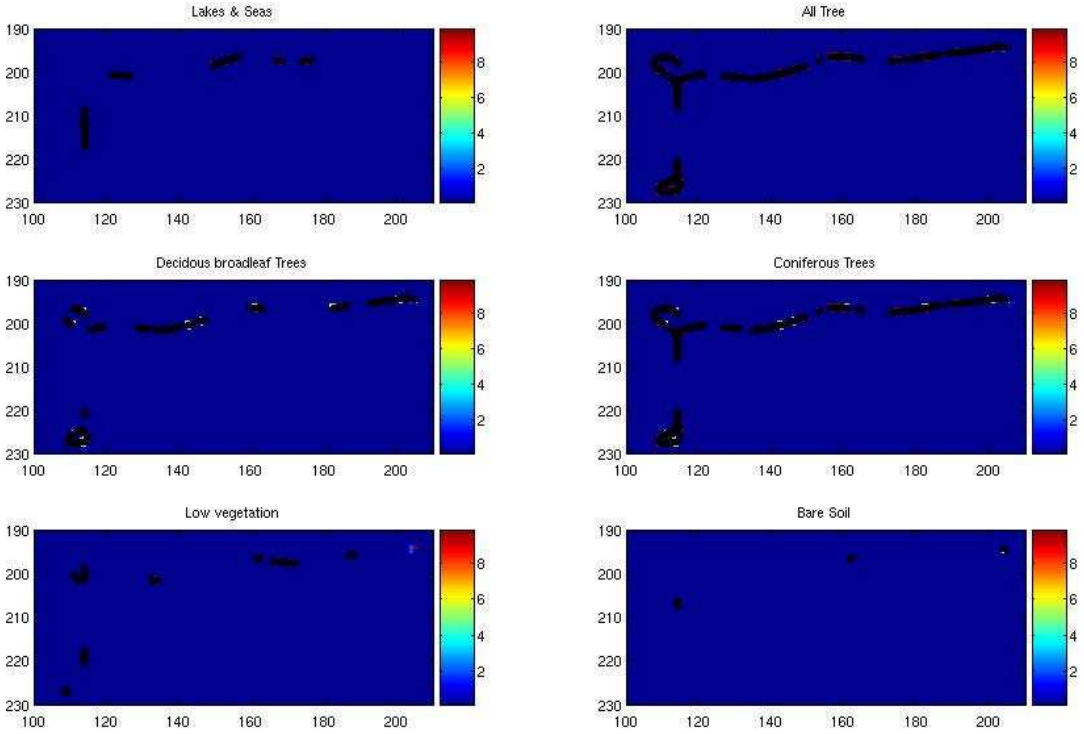

Figure 3.15: Land classes flown by Amiras flight

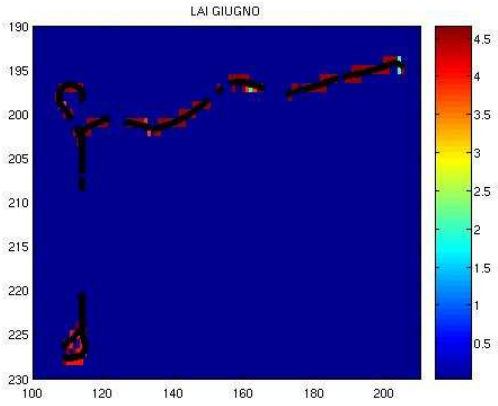

Figure 3.16: LAI values of forests flown by Amiras

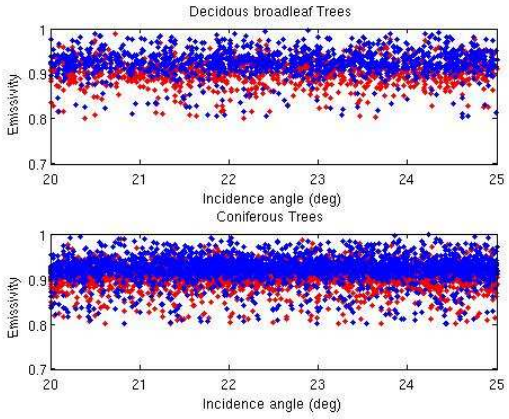

Figure 3.17: Emissivity trends vs. incidence angle in the range between 20° and 25°, blue dot point indicate the vertical polarization, red dot point indicate the horizontal polarization

3.6.2.5 ECMWF database inputs

Values of soil temperature ("skin temperature" for forests) and soil moisture were provided by the European Center for Medium-range Weather Forecasts (ECMWF). Physical soil temperature has been used to compute the experimental value of the emissivity. Soil moisture was used as an input to the model, jointly with LAI.

3.6.2.6 Experimental emissivity values

Brightness temperature data have been derived by AMIRAS files, taking into account the offset suggested for the calibration that have been applied to the L1C product. The results obtained from the L1C product corresponding to the forest areas are plotted in the following figures.

Figure 3.17 shows the experimental trends of emissivity vs. angle in the range between 20° and 25° for the two forest categories present in the area and for values of LAI greater or equal to 4. As expected, the values of emissivity are close to 0.9 and the difference between the two polarizations is low.

In Figures 3.18 and 3.19 the histograms and the mean values of emissivity for the deciduous and coniferous forests, respectively, are presented.

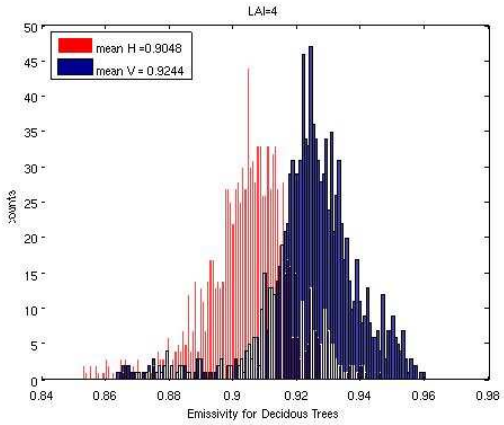

Figure 3.18: Emissivity trends vs. incidence angle in the range between 20° and 25° for deciduous forest

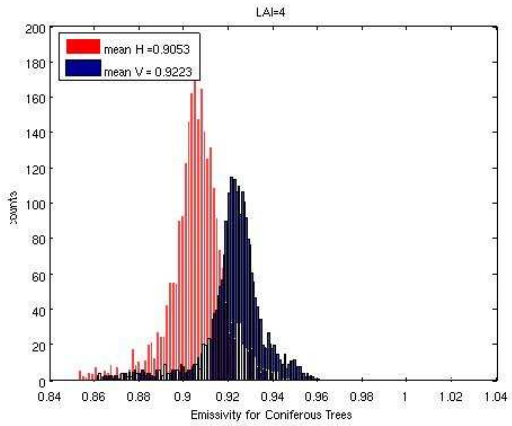

Figure 3.19: Emissivity trends vs. incidence angle in the range between 20° and 25° for coniferous forest

3.6.2.7 Comparison with the Physical Model

The Model used as reference for comparisons with data collected by AMIRAS over forests is described in section 3.2. Using the values of physical temperature and soil moisture extracted from European Centre for Medium-Range Weather Forecasts (ECMWF) data and the corresponding values of LAI for forest areas by ECOCLIMAP, we computed then the values of the emissivity for a range of incidence angles between 20° and 30°. The comparison has been made between measured emissivity values and simulated ones for a range of dbh between 5 and 35 cm and incidence angle between 20° and 30°, and according to the procedure developed in section 3.4.

Figure 3.20 shows for both forest categories, the Emissivity values predicted by the model are close to the center of the histograms of measured values. The experimental data show a slight difference between vertical and horizontal polarization, which is underestimated by the model.

3.6.3 National Airborne Field Experiment 2005

3.6.3.1 Introduction

This section describes model simulation and experimental data for NAFE05 campaign, which are used throughout this thesis to address the problem of soil moisture sensitivity in the presence of forests cover. This data was collected under the auspices of the National Airborne Field Experiment 2005 (NAFE'05), and consisted primarily of airborne L-band observations supported by ground sampling of the top 5cm soil moisture over an area as big as a SMOS pixel. The National Airborne Field Experiment 2005 (NAFE'05) was undertaken across a 4-week period, starting on October 31st and ending on November 25^{th}, in the Goulburn River catchment, located in south-eastern Australia (see Figure 3.21). The study area was a 40km x 40km area characterised by moderate to low vegetation cover (mainly grazing land and crops with a fraction of forest) and gentle topography. The objective of the campaign was to provide simulated SMOS observations using an airborne radiometer, supported by soil moisture and other relevant ground data.

A summary description of this data set has also been published in Panciera et al.(2008a)

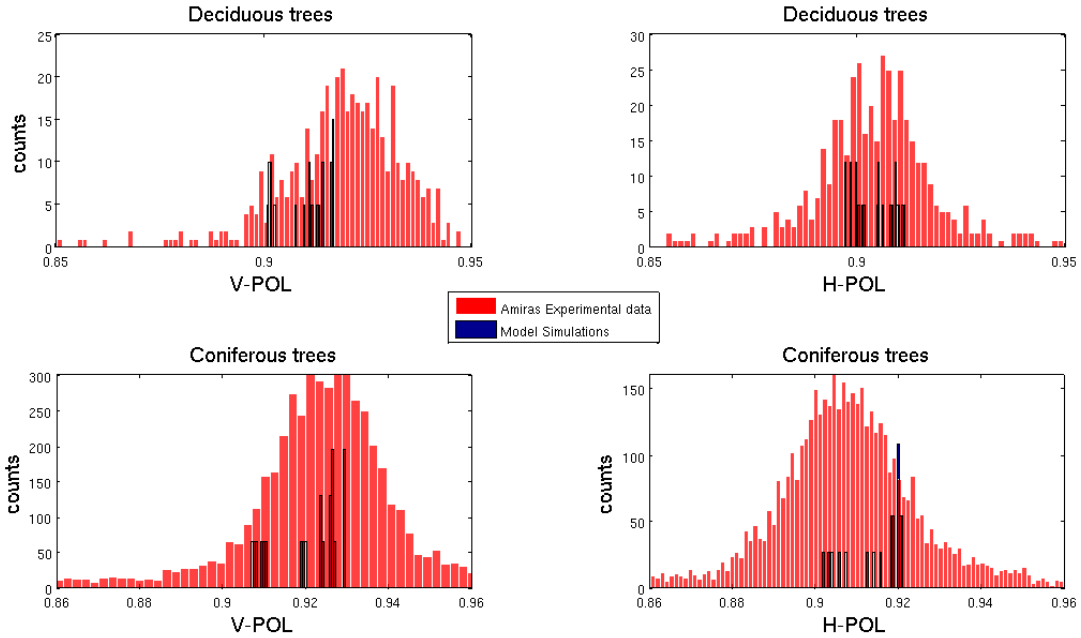

Figure 3.20: Comparisons between simulated histograms of emissivity and the ones measured by AMIRAS radiometer. Upper diagrams: decidous forests. Lower diagrams: coniferous forests. Left diagrams: Vertical polarization. Right diagrams: horizontal polarization

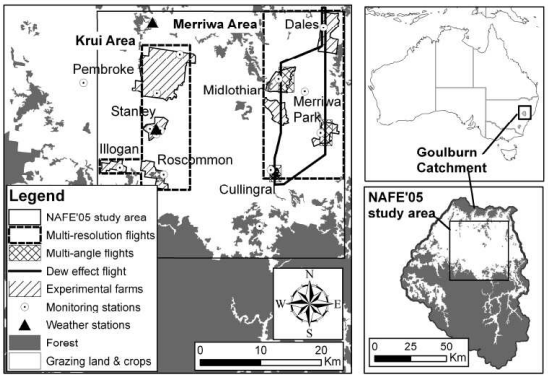

Figure 3.21: Location of the Goulburn catchment and study area (right panels) and overview of the NAFE'05 study area, permanent monitoring stations, experimental farms and flight coverages (left panel).

3.6.3.2 Forest site description

The area of study (lat/lon (32 8' 42" S, 150 6' 43.1994" E) to (32 11' 6" S, 150 9' 7.1994" E)) covered part of the 'Roscommon' farm. This area was part of the larger 'Krui' study area covering the Krui River subcatchment, which lies within the Goulburn River catchment in southeast Australia. The location of Roscommon within the catchment is outlined in (Panciera et al., 2008), while Figure 3.22 shows the farm boundaries, forest areas and flight lines in more detail. The study area has an average elevation of 300 m above sea level and is characterised by native grassland and Eucalypt forest areas. The forested surfaces were generally found on the more steep and rocky parts of the landscape (gently rolling with elevation differences up to 15 m), whereas the flatter parts had been cleared for grazing.

The forest areas consisted mainly of Box (Eucalyptus spp.), Ironbark (Eucalyptus spp.) and some Black Cypress-pine (Callitris endlicheri). Fish-eye photographs were taken of the Eucalypt vegetation, and the LAI was estimated at 2.5. MODIS images showed that forest LAI did not noticeably change during the experiment. The understory was an open-heath formation consisting mainly of Sifton bush (Cassinia quinquefaria). Some litter was present on the ground and formed a generally very thin (0.5 cm) layer. Litter dry bulk density was 0.15 ± 0.05 $g.cm^{-}3$. It is estimated that around 10-15% of the forest floor consisted of bed rock, with the remainder covered by sandy soil (67% sand, 15% clay) with a bulk density of 1.22 $kg.m^{-}3$ and a porosity of 0.437.

3.6.3.3 Data Set

The airborne L-Band measurements used in the current study were made using the dual-polarised Polarimetric L- band Multibeam Radiometer (PLMR) on 1^{st}, 8^{th}, 10^{th}, 15^{th} and 8^{nd} of November 2005. The average soil moisture ranged from 0.184 m3/m3 on the first date to 0.02 m3/m3 on the last date. At lower altitude, the nominal ground resolution (-3 dB footprint) was 62.5 m at nadir. Observations were made every second at incidence angles of +/-7, +/-21.5, +/-38.5, covering a total swath of approximately 375 m. More details about the measurements are given in [Panciera et al., 2008].

This section is aimed at getting an insight into the emissivity properties of the forest. Therefore, we have analyzed radiometric samples with the aid of a Landsat image,

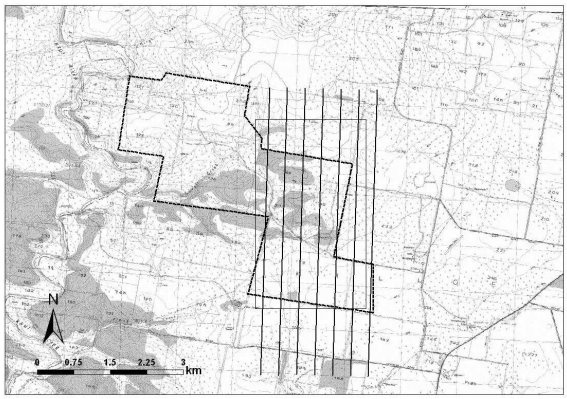

Figure 3.22: Topographic map of the area around Roscommon farm. The farm boundary is given by the dotted line, the thick solid lines show the seven PLMR flight lines at approximately 150 m altitude above ground level and the thin-lined rectangle indicates the approximate study area. The forest areas are coloured in grey.

by selecting the central part of the forest area, which is homogeneous and shows a brightness temperature more stable than in the outer regions.

3.6.3.4 Theoretical simulation

Simulations were made using the forest emission model described in section 3.2. In general, only a limited part of the variables influencing the emissivity are available by ground measurements. For this reason, some inputs are assigned on the basis of relationships derived by literature described in section 3.4.

For the case of Roscommon forest, soil moisture, LAI and litter parameters were made available by ground measurements. The vegetation temperature was measured at different levels, from the soil surface to 7 m height in the trunks. However, only the value at 7m has been used, since differences with measurements at different levels were lower than 2 K at the time of the flights. The height standard deviation of soil roughness was set equal to 1.5 cm. The average dbh was estimated to be roughly equal to 30 cm, on the basis of available photographs.

3.6.3.5 The simple radiative transfer model

Comparisons between experimental data and model simulations were also made by using the simple model being used in the SMOS SM algorithm (Kerr et al, 2007). Description of the model is reported in section 3.5.

3.6.3.6 Results

Figure 3.23 shows a comparison between predicted and measured values of brightness temperature for the five dates. The error bars in simulated data correspond to the range of soil moisture measurements. The agreement is good on 1/11/2005, when the average soil moisture was 0.184 (m^3/m^3). The brightness temperatures measured on 8/11 are almost 10 K higher (on average) than the ones measured on 1/11, although the physical temperature was lower by about 5 K. The model predicts an increase of emissivity, since the soil moisture decreased to 0.127 (m^3/m^3), but this is lower than the increase observed in the experimental data. On this date, the flight took place after a rainfall. The high value of brightness temperature could be related to the effects of raindrops on the vegetation, although the high values of Polarization Index, to be illustrated later, do not agree with this assumption. The problem, which was also found in (Grant et al, 2010), needs to be investigated further.

In the last flights the agreement is generally good, although with a slight underestimation. The overall rms error in the comparison between model simulations and experimental data is equal to 3.7 K. This figure is significantly lower than the dynamic range of brightness temperature, which is of the order of 20 K (cf. fig. 3.24 and 3.25). A different representation of results is given in Figures 3.24 and 3.25, where the angular interval 20°-30° is selected and the brightness temperatures at vertical and horizontal polarization are given as a function of soil moisture. For the experimental data, the figure gives the average values (continuous line) and the standard deviation (error bars). Both experimental and simulated data show a general decreasing trend, which the model mostly attributes to variations of soil moisture, with slight effects due to variations of physical temperature.

A comparison between values of Polarization Index PI is shown in Figure 3.26, considering all angles. The definition of this index is:

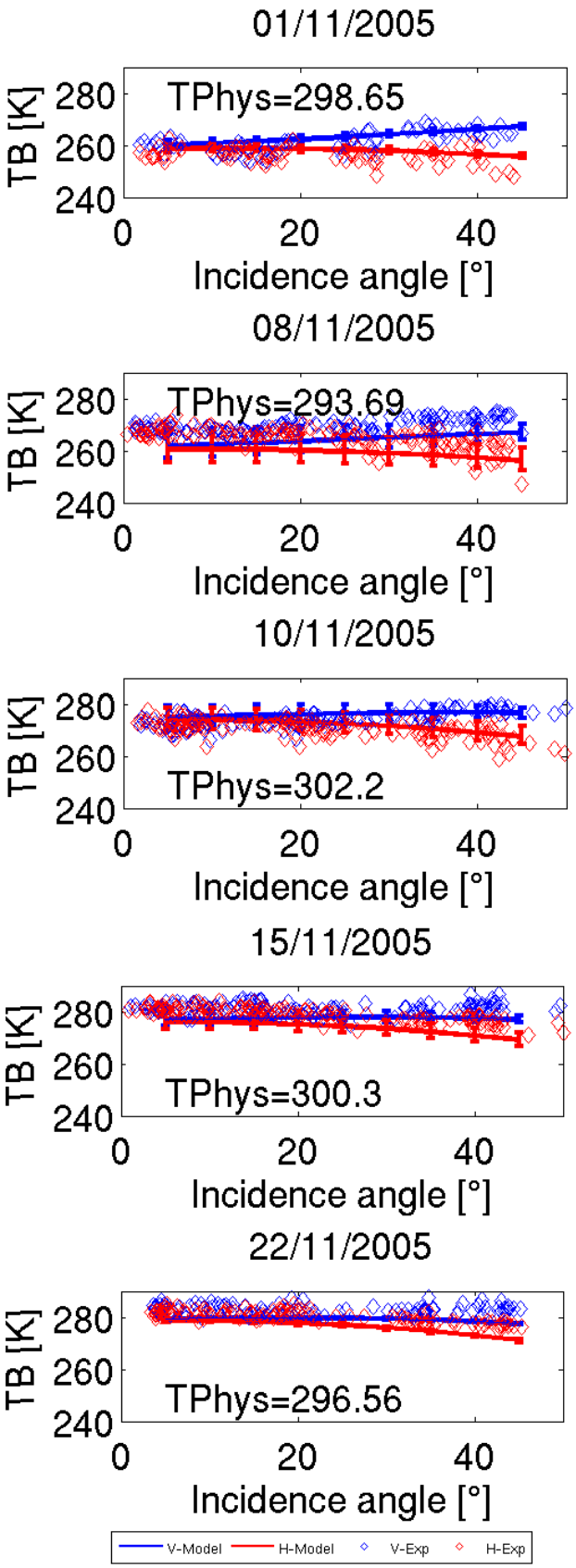

Figure 3.23: general comparison between experimental data (dots) and theoretical model simulations (lines) of brightness temperature TB[K]. Polarizations: vertical (blue), and horizontal (red). TPhys = physical temperature [K].

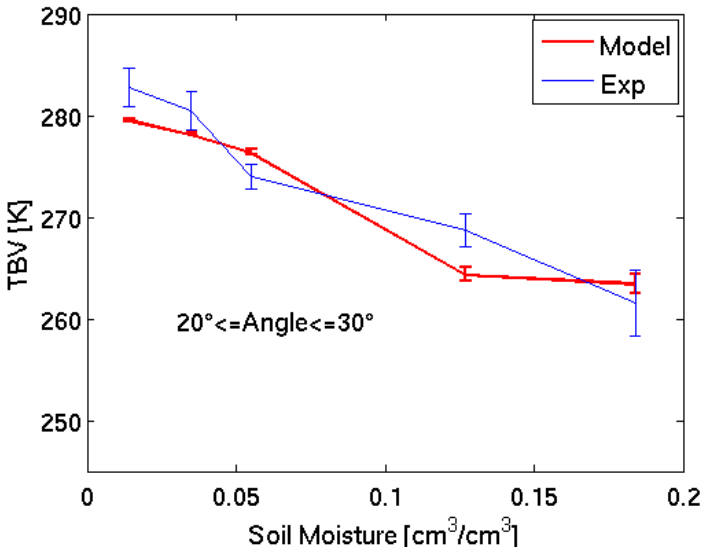

Figure 3.24: Vertical brightness temperature (TBV) vs. soil moisture. Angles 20°-30°. Experimental data (blue) and theoretical model simulations (red).

$$PI = \frac{2(TB_v - TB_h)}{(TB_v + TB_h)} \tag{3.33}$$

It is not influenced by the physical temperature. A specific comparison as a function of soil moisture is shown in Figure 3.27.

Previous theoretical and experimental studies indicate that PI increases with soil moisture (see, e.g Paloscia et al, (1993)). A specific comparison as a function of soil moisture is given in Figure 3.27. Since the PI is more significant at the higher angles, the interval 30° - 40° was selected. The model reproduces the absolute values of PI and its increase with soil moisture.

Figure 3.28 shows comparisons between measured and simulated brightness temperature using the simple model. Also the case of absence of litter is considered. The trends are similar to the ones obtained by the Tor Vergata model (Figure 3.23). However, the predicted temporal variations of brightness temperature are slightly lower than the measured ones. The overall rms errors are equal to 4.5 K without litter and 5.4 K in the presence of litter. However, it should be noted that in the simple model litter parameters are general, and not based on Roscommon measurements. Also, the

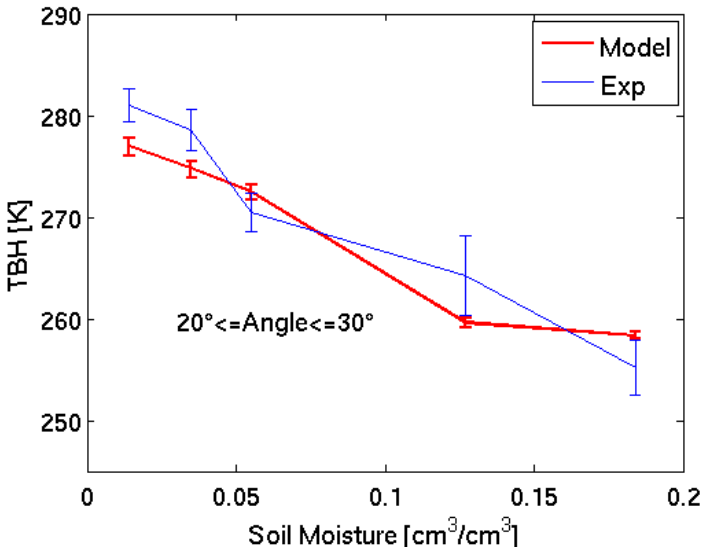

Figure 3.25: Same as in figure 3.24 for horizontal brightness temperature (TBH).

assumption to have a unique albedo for all deciduousforests reduces the accuracy with respect to the theoretical model.

3.6.3.7 Conclusions

Some main conclusions can be drawn by the presented work.

1) The reduction in sensitvity to soil moisture variations by crown attenuation depends not only on forest biomass but also on the average dimensions of forest elements (trunk and branches). For given bomass, higher values of attenuation are obtained in the presence of several trees with small trunk diameters. Further attenuation of soil emission is produced by litter and understory.

2) For developed forests, the average trunk diameter plays a strong influence on the emissivity at L-band. This can be a problem in the application of retrieval algorithms based on simple models. On the other hand, it could give the opportunity to identify areas dominated by old large trees.

3) In the Roscommon forest, characterised by moderate biomass and a thin litter layer, radiometric measurements give a dynamic range of about 20K, mostly related to soil moisture variations. The theoretical model reproduces the experimental data with an

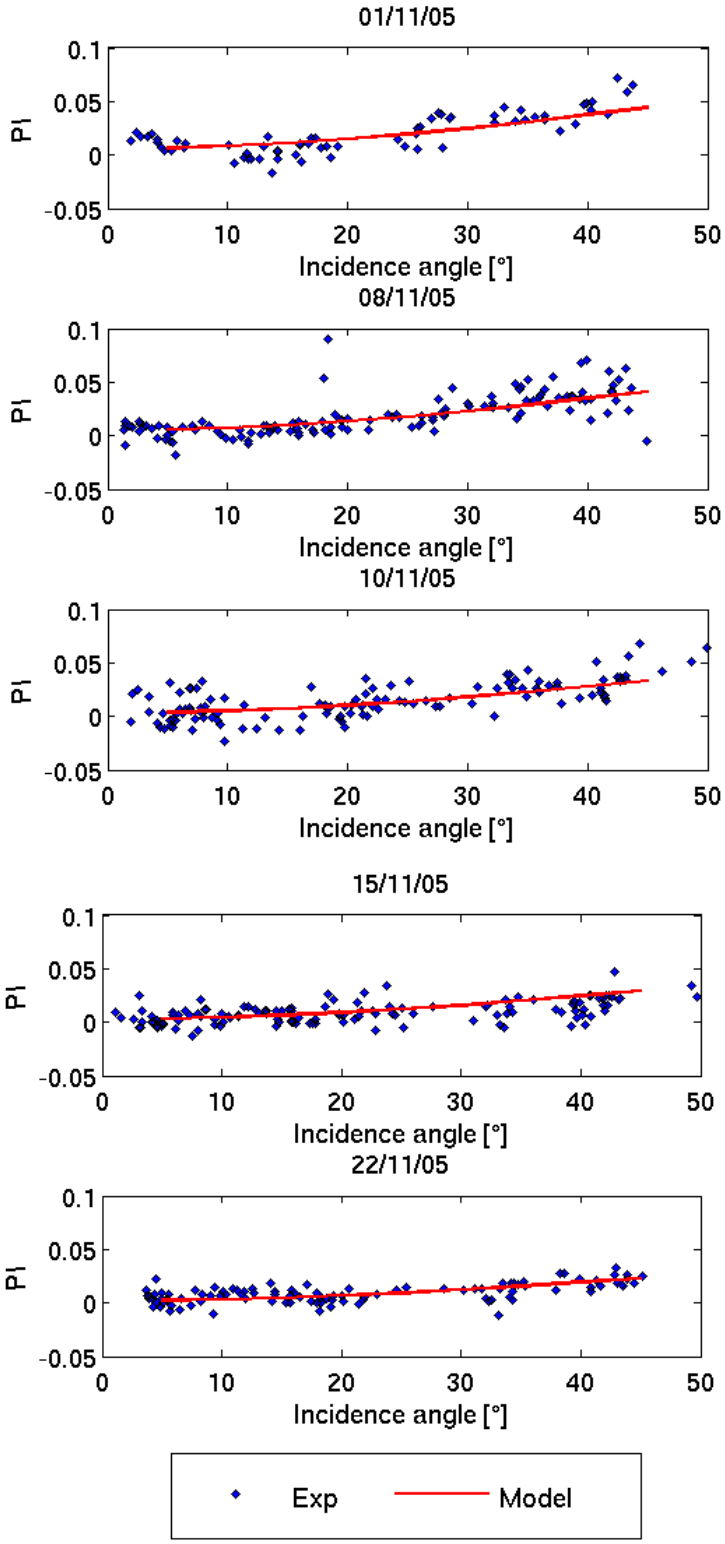

Figure 3.26: General comparison between experimental data (dots) and theoretical model simulations (lines) of Polarization Index.

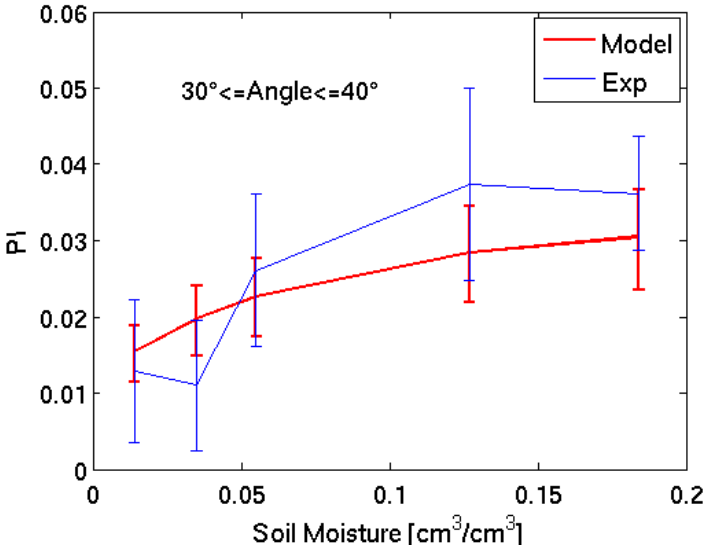

Figure 3.27: Polarization index vs. soil moisture. Angles 30-40. Experimental data (blue) and theoretical model simulations (red)

error of 3.7 K, which is low with respect to the dynamic range. Moreover the simple model generally reproduces the experimental data, but the dynamic range is slightly underestimated and the rms error is higher than in the case of the theoretical model.

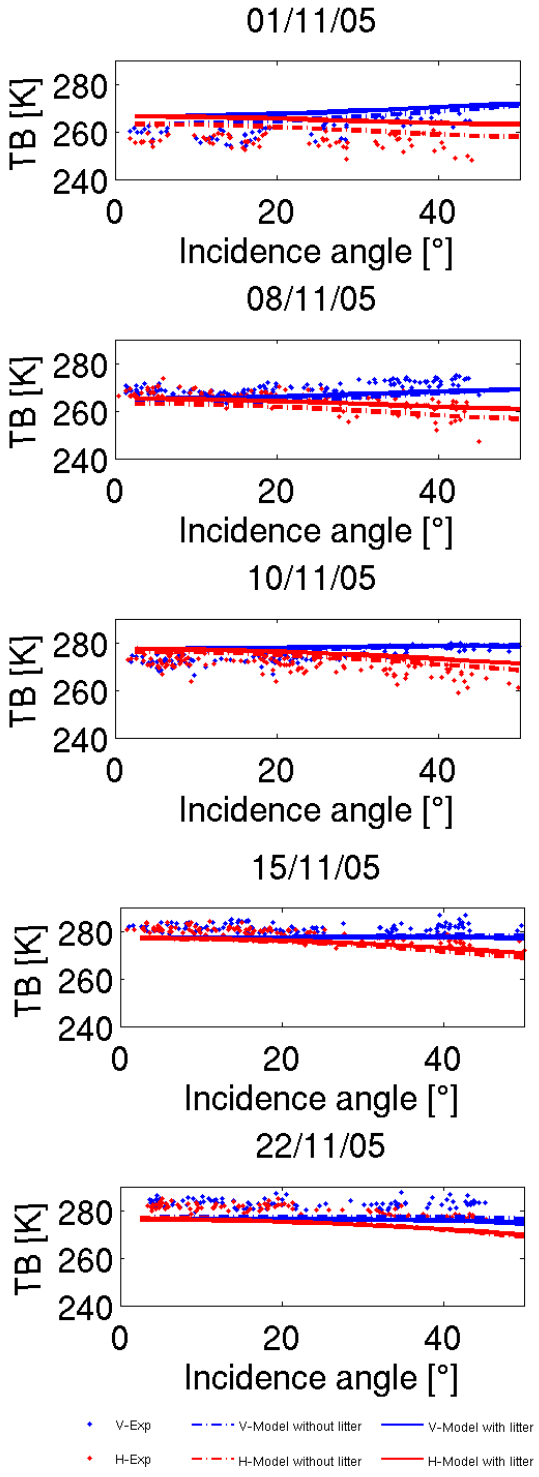

Figure 3.28: General comparison between experimental data (dots) and simple model simulations with litter (continuous lines) and without litter (dashed lines) of brightness temperature. Polarizations: vertical (blue), and horizontal (red)

4

The Effect of Rain Events on AMSR-E Signatures in Subtropical Chaco forest in Argentina

The present chapter and the following one analyze data collected by spaceborne radiometers with the aid of the previously described physical model. The main objective is to investigate the sensitivity of forest to variations of soil properties, mostly related to rainfall.

The present chapter considers AMSR-E data, while Chapter 5 considers first SMOS data collected in 2010.

4.1 Introduction

In the recent years, the availability of AMSR-E signatures offered new opportunities [Tawanishi et al, 2003]. This sensor spans a wide range of frequencies, from 6.925 GHz to 89.0 GHz, and the spatial resolution is substantially improved with respect to previous ones. Lower frequencies are more suitable for terrestrial applications, while higher frequencies, i.e. 23.8 GHz, 36.5 GHz and 89.0 GHz, are influenced by atmospheric water vapor and clouds. A conical scanning is used to observe the terrestrial surface with a local angle of 55°. Based on AMSR-E data, useful algorithms have been developed to retrieve soil moisture [Njoku et al, 2003], [Paloscia et al, 2006] and vegetation variables [Njoku et al, 2006].

This chapter, considers AMSR-E signatures of a large dry forest (Chaco forests, Argentina) which were collected in 2006-2007. The objective is to describe and explain the

effects on selected AMSR-E channels of the rainstorm events, occurred in the area.

The study area is located in the Semiarid Chaco subregion, in northwestern Argentina. The climate of this area is subtropical with a dry season. Mean annual temperature is 26 ° C, with mean temperatures of 30 ° C and 18 ° C for the hottest (January) and coldest (July) months, respectively. The mean evapotranspiration is 15 mm h^{-1} and the mean annual precipitation is 900 mm. Annual rainfall is low, with a strong pattern of monsoonal seasonality occurring mainly between November and March. The forest shows a considerable variation in tree basal area, ranging from $5 - 15m^2\ ha^{-1}$ [IDIA]. The main economic activities are cattle ranching, often within the forest, and charcoal production for local use, while cultivation is limited by scarcity of rainfall and restricted to specific areas [Grau et al, 2005].

In the analysis, we have used the Polarization Index PI, which is defined as:

$$\mathbf{PI} = \frac{(\mathbf{TB_v} - \mathbf{TB_h})}{0.5.(\mathbf{TB_v} + \mathbf{TB_h})} \tag{4.1}$$

TB_v and TB_h are the brightness temperature values collected at vertical and horizontal polarization, respectively. This index has been evaluated at C band and X band.

4.2 Analysis of a rainfall event in "Bajos Submeridionales"

In the lower part of Chaco forest ("Bajos Submeridionales"), a strong rainstorm occurred on October, 3, 2006. It is estimated that the amount of rainfall was between 50 and 150 mm. Since the event occurred after a long dry period of time, it is estimated that the variation of soil properties were very strong.

General maps of PI at C band are shown in Figure 4.1. The maps are based on AMSR-E observations of September 18 (before the rainstorm) and October 4 (after the rainstorm). The box indicates a region covered by a continuous forest, and the dots refer to sites where measurements of tree density, dry biomass and distribution of trunk diameters are available. Measurements were provided by the Forest Evaluation System Management Unit (UMSEF) (http://www.ambiente.gov.ar/). The distance between points corresponds to about 0.5° in longitude and latitude. This PI map is extended to a large region, and the color scale is selected in order to detect PI values as high as 0.15. It is evident that, in the South East part of the area, mostly covered by herbaceous low vegetation, the PI showed very high increases after the rainstorm. However, it is difficult to appreciate variations within the forest, with this scale.

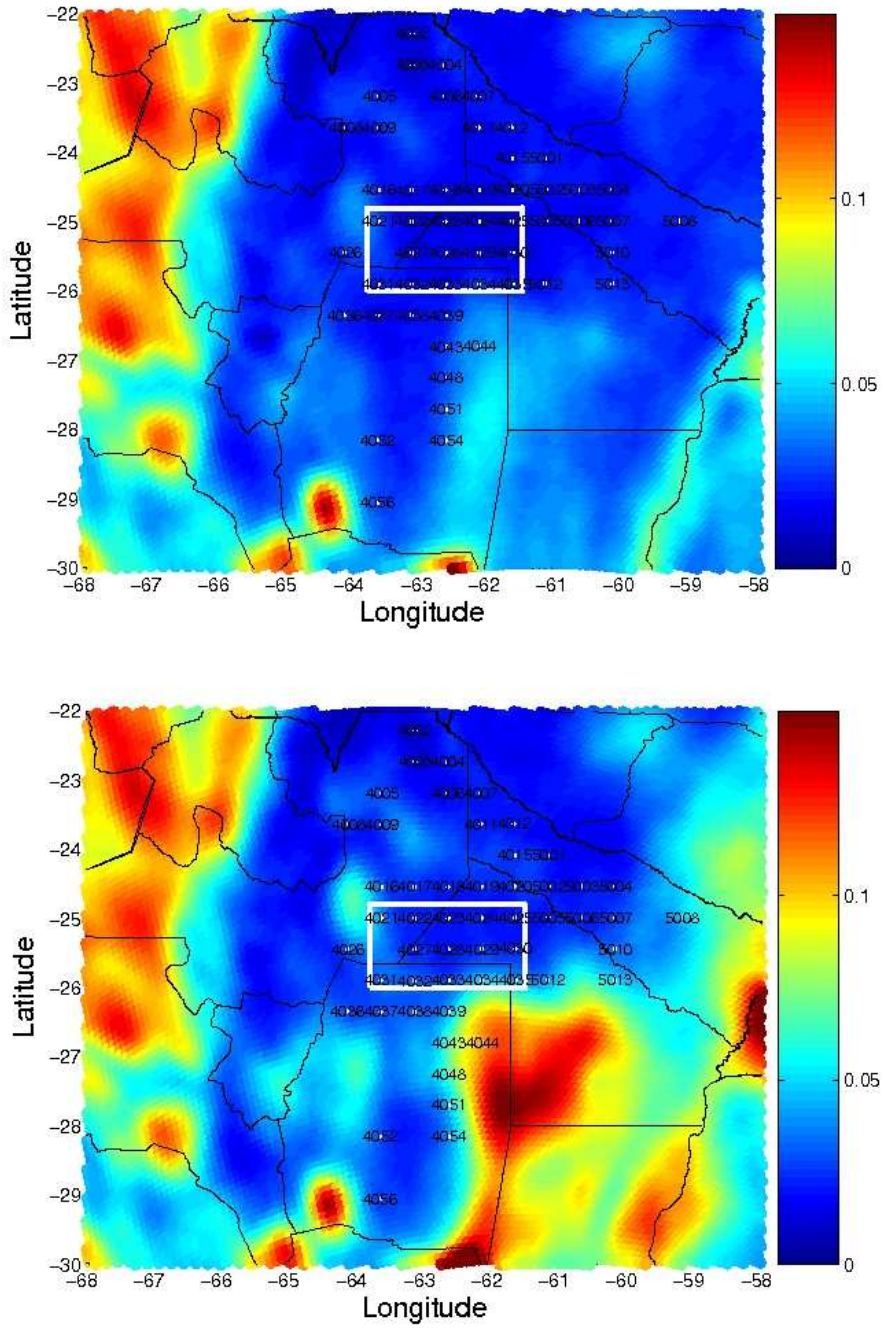

Figure 4.1: Maps of PI at C band in the Chaco forest. a) September 18 (before rain). b) October 4 (after rain). The continuous forest is indicated by the white box. White dots indicate sites of measurements..

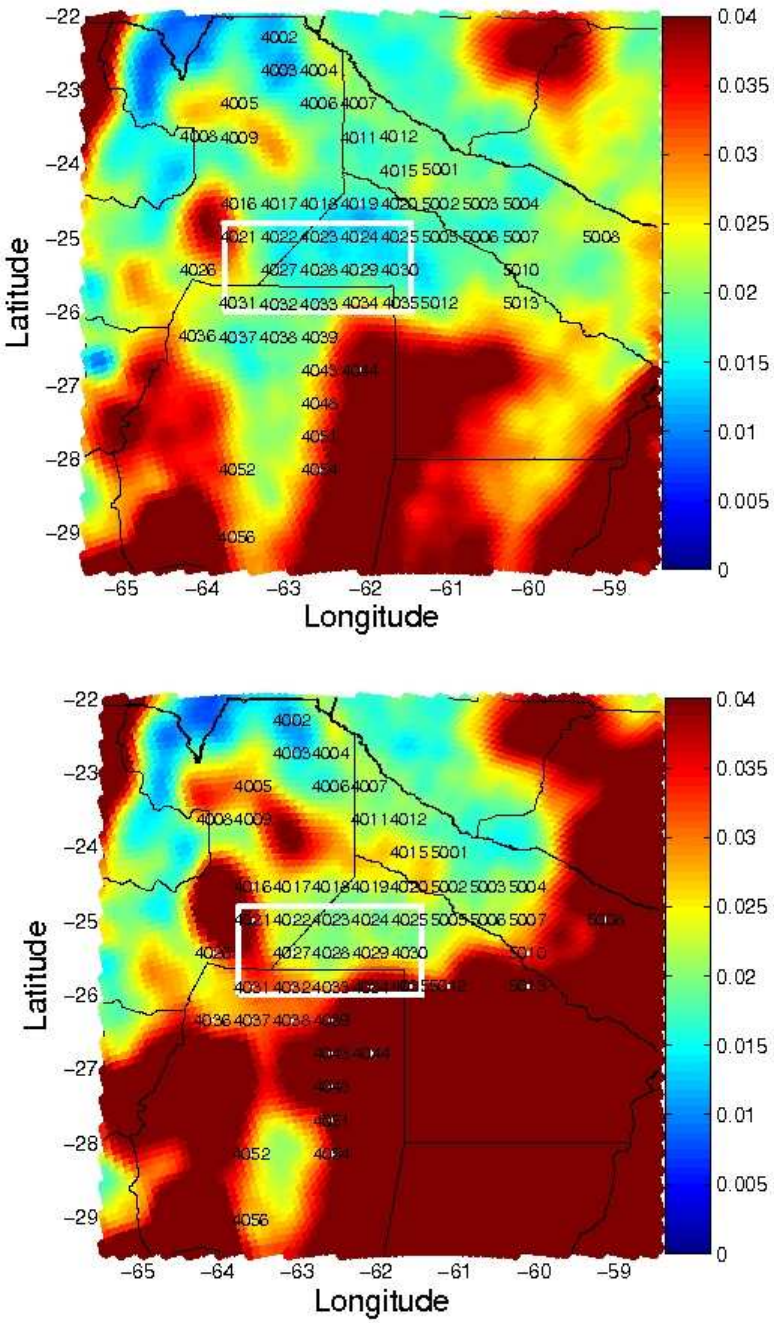

Figure 4.2: Specific maps of PI at C band in the Chaco forest. a) September 18 (before rain). b) October 4 (after rain). The continuous forest is indicated by the white box. White dots indicate sites of measurements..

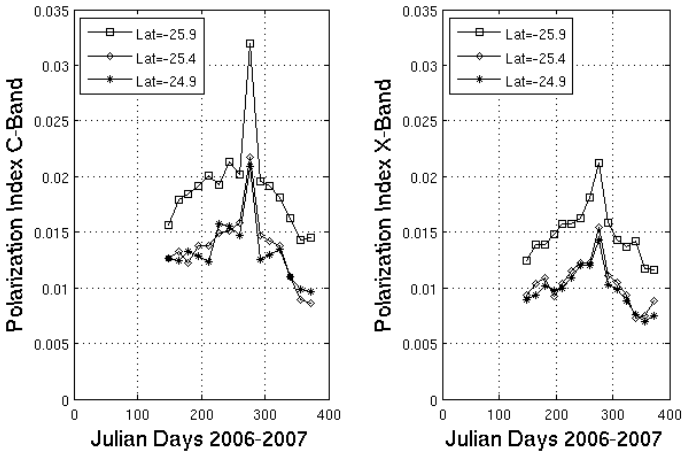

Figure 4.3: Trends of Polarization Index within the Chaco forest at three latitudes. Left: C band. Right: X band.

In Figure 4.2, the comparison between the C band PI's of the same dates is shown by using a more detailed map and a scale which saturates when the PI is equal to 0.04. With this representation, appreciable variations are observed even within the continuous forest, especially in the Southern part. Before the rain event (September 18), the PI is quite uniform within the rectangular box. Although the ground measurements indicate that the biomass varies in a range between about 70 and 110 t/ha, the effects on PI of this biomass variation cannot be appreciated. It must be considered that measurements were carried out in specific locations, while the coarse resolution of the instrument creates a smoothing effect. After the rain event, a general increase of PI is observed in the whole area, associated to a gradient from the Southern to the Central part of the forest.

In Figure 4.3, the trends of PI vs. time are represented for a period of about 200 days. The PI was estimated by averaging over forest pixels belonging to the same latitude. Three latitudes, i.e. -25.9°, -25.4° and -24.9°, have been considered. The first latitude is just at the edge of the forest, while the other two correspond to internal parts. A peak on Day of Year 277 (i.e. October 4) is well evident for the samples of the lower latitude and, to a lesser extent, for the other samples. After the rain event, the PI values decrease again to values close to the ones they had before the event. For sake of comparison, the trends of PI at both C band and X band, are shown, for the same pixels. The trends of X band are similar to the ones of C band, but with a lower dynamic range due to the higher canopy attenuation.

Anyhow, this comparison confirms the assumption that the effect is related to a change of soil properties after the rainstorm, and is not due to eventual artifacts (e.g RFI) of C band channel.

4.3 Analysis of two events in Las Lomitas area

A more detailed analysis was carried out on the area surrounding the city of Las Lomitas. A map is shown in Figure 4.4. This selection was based on: (i) the availability of daily precipitation data, (ii) the existence of large and continuous forest patches and (iii) the fact that basic forest properties of the area are routinely measured by the Unidad de Manejo del Sistema de Evaluacin Forestal (UMSEF). The natural vegetation of the area is a subtropical dry forest dominated by Schinopsis lorentzii (Griseb.) Engl.; Aspidosperma quebracho-blanco Schltdl. and Bulnesia sarmientoi Lorentz ex Griseb. associated with other species like Ziziphus mistol Griseb., Caesalpinia paraguayensis (D. Parodi) Burkart; Prosopis alba Griseb. and Prosopis nigra (Griseb.) Hieron. (Cabrera, 1976). The most common species of the highest stratum are perennials (B. sarmientoi and A. quebracho-blanco) and semideciduous (S. lorentzii), while those in the lowest one are deciduous (e.g., Z. mistol, Prosopis spp. and C. paraguarensis) [Gimenez et al, 2003].

A summary of the available information about Las Lomitas area is presented in Table 4.1.

Variable		Value
Mean basal area (sum of trunk at 1.3 m height) [m^2/ha]		10.55
DBH (Diameter at Breast Height)[cm]	5-10 cm	390+/-70
	10-30cm	103+/-37
	30-50cm	41+/-15
	50-70cm	7+/-4
	70-100cm	1
	≥ 100	0
Mean Above Ground Biomass (t/ha)		100 +/- 12.7

Table 4.1: Summary of available information about Las Lomitas Station

As illustrated in Figure 4.5, the most intense rain events occurred on 21/1/06 and on 5/12/07. They produced 15% and 11% of the annual precipitation, respectively.

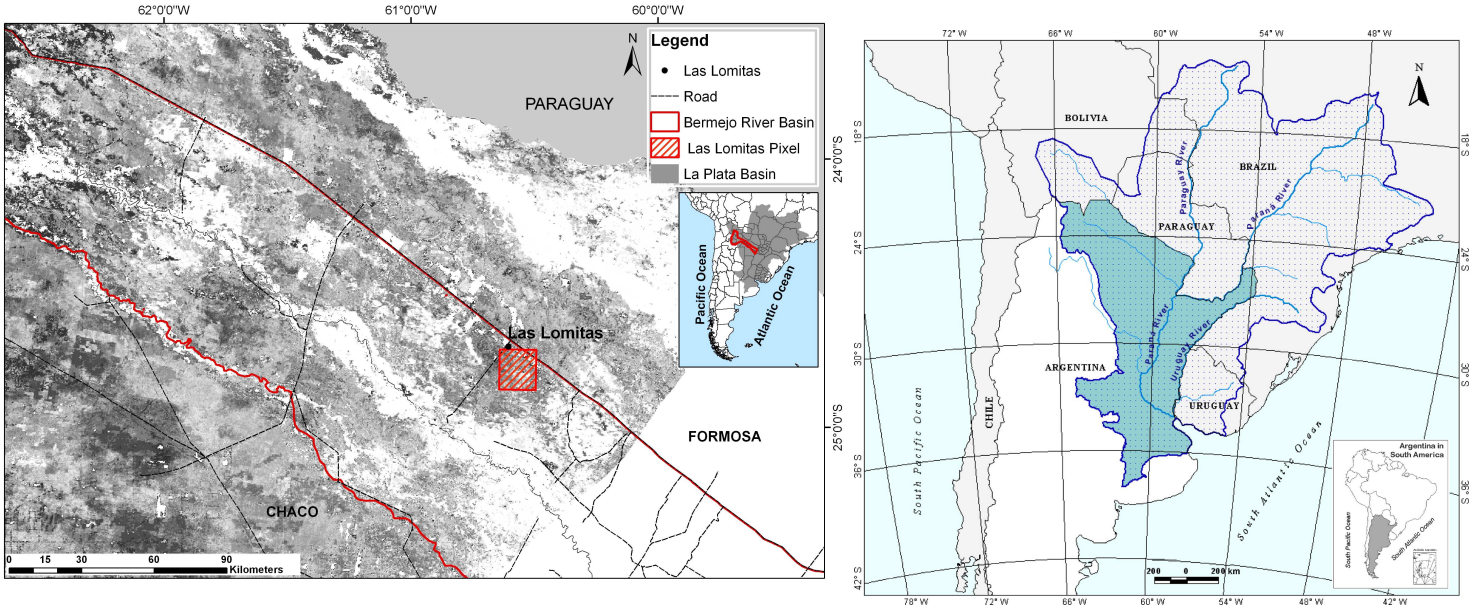

Figure 4.4: Map of the study area, superimposed to a biomass map. A land cover map of the study area is superimposed, showing the coverage of the main ecosystems present in the study area.

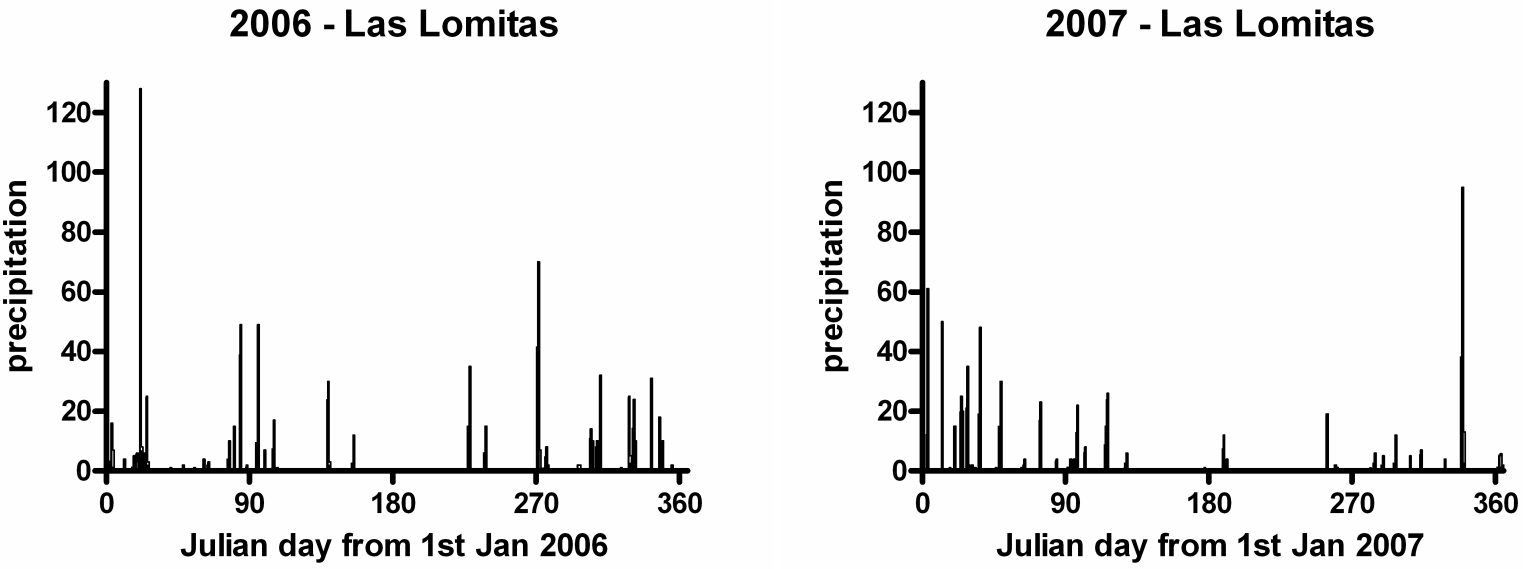

Figure 4.5: Daily precipitations in the study area.

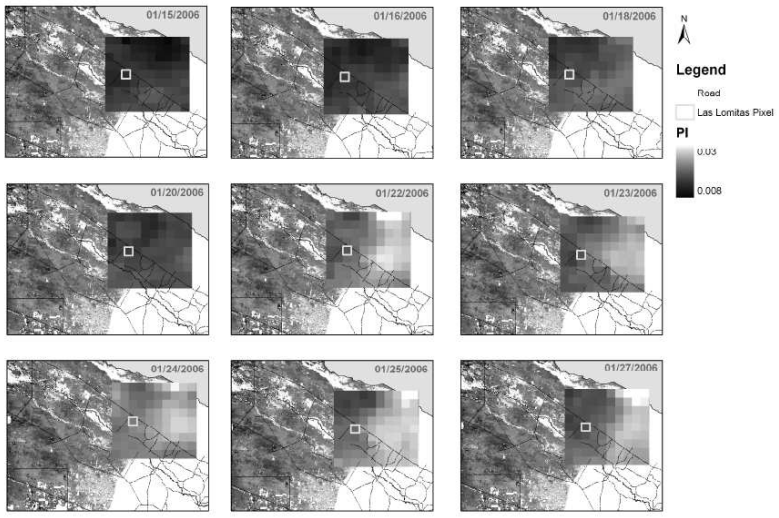

Figure 4.6: Multitemporal AMSR-E C Band PI map of Las Lomitas area for the rain event on January 21st, 2006.

A multitemporal C Band PI maps of the area are shown for the two other rain events of 21-1-06 and 5-12-07 in Figure 4.6 and Figure 4.7.

Both maps show AMSR-E observations prior and after the rain events. An increase in the PI of the whole area is evident after the rainstorms. Since the plotted area is large, and the precipitation is measured at point locations, it is important to assess if the rain event included the whole area. To this end, we applied the procedure developed in [Kyoung-wook et al, 2006] to evaluate the rain condition of an area using as input the brightness temperature values at 89 GHz. The procedure is based on the condition that the Tbv of a raining pixel should obey the relation Tbv (89 GHz) $<$ 270 K [Kyoung-wook et al, 2006] which is satisfied in the central pixels of Las Lomitas area for the event of 21/1/06. Therefore, the raining event at this date was spatially large, of the same spatial extent of the observed patches of PI of Figure 4.6 and 4.7.

To perform a specific quantitative estimate of C band PI sensitivity, we have chosen an area of the size of an average C Band AMSR-E pixel near Las Lomitas which does not include the city (exact location: 24 ° 35m 7.8s S, 60 ° 28m 2.7s W, area 45 x 80 Km). This selection is based on the availability of in situ measurements, up to date information about precipitation

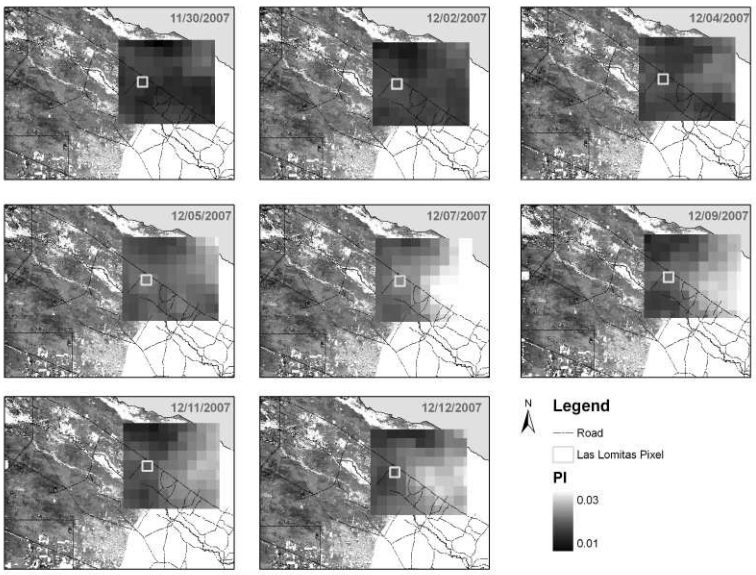

Figure 4.7: Multitemporal AMSR-E C Band PI map of Las Lomitas area including the rain event of December 5th, 2007.

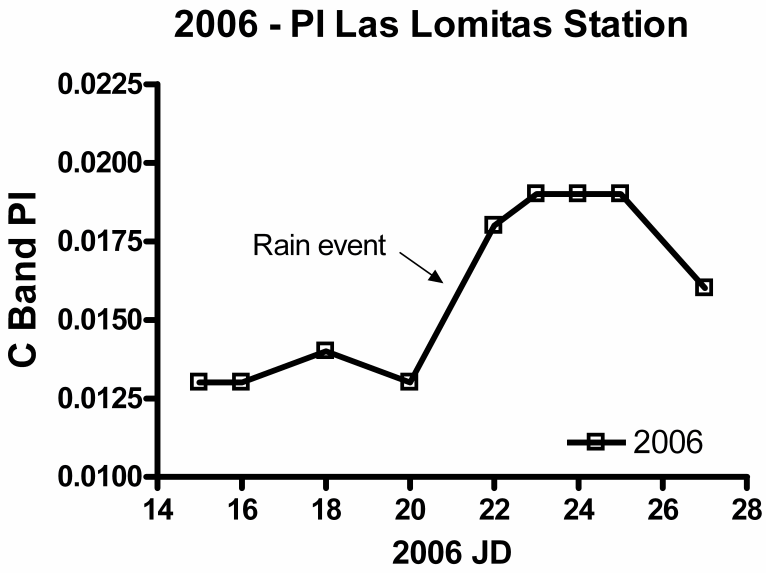

Figure 4.8: C Band PI trend of Las Lomitas station for the days before and after the rain event occurred on January 21st, 2006.

and forest condition (see Table 4.1), and by the fact that this area is continuously covered by forest with an average biomass of 100 t/ha (see Figure 4.4). In Figure 4.9 and 4.10, the C Band PI trends corresponding to this area are shown for a period of 10 days both before and after the events.

An increase on the day after the rain event is observed for both cases. These increases are significant, in the sense that produces an appreciable variation with respect to initial conditions. Roughly, the PI changes from 0.0125 to 0.02. Since the effects of the atmosphere are negligible at C band, these changes in the PI should be related to changes in the landcover type or condition. The temporal variation of the trend shows a rapid increase of PI after the rain, and then the PI returns to its initial value after 7 days. This is consistent with a change of soil status, since other phenological effects are not capable of changing the PI so steeply and in a reversible way. Therefore, the most conservative explanation is that the PI changes due to changes in SMC after rain. As an example of the typical PI behavior in this area, we show the temporal trend for a two week period when very low rain (< 4mm) were recorded (Figure 4.11)

The severe rainstorms produced variations of polarization index which are not negligible,

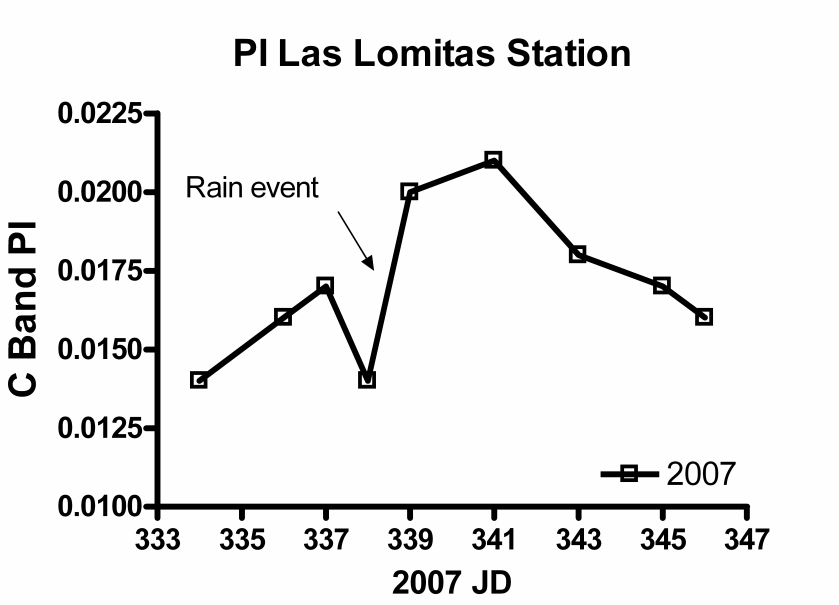

Figure 4.9: C Band PI trend of Las Lomitas station for the days before and after the rain event occurred on December 5th, 2007.

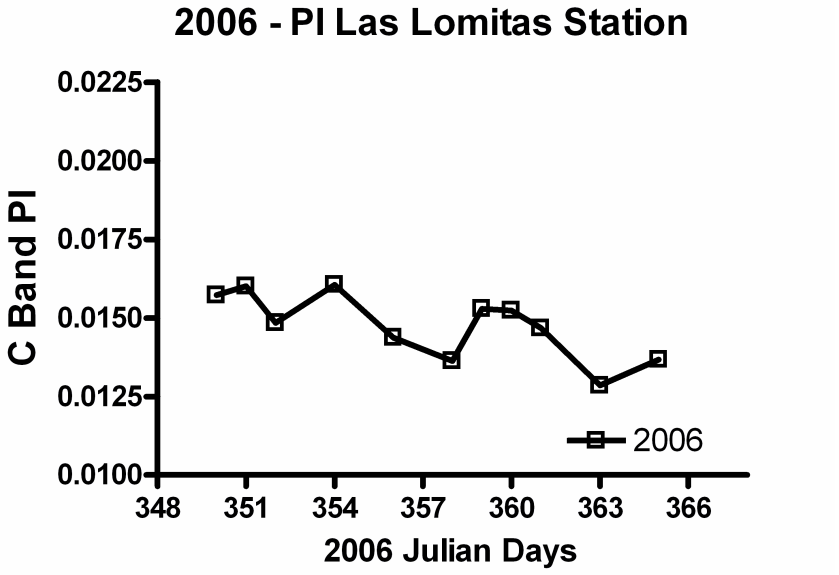

Figure 4.10: C Band PI trend of Las Lomitas station for the days before and after the rain event occurred on December 5th, 2007.

although moderate. This result can be justified by some considerations. First of all, the forest was continuous, but not very dense. Ground measurements indicated that the biomass ranged between about 70 t/ha and 110 t/ha. Moreover, the rain events occurred after a long dry period. Therefore, it produced a strong variation of soil conditions.

4.4 Model simulations

In order to interpret the observed trends of PI, the discrete forest model described in [Ferrazzoli and Guerriero] has been used to simulate the variations of PI with soil moisture. The model has been run for a dry biomass DB0 = 100 t/ha and the distribution of dbh given in Table 4.1.

The properties of woody material have been taken by INTI-CITEMA catalogues. It is important to note that most of the trees in the area belong to species characterized by heavy density wood, such as Aspidosperma quebracho-blanco, Schinopsis lorentzii and Bulnesia sarmientoi. For Aspidosperma quebracho-blanco, the following densities (weights over fresh volume) are given by:

Fresh matter: W = 1100 kg/m^3

Dry matter: WD = 875 kg/m^3

We have used these values for the whole forest, since small differences are present between the dominant species, i.e. Schinopsis lorentzii and Bulnesia sarmientoi. According to well known formulas summarized in Section IIB of [DellaVecchia et al, 2010], we have:

Water fraction by weight in wood: VM = 0.204

Dry matter density: D = 1129 kg/m^3

The Leaf Area Index has been set equal to 1.5, according to information available in ECOCLIMAP data base. Using these data, the other canopy variables required by the model as input have been derived according to the procedure given in [Della Vecchia et al, 2010].

According to literature [Gasparri et al, 2005], there is some litter in Chaco (most dried leaves and some small branches), and this should have non negligible effects on soil emissivity. For the litter, we have adopted the layer model described in [Della Vecchia et al, 2007] assuming to have a litter biomass equivalent to two years of litterfall. Information about soil roughness is not available at the scale of AMSR-E pixels. Simulations have been done under three assumptions about the standard deviation of surface height : 1 cm, 1.25 cm and 1.5 cm. The correlation length L has been set equal to 5 cm.

The volumetric soil moisture has been varied between 0 and 30 %. The left side of Figure 4.12 shows the simulated trends of PI as a function of volumetric SMC. A direct comparison between measured and simulated values is not possible, due to the unavailability of detailed information about soil moisture and roughness at the scale of AMSR-E signatures. However, the simulations can give realistic explanations for the variations of PI. The range of measured PI values (0.0125 to 0.02) is close to the range of simulated ones for the intermediate case of equal to 1.25 cm. Variations of σ have moderate effects in case of a dry soil, while are important for higher values of SMC. It is possible that rainfall produces a smoothing of the soil surface, besides an increase of SMC.

The right side of Figure 4.12 shows the trends of emissivity as a function of SMC. Variations are moderate, but can be detected. Model simulations indicate also that the transmissivity of the canopy at C band is about 0.5 at horizontal polarization and 0.45 at vertical polarization. This confirms that an appreciable, although moderate, contribution of soil emission is present, in agreement with results of previous works. Due to the low value of Leaf Area Index, the attenuation is mostly due to branch effects. Both previous experimental results [Santi et al, 2009], and model investigations [Ferrazzoli and Guerriero, 1996] confirm that branch attenuation dominates at L band, but increases slightly with frequency.

In summary, model simulations confirm that the increase of PI with SMC variations is moderate, but detectable, although signatures are at C band and the forest is continuous. There are two main explanations for this result. First of all, the forest is located in a sunny region, and both events occurred on summer. Furthermore, the diagrams of Figure 4.5 indicate that only minor rainfalls occurred in the antecedent days. Since evapotranspiration is high, this implies that the soil is very dry before precipitation events. Therefore, it is expected that the SMC before the rainfalls was low, and the diagrams of Figure 4.9 indicate that the increases of SMC can be more easily detected if initial values are lower.

A second important property of Chaco forest is related to the characteristics of woody matter. The wood of the main trees present in this area (like Quebracho Blanco) is harder with respect to other species. Therefore, the ratio between volume and dry biomass is lower. A biomass of 100 t/ha corresponds to a volume of only 114 m^3/ha, which produces a moderate attenuation. Therefore, the results of this study cannot be easily generalized to other forests. However, they are important, due to the extension and the environmental importance of the considered area. Furthermore, there are other dry forests around the world, which present

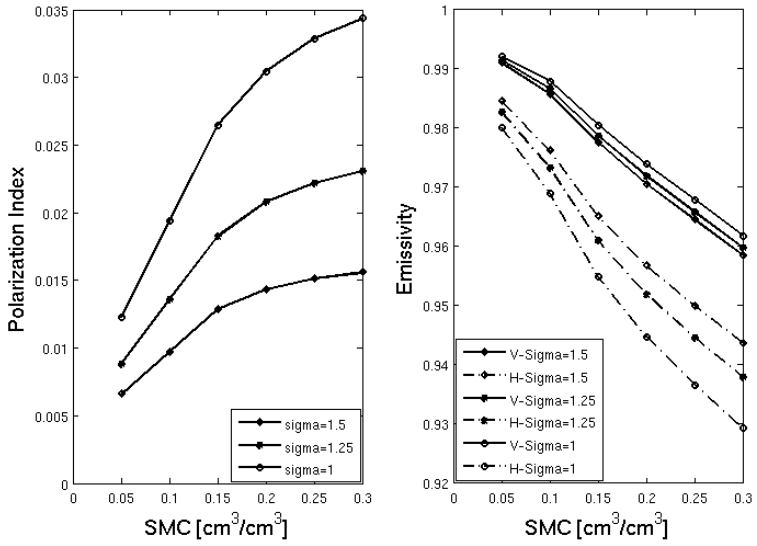

Figure 4.11: Model simulation results. A) C Band PI as a function of volumetric SMC. B) emissivity at V and H polarization (continuous and dashed lines, respectively) as a function of SMC.

similar forest characteristics and structures, such as: Chiquitano in Bolivia; Cerrado in Brasil; Mesquite in North America and Miombo in Africa.

4.5 Conclusion

In this chapter were analyzed three rain events in the Chaco forest as seen by the C Band channel of AMSR-E. The events were big (> 100 mm/day) and occurred after a dry period. In an area near Las Lomitas a significant change in PI after the rain event was observed. Using ancillary data and considerations about the spatiotemporal characteristics of the observed signatures, change in PI was associated to a change in soil moisture. Using field data about the forest structure and reasonable assumptions about the soil status prior and after the events, explained these changes were explained using model simulations.

These results indicate that there is some potential to monitor variations of SMC using AMSR-E signatures, at least in dry forests with moderate woody volume. I expect to find a better sensitivity, even with less intense rain events, by a long term multitemporal signatures of SMOS at L-band. In fact, although the variation of canopy transmissivity with frequency

is moderate, the emissivity of the soil and the litter is expected to be much more sensitive to SMC, at L-band.

4. THE EFFECT OF RAIN EVENTS ON AMSR-E SIGNATURES IN SUBTROPICAL CHACO FOREST IN ARGENTINA

5

Sensitivity to soil moisture variations of SMOS signatures over forests

5.1 Introduction

The Soil Moisture and Ocean Salinity (SMOS) mission of the European Space Agency (ESA) was launched on 2 November 2009 from the Plesetsk Cosmodrome, 800 kilometres north of Moscow. Over land, SMOS will attempt to retrieve soil moisture with a maximum error of 4 % by volume and global soil moisture maps will be provided with a temporal resolution of 2-3 days. SMOS is carrying a fully polarimetric L-Band (λ = 21cm, f=1.4 GHz) Microwave Imaging Radiometer using Aperture Synthesis (MIRAS). The passive microwave observations are collected at multiple viewing angles between 0° and 55° angles, and with a spatial resolution ranging from 35 Km at nadir up to 50 Km (Kerr et all.2001, Barr et al., 2008). The multiple-angle configuration allows us to achieve a significant improvement in retrieval accuracy when compared to the one of previous missions. SMOS mission requirements are summarized in Table 5.1

In this chapter, we investigate the capability of SMOS to monitor soil moisture over forests of South America, and Central Africa.

Global coverage	80North/South latitude
Spatial resolution	50 km
Revisit time	3 days
Swath width	1050 km to 640 km
SM accuracy	4%
OS accuracy	1.2 psu
Nominal (extended) lifetime	3 (5) years
Geo-localisation accuracy	400 m

Table 5.1: SMOS mission requirements.

5.2 The Original forward model adopted in the Algorithm Theoretical Based Document (ATBD)

The values of albedo and optical depth are assigned by a preliminary modelling work based on the model, with suitable refinements and adaptation to specific cases. The output of this basic direct modelling work consists of look-up tables, relating sets of simulated emissivities (for the SMOS configuration) to SM, for the forest categories. Using allometric equations available in the literature for the different forest categories, geometrical and bio-physical inputs required by the model are related to LAI_{max}, i.e. the maximum yearly value of LAI. Then, a standard RMS minimization routine is used to find the equivalent values of the parameters (optical depth and albedo) to be assigned to a simple first order model, in order to behave mostly similar to the discrete multiple scattering model. This RMS minimization is made by considering, for each forest scenario, several sets of angles and SM values. This operation is named parameterisation. Details are described in section 3.5.

The two equivalent forest parameters (nadir optical depth and albedo) are indicated by τ_{FNAD} and ω_F, respectively.

A simple formula is used to compute the nadir equivalent optical depth of standing vegetation, such as:

$$\tau_{FNAD} = b'_F.LAI_{max} + b''_F \tag{5.1}$$

b'_F and b''_F values, specific of the forest categories. It is also assumed that ω_F does not depend on LAI_{max}.

The basic algorithm for forests are listed below:

- A simple τ_{FNAD} constant, without correcting factors depending on polarization and angle, may be used. This is a result of the variability in orientation of branches and leaves.

- τ_{FNAD} may be also considered as a "static" parameter. In fact, it is related to LAI_{max}, which may be assumed constant during the years of SMOS life. This is a result of the dominance of branch effects with respect to leaf effects at L band.

- ω_F may be considered constant (i.e. independent on angle, polarization and time).

Simulations have been done in order to include also the contributions of understory and litter. From the analysis of seasonal trends of LAI, given by ECOCLIMAP, it is estimated that 40% of LAI_{max} is contributed by understory.

Then the contributions to τ_{FNAD} may be computed as indicated below.

1) Contribution of crown (τ_1)

$\tau_1 = b'_{F1}.LAI_{max1}$, where $LAI_{max1} = 0.6LAI_{max}$ gives the contribution of leaves (without understory) to LAI_{max}, and is an indicator of branch biomass. The values of b'_{F1} are given below. We may assume $b''_{F1} = 0$

2) Contribution of litter (τ_2)

For litter contribution (τ_2), The overall contribution results to be nearly equal to the one due to crown. Then we assume: $\tau_2 = \tau_1$.

3) Contribution of understory (τ_3)

For understory, we may assume: $\tau_3 = b'_{LV}.LAI_{maxu}$, where $LAI_{maxu} = 0.4 * LAI_{max}$ gives the contribution of understory to LAI_{max}. For the coefficient b'_{LV} assume the same value $b'_{LV} = 0.06$ adopted for low vegetation.

4) Total τ_{FNAD}

$\tau_{FNAD} = \tau_1 + \tau_2 + \tau_3 = 2 * (b'_{Fl} * 0.6).LAI_{max} + 0.06 * 0.4.LAI_{max}$

Then: $b'_F = 1.2b'_{F1} + 0.024$

In particular, simulations lead to:

- $b'_F = 0.295, \omega_F = 0.095$ for deciduous broadleaf, evergreen broadleaf, woodland.

- $b'_F = 0.337, \omega_F = 0.080$ for needle leaf.

- $b'_F = 0.31, \omega_F = 0.087$ for mixed forest

  It may be assumed: b''_F =0 in all cases.

.

5.3 Reprocessed Forward Model of L-Band Emission From Broadleaf Forests

The objective of this section is to revise the forward model adopted to simulate the brightness temperature of broadleaf forests (deciduous or evergreen). The revised approach is basically similar to the original one, which was adopted in SMOS L2 ATBD (Section 5.2) [SO-TN-ESL-SM-GS-0001,SMOS level 2 processor Soil moisture].

In particular, the reprocessed model shows significant changes with respect to the original model.

- Since information about the subdivision between LAI due to both forest leaves and herbaceous components is already available in ECOCLIMAP, this information has been adopted in the reprocessed model. The forest leaf contribution will be named LAI_F , and its maximum yearly value will be named LAI_{Fmax}, while the herbaceous contribution will be named LAI_V. Both LAI_F and LAI_V variables are made available by ECOCLIMAP. This change generally leads to an increase of τ, but the percentage of leaf area attributed to arboreous leaves is lower than 60%, in some sparse forests.

- By using the formula proposed in [Bartelink et al, 1997] linking between the LAI and leaf dry biomass lead to a significant decrease of branch biomass and litter biomass, for a given LAI_{Fmax} . Hence, τ is reduced.

- An extensive analysis of data published in literature indicates an average diameter at breast height (dbh) of 20 cm to be more realistic than the value of 36 cm, adopted in the original model. This change should produce, by itself, an increase of τ.

- A more extensive analysis of data published in the literature was done also for litter. In particular, a new relationship between litter biomass and litter thickness has been adopted in [Sato et al 2004]. This change, in combination with the change of point 2, produces a strong reduction of litter contribution to optical thickness.

Overall, the new formulation does not produce strong variations of the albedo ω, but can lead to a significant decrease of the optical depth τ. At least for broadleaf forests, the revised formulation is less pessimistic than the original one with respect to forest attenuation.

5.3.1 Selection of an appropriate roughness parameter

In most of forest nodes, the H_R roughness parameter was set equal to 0.1. We have noted that this assumption leads to an initial estimate of forest emissivity which is lower than the measured value. This initial discrepancy, in combination with the overestimation of the optical depth, can lead to a not convergent retrieval procedure. We think that the initial H_R value should be increased. This is justified by various considerations.

First of all, there is a physical consideration. Previous studies, confirmed by the recent manuscript of Wigneron et al. [in Press], indicate that $H_R = 0.1$ corresponds to a smooth surface, with a height standard deviation of about 5 mm. In natural forests, the floor is expected to be more irregular, although it is difficult to have detailed measurements. Moreover, the emission due to soil and litter can be underestimated for other reasons, and this effect can be compensated by assuming a higher value of H_R . Value of $H_R = 0.3$, without dependence on soil moisture. According to [Wigneron et al.] and previous studies, this corresponds to a height std. of about 1.0 cm, which appears to be realistic. A similar value, or higher ones, are assumed in the physical model simulations and comparisons with airborne measurements. Further empirical refinements can be applied after long temporal series of SMOS measurements will be available.

5.3.2 Selection of the albedo

The simple model adopted in the ATBD attributes to the albedo ω a constant value, which depends only on the forest type. In our simulations, we obtained a decreasing trend of the albedo as a function of forest biomass, represented by LAI_{Fmax}. For broadleaf forests, a value of 0.095 was adopted in ATBD, obtained by averaging over a range of LAI_{Fmax} values between 1 and 6. However, tests with recent airborne measurements [Rahmoune et al, 2010] and first tests with the same SMOS data indicate that this value leads to a slight underestimation of the emissivity, due to two main reasons. First of all, the estimate of the albedo is more reliable for higher values of LAI_{Fmax}, and these values are lower than the average. Moreover, the physical model by itself tends to slightly underestimate the emissivity.

Therefore, avalue of ω=0.08 for broadleaf forests are adopted.

For moderate values of LAI_{Fmax}, the effects of this change are lower than the effects produced by the change of HR, but for very dense forests the increase in the initial value of brightness temperature can be appreciable (3-5 K).

5.4 SMOS results

For the time interval between March 1, 2010 and July 30, 2010, I have analyzed the SMOS signatures over different forest areas by using the Digital Product Ground Segment (DGPS) data in the L1C Scinece configuration. I have included in the analysis also auxiliary data, i.e. surface temperature and soil moisture initially estimated by ECMWF.

Three wide forest areas have been selected. Selected areas are flat, homogeneous, and free from water bodies or urbanization. These properties have been verified by ECOCLIMAP maps and Landsat maps. The forests are broadleaf, located in tropical regions, but with different values of Leaf Area Index. The properties are summarized in Table 5.2

Area	Longitude	Latitude	LAI_{Fmax}	LAI_V	τ ATBD	τ modified
Amazonia	[-65.5,-64.5]	[1,2]	6	0	1.75	1.7
Central Africa	[16.5,17]	[5.5,6]	1.75	1.75	1.06	0.7
Chaco	[-64.5,-64]	[-26,-25.5]	1.5	1.5	0.93	0.6

Table 5.2: Selected Broadleaf site forest

5.4.1 Multiangular comparisons

The angular trends of brightness temperature have been compared against the simulated ones in 4 cases.

- Forward model as in the original version of ATBD, and SMC estimated by ECMWF
- With modification of τ proposed as above.
- With modification of τ proposed as above, H_R=0.3 and $\omega = 0.08$
- With all previous modification and SMC obtained by fitting radiometric measurements.

5.4.1.1 Area 1 (Amazonia)

Amazonia is characterized by thick forest. The optical depth is very high both with the original ATBD and with the formulation described above.

The comparisons, for the orbit of April 18, are shown in Figure 5.1. Simulations and experimental data agree in indicating that the difference between vertical and horizontal

polarization is small and the trend as a function of angle is flat (see Figures 5.1a, 5.1b). The absolute values of TB are better reproduced with ω=0.08 and HR = 0.3 (Figure 5.1c). In this case the change is mostly related to the albedo, because the emission is dominated by the canopy. For the same reason, also the fitting of SMC produces small effects (Figure 5.1d).

5.4.1.2 Area 2 (Cental Africa)

Also in area 2 (Central Africa) the Leaf Area Index is low, and 50% is contributed by herbaceous vegetation. Therefore the optical depth is moderate. In this case, the SMC values predicted by ECMWF show a wide range of variations. I have selected the orbit of March 8 (Figure 5.2) . The initial values of brightness temperature do not differ so much from the measured ones, on average, but the polarization difference is underestimated. This discrepancy is eliminated by using the new formulation of τ. With $H_R = 0.3$ and ω=0.08 the agreement is improved. The fitted value of SMC is slightly lower than the initial one. In this case, the final fitting is influenced by the anomalous samples measured for angles lower than 20°.

5.4.2 Multi-temporale comparisons

I have considered multitemporal SMOS L1C signatures collected over broadleaf forests. The brightness temperatures have been computed by taking L1C data, applying the XY to HV transformation, and averaging between 37.5° and 47.5°. Temporal samples with a significant amount of RFI have been eliminated.

5.4.2.1 Area 1 (Amazonia)

Figure 5.3 shows, for the area in Amazonia, the comparison between measured and simulated trends of TB at vertical (top diagram) and horizontal (middle diagram) polarization. The diagram in the bottom shows the trend of SMC estimated by ECMWF. Here the forest is thick. Measured and simulated results agree in indicating that the difference between the two polarizations is low, and variations of TB are small. The soil moisture is high all the time, but this has scarce effects, because the emission is dominated by the thick crown.

Preliminary predictions of emissivity were formulated before the launch, in the framework of a study amed at investigating the performance of Amazon Rain forest for vicarious calibration. The study is summarized in Appendix A. with reference to figure 5.3, brightness

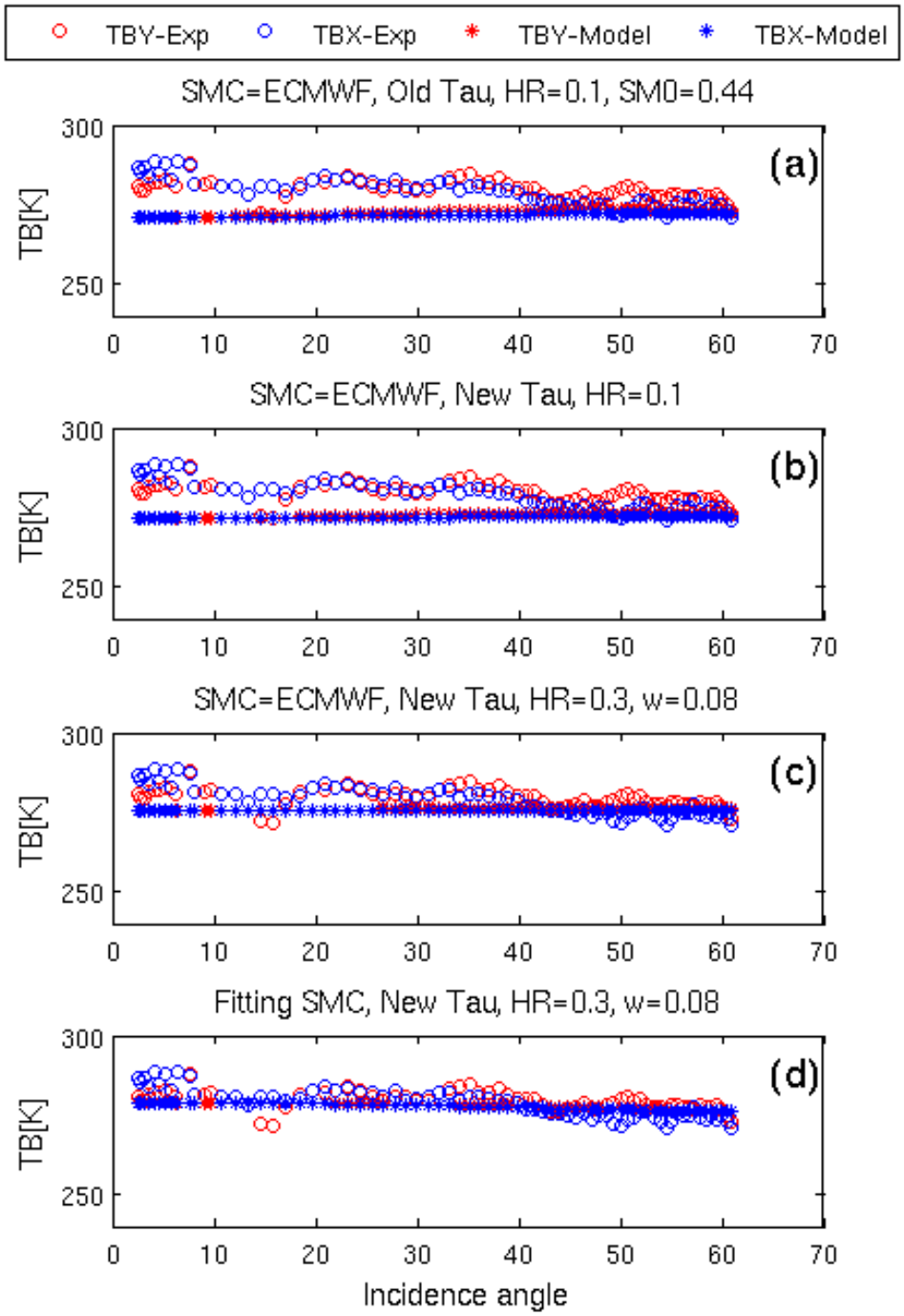

Figure 5.1: Comparison between simulations and measurements of brightness temperature vs. angle for area 1 (Amazonia). Orbit: April 18. a) Forward model as in the original ATBD, and SMC estimated by ECMWF. b) With modification of proposed in [1]. C) With modification of τ , HR=0.3 and =0.08 d) With all previous modification and SMC obtained by fitting radiometric measurements.

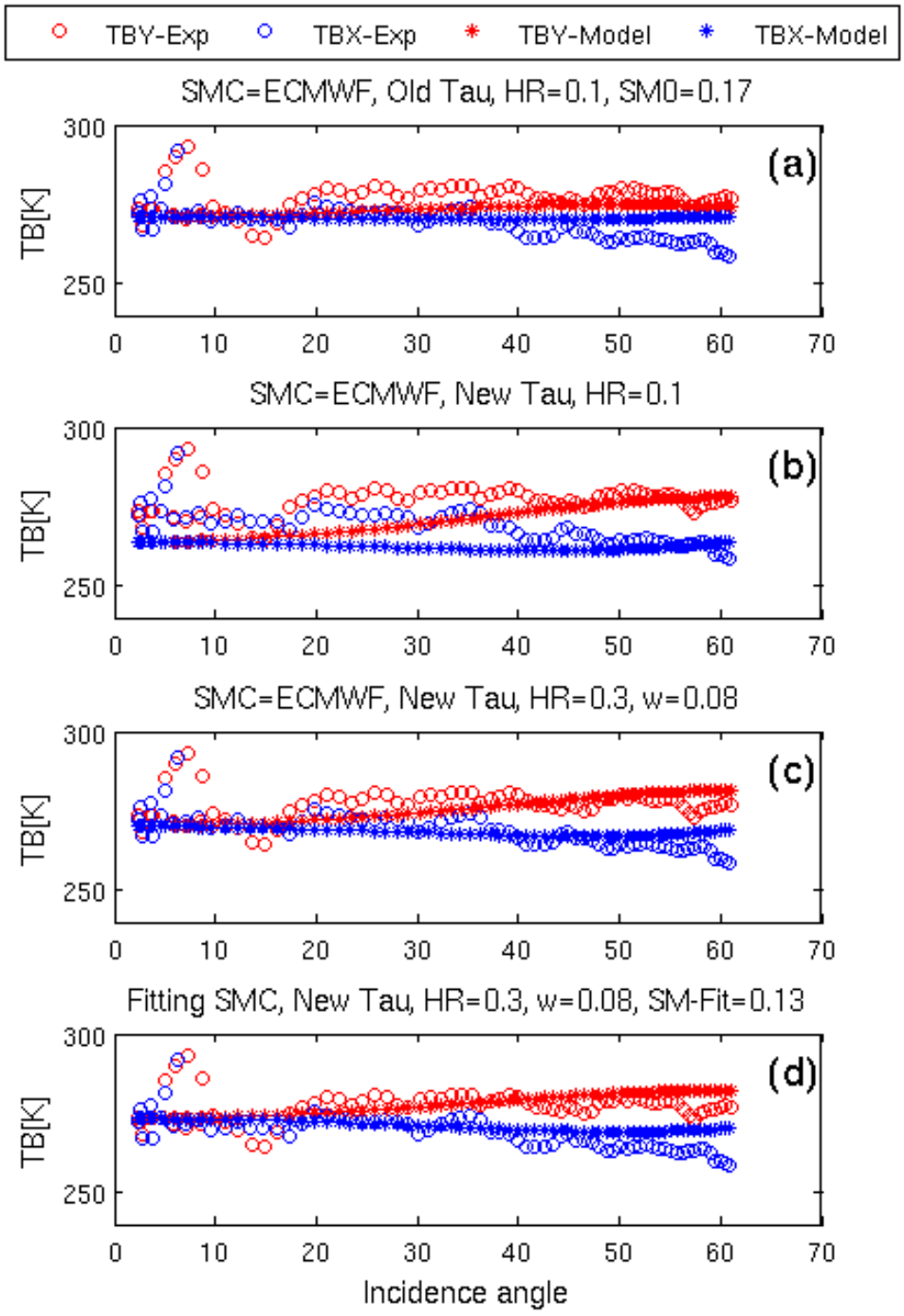

Figure 5.2: Comparison between simulations and measurements of brightness temperature vs. angle for area 3 (Central Africa). Orbit: March 8. a) Forward model as in the present ATBD, and SMC =0.17, estimated by ECMWF. b) With modification of τ proposed. C) With modification of τ proposed in [1], $H_R = 0.3$ and ω=0.08 d) With all previous modification and SMC =0.13, obtained by fitting radiometric measurements.

temperature values measured after DoY 160 correspond to an emissivity of ~ 0.93 at vertical polarization and ~ 0.92 at horizontal polarization, with very small temporal variations. In previous days there are some moderate variations of T_B which are unpredictable.

These small variations could be due to instrument calibration problems, which were stronger in the first months. Further date collection will clarify the problem. These are in agreement with predictions of Appendix A.

5.4.2.2 Area 2 (Central Africa)

Figure 5.4 shows the same trends for the forest of Central Africa. The optical thickness is lower than in the previous example. Here the TBs show appreciable variations, correlated with SMC. Simulated values agree with measured ones, with a slight underestimation of the variation observed on DoY 80.

5.4.2.3 Area 3 (Chaco)

In Grand Chaco, Argentina, the Leaf Area Index is low, and 50% of it is contributed by herbaceous vegetation. Therefore the optical depth is moderate.

Figure 5.5 shows the temporal trends of Brightness temperature (TB), emissivity, rainfall and ECMWF soil moisture vs. the Day of Year (DoY). Some reductions of TB and emissivity are well evident in the two upper plots. A small reduction on DoY 75 is detected at the beginning of an intense rain event. Other more evident reductions of TB and emissivity, recorded on DoYs 98, 127 and 138, are subsequent to rain events. For the last two events, there is a clear inverse correlation with ECMWF SM trends. On the contrary, the event of DoY 98 was not captured by ECMWF. The dynamic range of emissivity is about 0.06 units at vertical polarization and about 0.07 emissivity units at horizontal polarization.

The decreases of emissivity recorded in Figure 5.5 are more intense at horizontal polarization than at vertical polarization. In order to evaluate this property more clearly, in Figure 5.6 we represent the trends of both the emissivity and the Polarization Ratio. It is noted that the events producing lower values of emissivity produce also higher values of Polarization Ratio. Since this feature is typical of soil effects, it confirms that the reductions of emissivity are associated to rainfall events and consequent increases of soil moisture.

As a further investigation, the Polarization Ratio computed using SMOS signatures has been compared against the one computed by using AMSR-E C band data collected in the same interval of time. Results are shown in Figure 5.8. Although the signatures were obtained

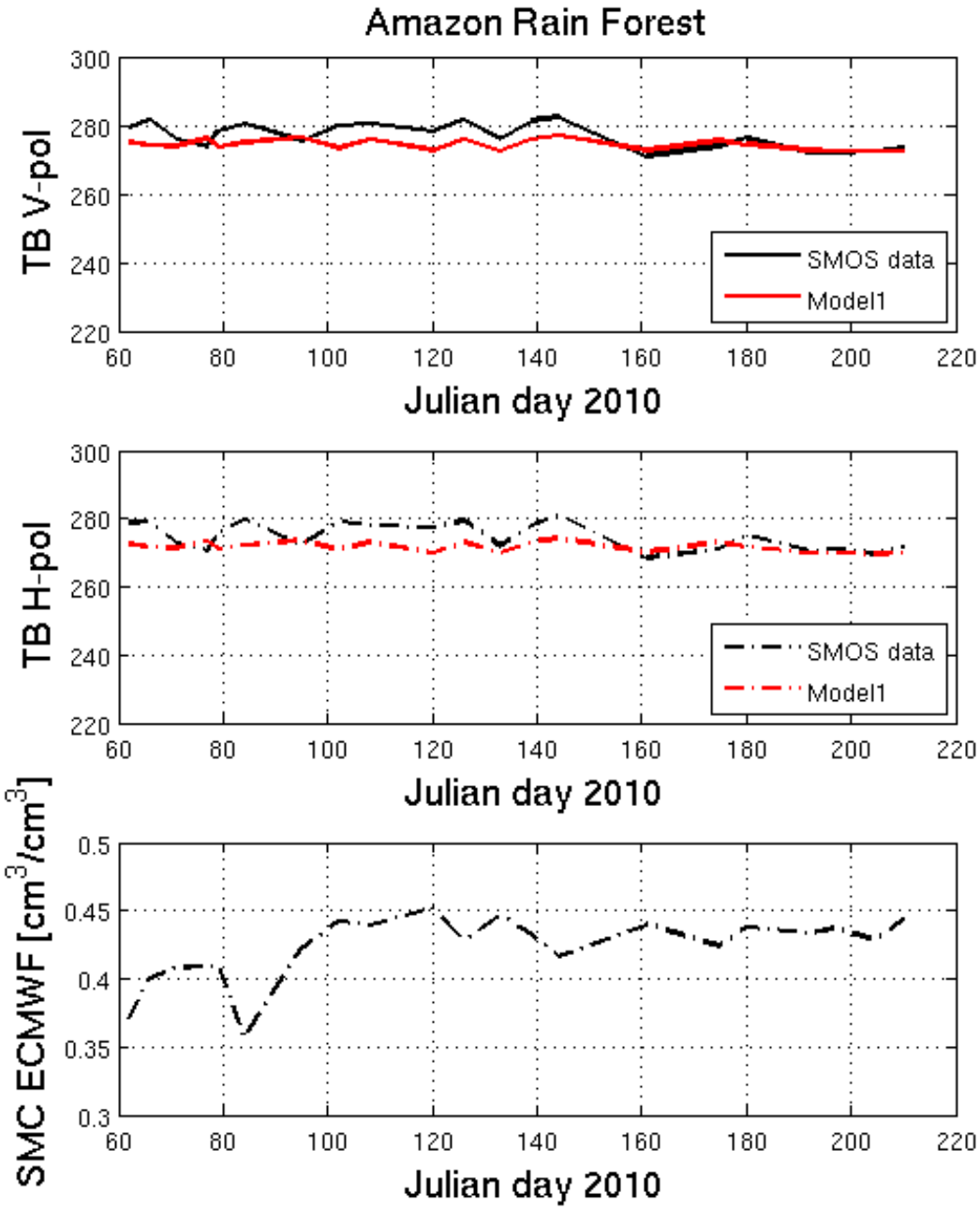

Figure 5.3: comparison between measured and simulated trends of TB at vertical (top diagram) and horizontal (middle diagram) polarization. The diagram in the bottom shows the trend of SMC estimated by ECMWF.

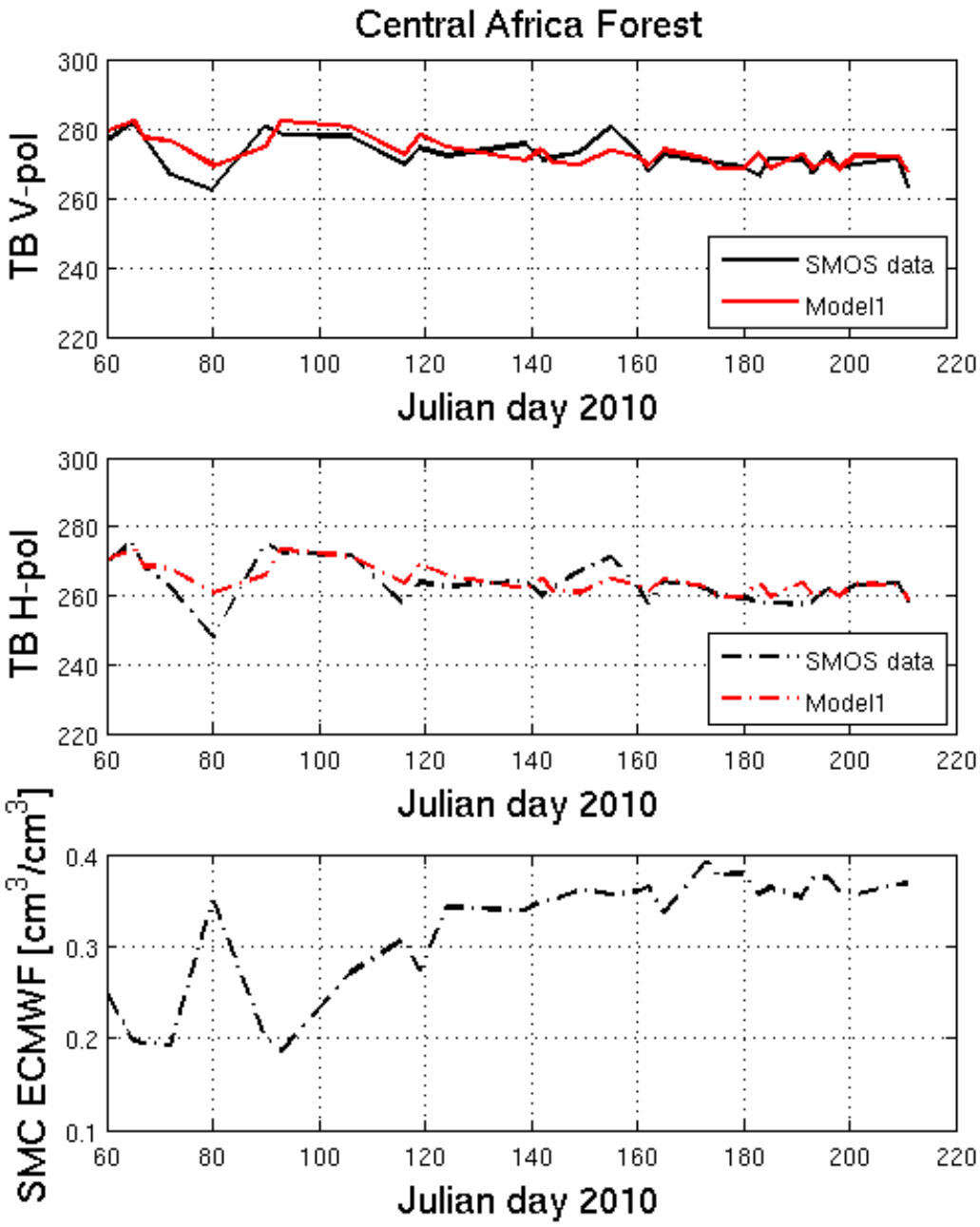

Figure 5.4: comparison between measured and simulated trends of TB at vertical (top diagram) and horizontal (middle diagram) polarization. The diagram in the bottom shows the trend of SMC estimated by ECMWF.

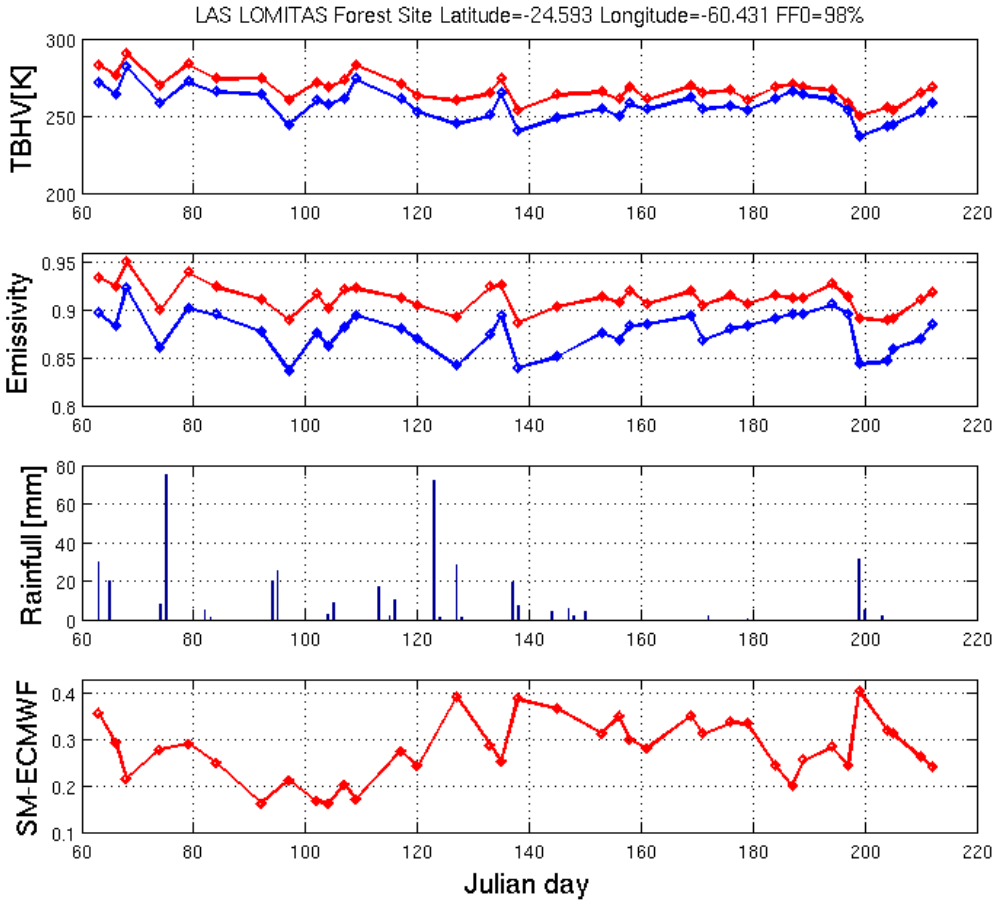

Figure 5.5: Temporal trends. From top to bottom: Brightness temperature (K) at vertical (continuous line) and horizontal (dash dotted line) polarization; emissivity at vertical (continuous line) and horizontal (dash dotted line) polarization; rainfall (mm), Soil Moisture by ECMWF

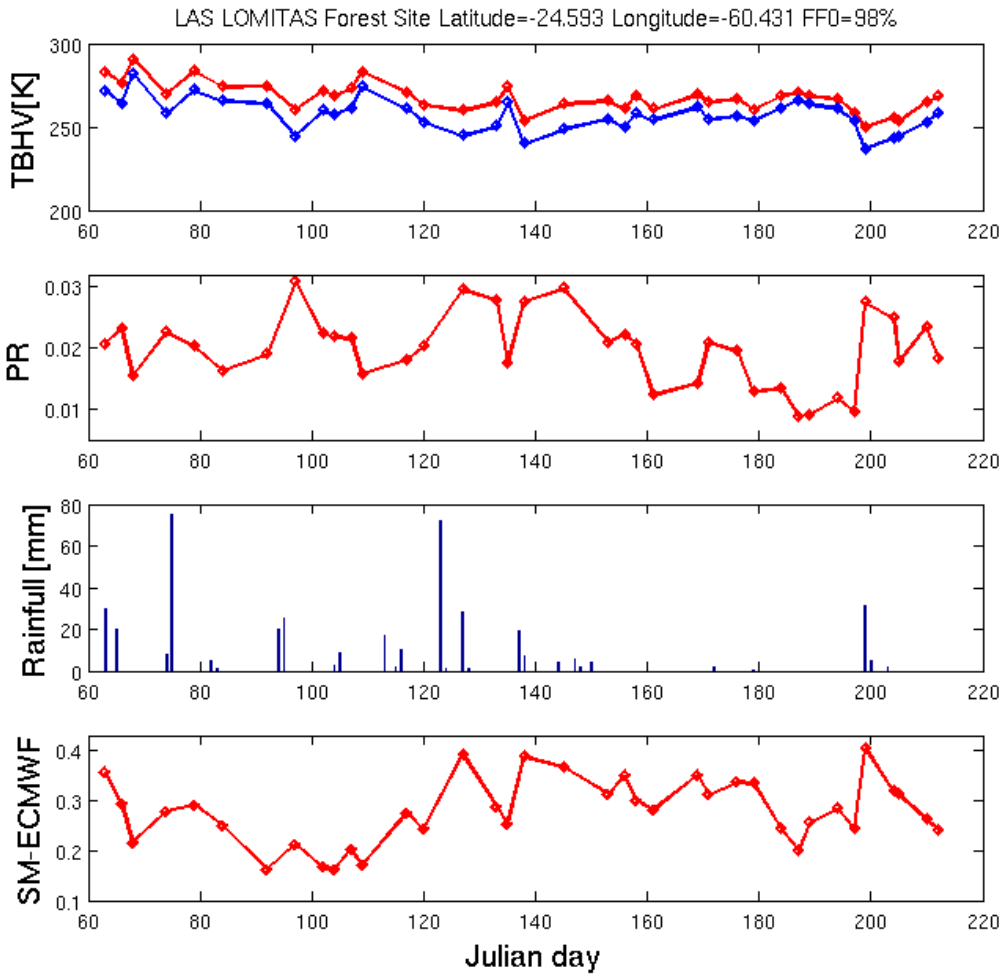

Figure 5.6: Temporal trends. From top to bottom: emissivity at vertical (continuous line) and horizontal (dash dotted line) polarization; polarization ratio; rainfall (mm), Soil Moisture by ECMWF

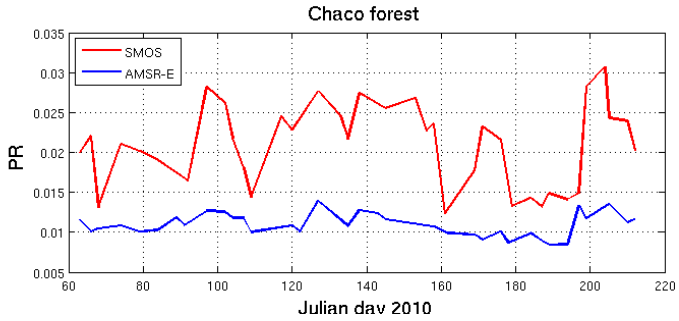

Figure 5.7: Temporal trends of Polarization Ratio collected by SMOS (red line) and AMSR-E at C band (blue line).

by independent instruments, at different angles and at different times of the day, there is a clear temporal correspondence between the two trends. This result again confirms that the variations of emissivity (and Polarization Ratio) are related to physical properties of the observed surface, and in particular to soil moisture. As expected, the dynamic range of L band time series is much better than the one attainable using C band.

Figure 5.8 shows comparisons between the brighness temperature trend simulated by the simple model and the SMOS data in Las Lomitas area. The model reproduces well both the absolute values and the variations, at both polarizations.

5.5 Concluding remaks

Six months of SMOS signatures collected over a dry and wet forest have been analyzed. Marked differences between moderate and thick forest have been observed. In particular, the chaco dry forest shows evident temporal variations of both emissivity and Polarization Ratio. The latter shows also a higher average value. The dynamic range of emissivity variations is 0.06-0.07 units (∼20 K). Emissivity reductions show a general correspondence with rainfall events and ECWF variations. Overall, these results are promising, indicating that SMOS has the potential to retrieve soil moisture under broadleaf forests with moderate biomass.

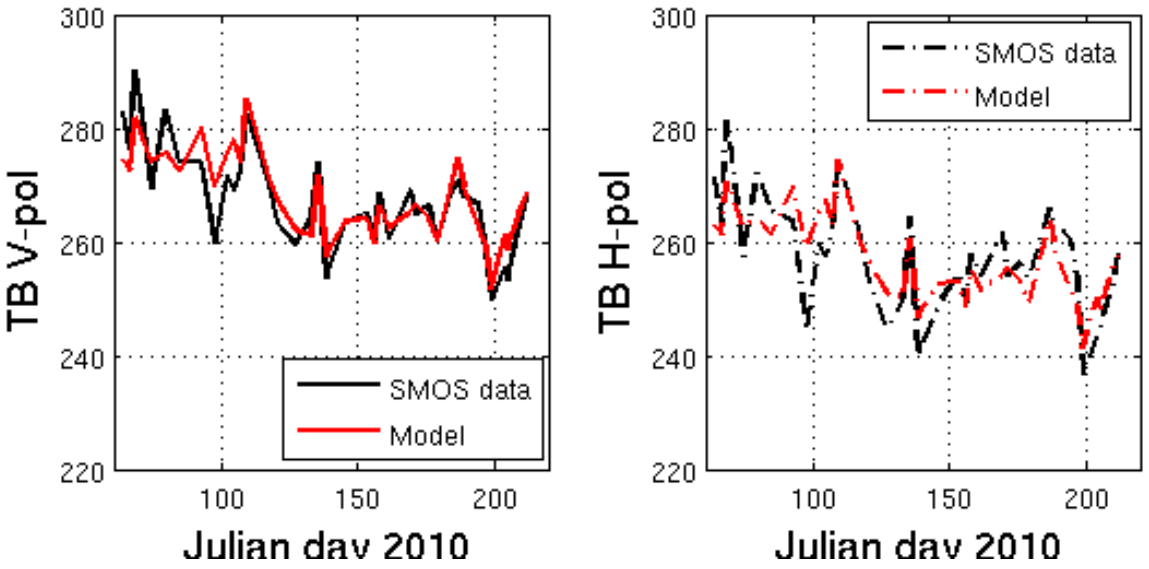

Figure 5.8: Comparison between SMOS measured and simulated trends of TB. Left: V polarization. Right: H polarization.

6

Potential of GNSS for biomass retrieval

6.1 Introduction

GNSS-Reflectometry is gaining increasing interest in the remote sensing community, due to the bistatic nature of the microwave scattering measurements (Jin and Komjathy, 2010). This technique exploits the L-band Global Navigation Satellite System (GNSS) signal as an opportunity source, with the consequent advantages of a limited cost and a potential high time resolution when performed from a spaceborne platform (Ruffini, 2006). Most of GNSS-R activities, both theoretical and experimental (Zavorotny and Voronovich, 2000a; Hajj and Zuffada, 2003; Martin-Neira et al., 2001; Gleason et al., 2005) concern oceans, as the high conductivity maximizes the reflected signal amplitude. Although most works considered the altimetric application, aimed at estimating the delay between direct and reflected signals, also the scatterometric mode is gaining interest. The latter measures the power coming from the sea surface, with the objective of estimating the reflection properties of the observed area which, on their side, are related to the sea state and wind speed over the ocean.Recently, the scatterometric mode has been proposed for land applications also, i.e., soil moisture monitoring (Masters et al., 2004) since, according to the well established Fresnel formulas, the reflection coefficient of a flat surface depends on its permittivity which, in the case of land, is dependent on its moisture content. Semi-empirical permittivity models indicate L-band to be well sensitive to this parameter, so that an appreciable sensitivity of GNSS-R to soil moisture is expected. In the last decade some experimental campaigns were carried out to

demonstrate that GNSS-R power waveforms can be detected over land, and their parameters are correlated to soil moisture content (Zavorotny et al., 2003; Masters et al., 2004; Gleason, 2006). Most of the pioneering study were devoted to a qualitative interpretation of the land waveforms, while most recent works proposed inversion algorithms relating power value of the waveforms to the Fresnel reflectivity (Katzberg et al., 2006; Egido et al., 2008). The sensititvity to soil moisture of the GPS reflected signal was proved also by means of a different approach: the Interferometric Pattern Technique (Rodriguez-Alvarez et al., 2009), which is based on the coherent addition of the direct and reflected fields. A theoretical study was performed by Zavorotny and Voronovich (2000b) who extended a previous model, based on the Geometrical Optics approximation and concerning GPS scatterometry over ocean, to the case of a bare soil with rough surface. The work in Pierdicca et al. (2008) also analyses the sensitivity to soil moisture of bare soil bistatic scattering, showing that at L-band the specular configuration exhibits a high sensitivity. The presence of vegetation can make the soil moisture retrieval a difficult task, since it attenuates and scatters the GNSS signal before it impinges on the ground and after it is reflected to the receiver (Katzberg et al., 2006). On the other hand, this may suggest another application of GNSS scatterometry, i.e. vegetation monitoring. It is well known that the biomass dependency of the radar backscatter varies as a function of radar wavelength and polarization, though reaching saturation after a certain biomass level. In Ferrazzoli et al. (2000) model simulations were carried out at L- and C-band with the aim of assessing the relevant features and the potential of the bistatic technique, and to investigate the possibility to overcome the limitations of monostatic radar in monitoring the crop biomass. Although the work was not strictly related to the use of GNSS-R, it considered specular scattering, so that its results at L-band may be taken as a first example of the potentiality of this technique. The theoretical study, carried out by means of a discrete Radiative Transfer model, showed that the biomass range over which an appreciable measurement dynamics is maintained can be widened by the specular bistatic configuration (Ferrazzoli et al., 2000). In particular, it was shown that the co-polar linear responses of a sunflower crop exhibits a decreasing trend with increasing biomass, since scattering in the specular direction is dominated by the soil coherent component, while all incoherent contributions are several dBs lower than total specular scattering. In this section, an extention of the previous study on specular scattering, focusing on GNSS-R applications to biomass monitoring of forests. The latter cover a very important role within the global monitoring objectives of remote sensing, such as carbon modelling, greenhouse gas emission

inventories and deforestation control. Collection of GNSS signal reflections over land may represent a valuable tool to monitor the vegetation biomass, complementing the already well assessed capability of GNSS-R over the sea surface. The discrete electromagnetic model which has been used to carry out this study will be recalled, and the equations adopted to estimate the variables required by the model are shown. Previous validations of the model are summarized. Also, a specific forest site for which radar measurements were made available by literature is considered (Imhoff, 1995) and a specific validation in the monostatic configuration will be carried out. The specular scattering coefficient of the same forest site is then simulated at VV and HH polarizations. In order to take into account the polarization properties of the GPS signal, simulation of the circular polarized scattering coefficient using a simplified version of the model are considered. Finally, parametric simulations are carried out using the typical GNSS parameters, in order to estimate the potentialities of GNSS-Reflectometry.

6.2 Model adopted

The model developed at Tor Vergata University, which has been used in this study, is a discrete model, a detailed description can be found in chapter 3, section 3.2.

Thus, the Tor Vergata model is intrinsically bistatic: for this reason a passive version was directly generated by applying the energy conservation law. This passive model is able to simulate microwave radiometric measurements of vegetation (Ferrazzoli and Guerriero,1996), while the first bistatic simulations are shown in Ferrazzoli et al. (2000) in the case of crops. It is well known that, due to the low power flux density at the earth surface, the reflected GNSS signal is significantly high in the specular direction only, so that the simulations presented here will refer to this direction. Specifically, the specular scattering coefficient of the forest canopy is modelled by:

$$\sigma^0_{pq}(\theta_i, \theta_s = \theta_i, \phi_s - \phi_i = 0) = \sigma^{0_{coh}}_{pq}(\theta_i, \theta_i, 0) + \sigma^{0inc}_{pq}(\theta_i, \theta_i, 0) \tag{6.1}$$

where θ_i and ϕ_i describe the zenith and azimuth direction of, respectively, the incident and scattered electromagnetic fields; p and q stand for polarizations of the scattered and incident electromagnetic fields. $\sigma^{0_{coh}}_{pq}$ is the coherent scattering coefficient of the soil attenuated by the above lying vegetation canopy. This coherent component is computed following the theory developed in Fung and Eom 1983 which correctly takes into consideration the spherical shape of the wave front impinging on the surface when produced by a real antenna. Note that the

coherent scattering coefficient of the soil depends not only on the surface parameters, but also on the receiving and transmitting antenna parameters. σ_{pq}^{0inc} is the incoherent scattering coefficient of the whole soil-vegetation canopy: it includes volume scattering from leaves and branches, double bounce effects due to soil and trunk interactions, multiple interactions between vegetation elements and between vegetation and the soil, incoherent scattering from the soil attenuated by the overlying vegetation canopy. The latter contribution is simulated by means of the Integral Equation Method (Fung, 1994), which was developed to fill the gap in the applicability range of the Kirchoff and Small Perturbation approaches. Although it contains some approximations which have been improved by subsequent versions (Advanced IEM, IEM with Multiple scattering), the original bistatic version is considered accurate in many practical cases, especially at L-band and for typical roughness parameters of soil (Macelloni et al., 2000; Chen et al., 2003). Furthermore, in section 3.3 it will be shown that scattering in the specular direction is strongly influenced by soil coherent scattering, so that eventual inaccuracies of the IEM predictions can be taken as negligible in this direction.

6.2.1 The Forest Parameters

Using allometric equations and empirical formulas derived by literature (Jenkins, 2003; Cannell, 1983), the geometrical and physical variables required by the electromagnetic model can be computed, according to the procedure indicated in detail by Della Vecchia et al. (2010). In the following section, backscattering measurements at L-band over a forest site in Hawaii (Imhoff, 1995) are compared with model simulations and, afterwards, simulations of the specular scattering coefficient of this same forests are carried out in section 6.4.3 The Hawaii site is an evergreen broadleaf forest (Metrosideros polimorpha) with varieties appearing as small shrubs and tall trees (Imhoff, 1995). In this study, dbh measurements in a range within 2 and 21 cm are reported for a biomass range between 4 and 300 t/ha: these values were used as a guideline to hypothesize a linear increase of dbh_{mean} [cm] with forest biomass DB0 [t/ha]. Since no further details were given about the relationship between these variable, a simple linear correlation was supposed in agreement with measurements collected over other forest sites (LeToan et al., 1992). Model simulations were performed using a dbh distribution of Gaussian type, with dbh_{mean}=(0.036 *DB0) + 6.3 and standard deviation σ_{dbh}=dbh_{mean}/3. The dbh range defined previously was calculated fixing dbh_{min}=dbh_{mean}-3σ_{dbh} (setting a lower limit dbh_{min}=2 cm) and dbh_{max}=dbh_{mean}+3σ_{dbh} Also for LAI a linear increase with

biomass was supposed, i.e., LAI=DB0/50. The tree density [#/ha] was calculated by means of:

$$N_T = 10^3 (a(\frac{DB0}{b})^{c^-1} exp(-(\frac{DB0}{b})^c))$$

a=14.3

b=232.42

c=1.49 (6.2)

which was derived performing a best fitting of the densities reported at the bottom of fig. 6.1 in Imhoff (1995). Equation (6.2) is reproduced in fig. 6.1. All necessary forest parameters were then derived according to the procedure described in Della Vecchia et al. (2010).

6.3 Model Simulations over a Specific Site

6.3.1 Previous comparisons of the model with experimental data

The Tor Vergata model for forests was originally developed to study the sensitivity of radar backscattering to biomass and tree geometrical properties. In Ferrazzoli and Guerriero (1995), the monostatic simulations of the Tor Vergata model was compared against backscattering coefficients of the Flevoland site (The Netherlands) collected during the MAESTRO-1 campaign in 1991. L-band data were acquired over five deciduous forests with different biomasses and were reproduced by the model with a slight overestimation. Applying the energy conservation and reciprocity principles, it was demonstrated (Peake, 1959) that emissivity is related to the integral of the bistatic scattering coefficient carried over all scattering directions in the upper half space Ω_s:

$$e_p(\theta_i) = 1 - \frac{1}{4\pi \cos\theta_i} \int_{\Omega_s} (\sigma^0_{pp}(\theta_i, \theta_s, \phi_s)) + \sigma^0_{pq}(\theta_i, \theta_s, \phi_s)) d\Omega_s \tag{6.3}$$

As it was mentioned in the previous section, the intrinsic bistatic nature of the Tor Vergata model made it possible to develop a passive version which is able to simulate the emissivity of a forest environment (Ferrazzoli and Guerriero, 1996) on the basis of the previous integral equation. The emissivity simulations were validated against multi-temporal data collected during the ground based Bray experiments (Della Vecchia et al., 2007) carried out over a single site in Les Landes forests (France). This study have demonstrated the sensitivity of forest emission at L-band to Soil Moisture and the important effect of litter. In section

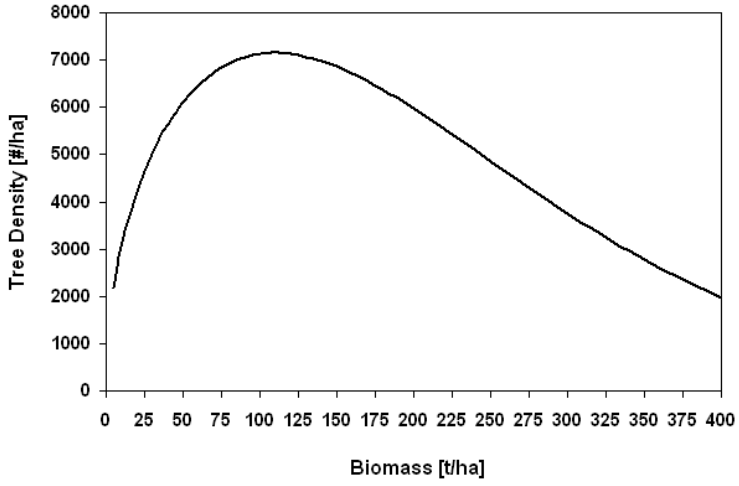

Figure 6.1: Tree density of the Hawaii forest site used to perform backscattering and specular simulations

3.6.1, the comparison of model outputs with airborne measurements carried out in Tuscany (Italy) over forests of different species was done, showing that emissivity is reproduced with a significant accuracy (in the range 2-3 K) and it allowed to single out the effects of Soil Moisture, forest biomass and trunk diameter (Della Vecchia et al., 2010).

Validation of the bistatic scattering simulations has not been possible, up to now, due to the lack of experimental data. However, the comparisons of both backscattering and emissivity with experimental data allow us to rely on the global performance of the bistatic model, since both scattering in a single direction, i.e. the backward direction, and the integral of scattering in the whole upper hemisphere, are reproduced with a satisfactory accuracy. In particular, the emissivity at L-band is strongly affected by coherent scattering in the specular direction which, as it will be shown in section 6.4.3, is the scattering component mainly affecting the GNSS-R measurements.

6.3.2 Backscattering simulation test

In the past, several campaigns were carried out with the NASA/JPL AIRSAR in order to study the correlations between radar backscatter and forest parameters. They were accompanied by ground measurements like those performed at the Duke forest site in North Carolina (USA) (Kasischke et al, 1994), Les Landes in France (LeToan et al., 1992) and Hawaii (Imhoff,

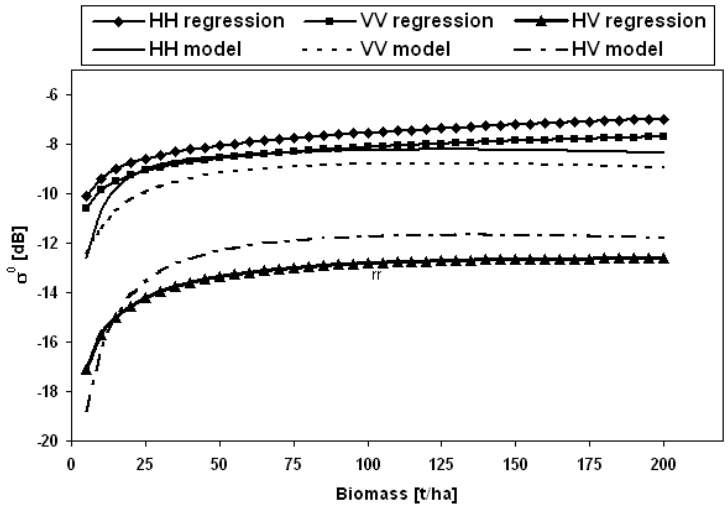

Figure 6.2: Comparison between model results and regression curves of the AIRSAR L-band measurements over the broadleaf evergreen forests in Hawaii

1995). In this chapter, backscattering measurements at L-band over the latter site are compared with simulations performed with the Tor Vergata model; to this aim the polynomial regression curves reported in Imhoff (1995) was used to reproduce the experimental trend of the three linearly polarized backscattering coefficients as a function of the forest biomass. The SAR observation angle ranged between 40° and 50°, and in model simulations it has been fixed to 45°.

In the absence of information about the soil parameters, typical average values of soil moisture and roughness of vegetated soils were assumed: the Soil Moisture Content (SMC) was fixed to 15%, the soil height standard deviation σ_z to 1.5 cm, and its correlation length to 5 cm. On the other hand, I verified that, at 45° incidence angle, changing their values in the ranges $10 \leq \text{SMC} \leq 20\%$ and $0.5 \leq \sigma_z \leq$ 2cm, the theoretical backscattering coefficient changes only for biomasses lower than 60 t/ha and mainly at vertical polarization: effects are limited by less than 0.5 dB for Soil Moisture and by 1.5 dB for soil roughness variations.

Figure 6.2 shows the simulated trends of σ^0 at the three linear polarizations and, reported for the sake of comparisons, also the polynomial regressions given by Imhoff (1995). In general, the increasing trend of σ^0 at the three polarizations is reproduced by the model and shows the saturation limit of the radar measurements which become almost insensitive to biomass beyond a certain limit.

At large values of biomass, the model overestimates the crosspolarized backscattering, while a slight underestimation is present in the co-polarized cases. The overall Root Mean Square (RMS) of the model error is 0.95 dB, indicating a generally good correspondence. The positive results of the backscattering test also allow us to be confident upon the assumptions made in Section 6.3.2 about the geometrical forest parameters of the Hawaii site.

6.3.3 Extension of simulations to the specular case

Up to now, no results of GNSS-R measurements over forests were published, so that it is not possible to assess the potentiality of this technique in biomass monitoring by means of experimental data. To reach this goal, the electromagnetic model developed at Tor Vergata is used. In the following, the specular bistatic coefficient of the same Hawaiian forest site is simulated and the relative contributions of the coherent and incoherent components in the specular direction is also highlighted.

Assuming that, if the observed area is flat (i.e., no topographic relief is present), contributions to specular reflection come mainly from the first Fresnel zone. The latter is traditionally defined as the locus of points, surrounding the specular reflection point, which reflect waves with phase shifts $\leq\pi$ with respect to the one reflected by the specular point itself. The waves reflected by different points on a surface interfere constructively if their paths differ by less than half a wavelength, otherwise they add with alternatively destructive and constructive interference. Since the destructive contributions of some points outside the first Fresnel zone are balanced by the constructive contributions of other points, it is usually assumed that the area responsible of reflection is only that of the first Fresnel zone (Beckmann and Spizzichino, 1963). In other words, a reflection that we think of as coming from a single point is actually being reflected from an ellipse with semiaxes a and b given by the following equation (when the transmitter height H_T is much larger than the receiver height H_R, and neglecting the earth curvature):

$$b = \frac{\sqrt{\lambda H_R \cos\theta_i}}{\cos\theta_i}, a = \frac{b}{\cos\theta_i} \tag{6.4}$$

These formulas are usually quoted in GNSS-R studies (Masters et al., 2004, Katzberg et al., 2006) and can be derived as in Caparrini (1998) from the expression of the geometrical locus of points with constant delays, given at p. 287 of Beckmann and Spizzichino (1963). The flat earth approximation can be considered valid for low incidence (high elevation) angles (Hajj and Zuffada, 2003).

Besides the coherent component coming from specular reflection by the first Fresnel zone, a diffuse component can be also present in the GNSS-R signal. It comes from the so-called glistening area, which is defined as the area for which the scattered power has dropped down by a factor 1/e (-4.3 dB) with respect to the specularly reflected one (Beckmann and Spizzichino, 1963). In the case of ocean surfaces, the diffuse contribution is described as the one produced by tilted facets on the surface and properly oriented to redirect the electromagnetic wave towards the receiver. Indeed, a slope probability function is usually introduced to model this contribution (see the Kirchhoff approximation) which describes scattering caused by roughness of the surface at scales comparable or larger than the incoming wavelength. Under these conditions, the coherent component is largely overpassed by the incoherent one and coherent scattering is consequently neglected. The roughness scales typical of land surfaces are well below the GNSS wavelength so that, unless topographic effects are present, the diffuse component does not arise from properly oriented slopes, and incoherent scattering is theoretically described by the Small Perturbation Model and the Integral Equation Method. As a consequence, while ocean surfaces own a glistening area that may extend over several delays with respect to the specular one, land surfaces do not own a glistening area since, as it will be shown by the following simulations, diffuse scattering from bare and vegetated soils is usually much lower than the coherent component.

In fig.6.3 the linear co-polarized response in the specular direction is represented as a function of the standing forest biomass, for an incidence angle of 20°: the steep decreasing trend of the specular scattering coefficient is due to the strong soil reflection, which suffers from an increasing attenuation due to the increasing forest biomass. Note that, in fig. 6.3, the total scattering coefficient, i.e., including both coherent and incoherent contributions, is superimposed on the curve that reproduces soil coherent scattering coefficient. This is a consequence of the fact that the latter keeps values larger than 10 dB, which are significantly higher than any incoherent contribution, i.e., coming from both vegetation volume and underlying ground. In particular, incoherent scattering from soil can be always considered negligible, while volume scattering may become a non negligigle contribution when vegetation biomass is large.

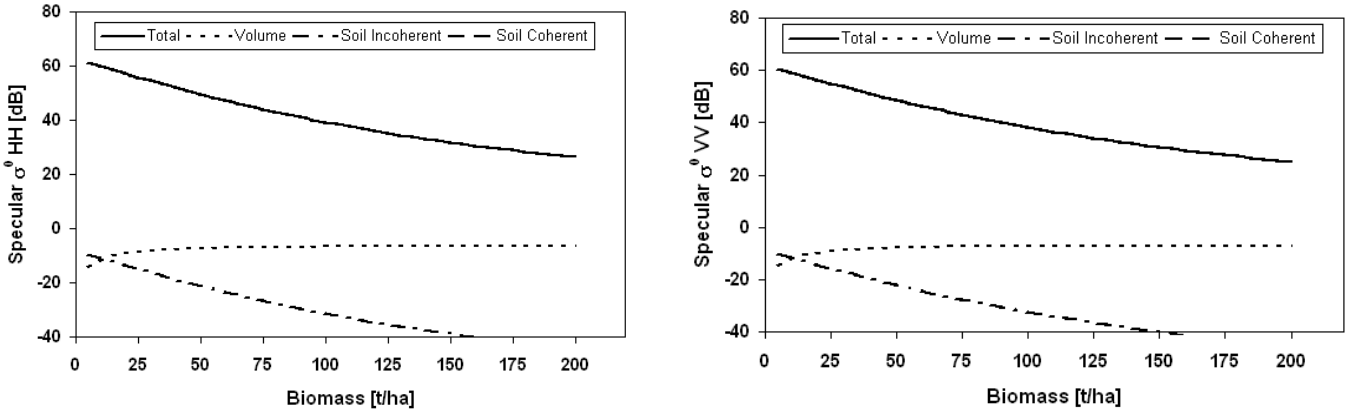

Figure 6.3: Simulated specular scattering coefficient of the first Fresnel zone for the broadleaf evergreen forests in Hawaii. Incidence and observation angle i=20°, HH (left) and VV (right) polarizations

6.4 Bistatic System with a GNSS Receiver

6.4.1 Single scattering approximation

In order to simulate the circularly polarized signal transmitted by a GNSS satellite, the Matrix Doubling procedure of the Tor Vergata model calls for an extension to a fully polarimetric version (Bracaglia et al., 1995) which requires scattering and extinction matrices with dimensions 4 times bigger than in the linear polarization version. The requested computational effort is therefore heavily increased and it is justified only if multiple scattering processes contribute significantly to the overall scattering. This is not the case for the GNSS-R configuration, so that the Tor Vergata model can be applied in a simplified single scattering form, wheareas allowing introduction of circular polarizations.

Let us consider a linearly q-polarized field E_q^i that is impinging upon a dielectric scatterer from a direction identified with angles θ_i and ϕ_i. The particle scatters in the direction identified with angles θ_s and ϕ_s a p-polarized field E_p^s which behaves as a spherical wave and, at a distance R from the scatterer, is expressed by:

$$E_p^s(\theta_s, \phi_s) = \frac{e^{ikR}}{R} f_{pq}(\theta_i, \phi_i, \theta_s, \phi_s) E_q^i(\theta_i, \phi_i) \tag{6.5}$$

f_{pq} is called the scattering amplitude and it is related to the bistatic scattering cross

section σ_{pq} and the extinction cross section σ_{ep} of the scatterer by:

$$\sigma_{pq}(\theta_i, \phi_i; \theta_s, \phi_s) = 4\pi \mid f_{pq}(\theta_i, \phi_i; \theta_s, \phi_s) \mid^2, \sigma_{ep}(\theta_i, \phi_i) = \frac{4\pi}{k}\Im(f_{pp}(\theta_i, \phi_i; \pi - \theta_i, \phi_i))$$

(6.6)

where Γ stands for the imaginary part operator and k is the vavenumber.

Let us now consider the forest crown as a collection of scatterers of different shapes, sizes, orientations and densities. Neglecting multiple scattering, we introduce the normalized crown bistatic scattering cross section and thenormalized crown extinction cross section:

$$\sigma_{pq}^{crown}(\theta_i, \phi_i; \theta_s, \phi_s) = \sum_j N_j^{crown}\sigma_{jpq}(\theta_i, \phi_i; \theta_s, \phi_s), \tau_p^{crown}(\theta_i, \phi_i) = \sum_j N_j^{crown}\sigma_{ejp}^{crown}(\theta_i, \phi_i) \tag{6.7}$$

Both parameters are normalized to the underlying area, and the second one is also referred to as optical depth.N_j^{crown} is the density per unit area of the j-th scatterer type in the crown layer, i.e., disks, needles or cylinders (N_j^{crown} is the conventional density per unit volume multiplied by the crown height), and:

$$\sigma_{jpq}(\theta_i, \phi_i; \theta_s, \phi_s) = 4\pi|f_{jpq}^{crown}(\theta_i, \phi_i; \theta_s, \phi_s)|^2$$

(6.8)

$$\sigma_{ejp}^{crown}(\theta_i, \phi_i) = \frac{4\pi}{k}\Im(f_{jpp}^{crown}(\theta_i, \phi_i; \pi - \theta_i, \phi_i))$$

(6.9)

f_{jpq}^{crown} is the complex scattering amplitude of the $j - th$ scatterer type in the crown. Brackets stand for dimension and orientation averaging. The power density scattered at distance R by an illuminated area A of a forest crown with height h, is given by (Ulaby et al., 1982):

$$|E_p^s(\theta_s,\phi_s)|^2 = \frac{A}{4\pi R^2}|E_q^i(\theta_i,\phi_i)|^2 \int_0^h \sigma_{pq}^{crown}(\theta_i,\phi_i;\theta_s,\phi_s)|h.e^{\frac{-\tau_p^{crown}(\theta_i)}{(h\cos\theta_i)z}}.e^{\frac{-\tau_p^{crown}(\theta_s)}{(h\cos\theta_s)z}}|dz \tag{6.10}$$

From integration of the above equation the bistatic crown volume scattering coefficient can be derived and, specifying for the specular direction, it is

$$\sigma_{pq}^{volume}(\theta_i,\phi_i) = \frac{4\pi R^2|E_p^s(\theta_i,\phi_i)|^2}{A|E_q^i(\theta_i,\phi_i)|^2} = \frac{\sigma_{pq}^{crown}(\theta_i,\phi_i;\theta_i,\phi_i).\cos\theta_i}{\tau_p^{crown}(\theta_i)+\tau_q^{crown}(\theta_i)}.(1-e^{\frac{-\tau_q^{crown}(\theta_i)}{\cos\theta_i}}e^{\frac{-\tau_p^{crown}(\theta_i)}{\cos\theta_i}}) \tag{6.11}$$

By introducing a trunk layer below the crown which attenuates electromagnetic waves due to their large dimensions. Trunks produce mainly forward scattering, and for this reason direct upward scattering from trunks can be neglected. Following the considerations drawn at the end of the previous section, the specular scattering coefficient of the whole forest canopy can be formulated by the sum of two contributions:

$$\sigma_{pq}^{0sp}(\theta_i,\phi_i) = \frac{1}{L_p^{trunk}(\theta_i)}\frac{1}{L_p^{crown}(\theta_i)}\sigma_{cohpq}^{soil}(\theta_i,\phi_i;\theta_i,\phi_i)\frac{1}{L_q^{trunk}(\theta_i)}\frac{1}{L_q^{crown}(\theta_i)}+$$
$$(\sigma_{pq}^{crown}(\theta_i,\phi_i;\theta_i,\phi_i).\cos\theta_i)/(\tau_p^{crown}(\theta_i)+\tau_q^{crown}(\theta_i))(1-\tfrac{1}{L_p^{crown}(\theta_i)}\tfrac{1}{L_q^{crown}(\theta_i)}) \tag{6.12}$$

The first term represents coherent scattering in the specular direction, the second term represents incoherentvolume scattering. (From now on, the angular dependence will be understood, since the specular direction only is taken into account). In eq. 12) σ_{coh}^{soil} is the soil coherent scattering coefficient (simulated accordingly to the theory developed in Fung and Eom, 1983) which is attenuated two times by the vegetation, made up of a crown and a trunk layer: $\frac{1}{L^{crown}}$ and $\frac{1}{L^{trunk}}$ are the one way loss factors of, respectively, the crown and the trunks. They are related to the normalized extinction cross section by means of $L^{layer} = e^{\frac{-\tau^{layer}}{\cos\theta_i}}$, where layer is crown or trunk.

τ^{trunk} is computed by averaging the extinction (σ_{ej}) cross sections of the single scatterers inside the trunk layer, over all dimensions, by means of the following relationships:

$$\tau_p^{trunk} = \Sigma_j N_{Tj}\sigma_{ejp}^{trunk} \tag{6.13}$$

$$\sigma_{ejp}^{trunk} = \frac{4\pi}{k}\Gamma f_{jpp}^{trunk}(\theta_i,\phi_i;\pi-\theta_i,\phi_i) \tag{6.14}$$

f_{jpq}^{trunk} is the complex scattering amplitude of the j-th trunk at incident and scattering q and p polarizations. N_{Tj} is the density per unit area of trunks with the j-th dbh, within the distribution defined in section 6.3.2. (For the Hawaii site $N_T = jN_{Tj}$ with N_T defined in eq. 6.2).

For circularly polarized incident and scattered fields, the scattering cross sections are obtained from a suitable linear combination of the scattering amplitudes $f_{VV}f_{HH}f_{HV}f_{VH}$ (Ruck et al., 1970). The normalized circular extinction cross section τ_{eC} is obtained according to the following procedure. If an elliptically polarized wave is propagating through a vegetation layer, the loss factor can be expressed as in Lopes et al. (1991):

$$\frac{1}{L_p^{layer}} = c_v^2 exp(-\tau_v^{layer} sec\theta_i) + c_H^2 exp(-\tau_H^{layer} sec\theta_i) + 2c_V c_H \cos(\beta_H^{layer} - \beta_V^{layer}) exp(-0.5(\tau_V^{layer} + \tau_H^{layer}) sec\theta_i) \tag{6.15}$$

where layer is trunk or crown and:

$$\beta_p^{layer} = \frac{2\pi}{k} \Sigma_j N_j^{layer} \Re f_{jpp}^{layer}(\theta_i, \phi_i; \pi - \theta_i, \phi_i) \tag{6.16}$$

with p=H or V or Circular, and $\Re$ being the real part operator. For a V polarized wave c_v=1 and c_H=0; for an H polarized wave c_V=0 and c_H=1; for a Circularly polarized wave c_V=$\frac{1}{2}$ and c_H=$\frac{1}{2}$. Note that the loss factor is the same for a Left circularly polarized wave and a Right circularly polarized wave. Given an incident circularly polarized wave, the normalized circular extinction cross section τ_C can be derived by the inversion:

$$\tau_c^{layer} = \cos\theta_i . \ln(L_c^{layer}) \tag{6.17}$$

In order to consider the wave depolarization, which can also occur during propagation through the vegetation layer, the depolarization factor D (Lopes et al., 1991) has been introduced:

$$D_p^{layer} = \mid exp(-\frac{1}{2}\tau_v^{layer} sec\theta_i) - exp(-\frac{1}{2}\tau_H^{layer} sec\theta_i) \mid^2 C_V C_H \tag{6.18}$$

It is now possible to account for the wave impinging on the soil at, let us say, circular Right polarization which is composed of the incident Right polarized wave affected by vegetation attenuation (through the loss factor $\frac{1}{L}$), but also of the Left polarized incident wave depolarized while propagating through vegetation. Similarly, the power scattered by soil suffers from attenuation and depolarization before reaching the receiver. As a consequence, for circularly polarized waves, the first term in eq. (6.12) becomes (the subscripts R and L stand for Right and Left polarization):

$$\sigma_{RR}^{soil} = (\frac{1}{(L_C^{crown})^2 (L_c^{trunk})^2} + (D_c^{crown})^2 (D_c^{trunk})^2)) \sigma_{cohRR}^{soil} + 2 \frac{D_c^{crown}}{L_c^{crown}} \frac{D_c^{trunk}}{L_c^{trunk}} \sigma_{cohRL}^{soil}$$

$$\sigma_{RL}^{soil} = (\frac{1}{(L_C^{crown})^2 (L_c^{trunk})^2} + (D_c^{crown})^2 (D_c^{trunk})^2)) \sigma_{cohRL}^{soil} + 2 \frac{D_c^{crown}}{L_c^{crown}} \frac{D_c^{trunk}}{L_c^{trunk}} \sigma_{cohRR}^{soil} \tag{6.19}$$

where it is assumed that $\sigma_{RL} = \sigma_{LR}$ and $\sigma_{LL} = \sigma_{RR}$, due to the azimuthal symmetry of the vegetation canopy.

First of all, this simplified single scattering model has been tested comparing the simulations performed at linear polarizations in the specular directions against the simulations performed applying the general Tor Vergata model, described in Section 6.3, based on the Matrix Doubling algorithm. The latter allows to include multiple scattering contributions within the crown and also multiple interactions between the soil and the crown itself. The difference between the results obtained by the two methods is very low with respect to the dynamic range: the maximum difference occurs at the largest biomass values and it is equal to 1.2 dB at VV polarization and to 0.5 dB at HH polarization. This result is obtained because the specular scattering is contributed mainly by the attenuated coherent scattering from the soil and multiple scattering effects introduced by vegetation are negligible. On the other hand, we point out that the multiple scattering contributions could not have been neglected in the monostatic simulations, at least when the volume contribution is the most important one (Ferrazzoli and Guerriero, 1995).

6.4.2 Simulations of GNSS reflected power

As we mentioned earlier, the specular scattering coefficient due to the coherent scattering from the soil depends on the transmitter and receiver parameters (Fung and Eom, 1983), i.e., the

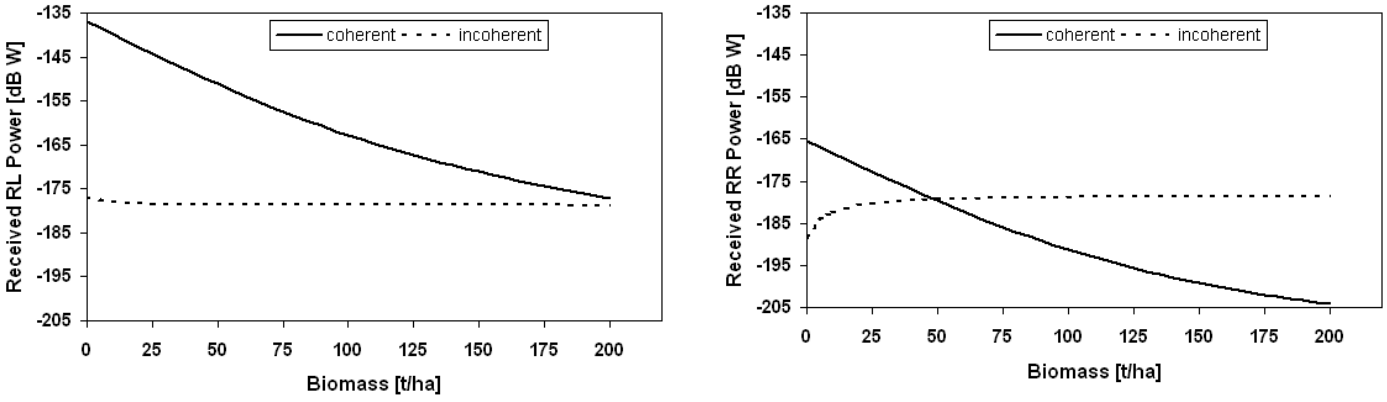

Figure 6.4: Received Power at circular polarizations vs. biomass. $\theta_i = 20$, $\sigma_z = 1.5cm$, $SMC = 15\%$, receiving antenna gain G=25 dB. Left: RL polarization; right: RR polarization

antenna beamwidths and their heights. Indeed, applying the scattering coefficient definition to a coherent process means to transfer the antenna effects into a parameter which should represent the object scattering properties only. In order to use a physical quantity which is more useful from the application point of view, in the following simulations we will make reference to the power which reaches the receiving antenna. To this end, the classical bistatic radar equation is used to compute the power measured by the receiver antenna: an Equivalent Isotropic Radiated Power (EIRP) by the GNSS transmitter equal to 27 dBW is assumed to be incident over the observed surface (Bao-Yen Tsui, 2005). Coherent power comes from an area equal to the first Fresnel zone and characterized by the coherent specular bistatic scattering coefficient calculated by means of the model described previously. In particular, for transmitter and receiver heights fixed, respectively, to H_T=20000 km and H_R=600 km, the region where coherent reflection takes place has an extension of about 0.35 km^2 at nadir. In order to evaluate incoherent power we applied the bistatic radar equation to the equi-delay ellipse surrounding the specular point and corresponding to $\frac{1}{2}$ chip delay of the $\frac{C}{A}$ code. For the above receiver and transmitter height, this is an area of about 500 km^2 at nadir. We then supposed that the bistatic scattering coefficient of this area was isotropic and equal to the specular one: this represents an upper bound since bistatic scattering is usually at its maximum in the specular direction.

In the following simulations, a receiving antenna gain equal to 25 dB was supposed (this is an arbitrary value that, however, affects the power simulation in dBW only by a constant

factor and does not change its sensitivity to biomass). Additional processing gains, such as coherent or incoherent integration, were understood: that is, the expected value of the received signal is considered, provided the proper noise and speckle mitigation approaches are carried out. The simulations of the co- and cross-circularly polarized powers at an angle θ_s=θ_i=20 are reported in Fig.6.4 as a function of biomass of the Hawaii deciduous forest. On the left of fig.6.4, simulations of the two components of the RL power are plotted. It can be observed that, unless vegetation is very dense, it is not possible to define a glistening area since the incoherent power (from both volume and soil) is well below -4.3 dB of the coherent power. Experimental data support this outcome: GNSS-R waveforms collected over land surfaces (Masters et al., 2004) did not show spreading to delays longer than the specular one, and measurements performed with the Interferometric Technique (Rodriguez-Alvarez et al., 2009) were based on the coherency of the specularly reflected signal.

From fig.6.4 we also observe that the coherent RR polarization power is about 30 dB lower than the RL one, since vertical and horizontal reflectivities have opposite phases whose combination tends to cancel coherent reflection by soil at RR polarization. As a consequence, the RR signal is prevalently dominated by incoherent scattering, quickly reaching a saturation values which is very low. Therefore, detection of RR polarization appear more critical, so that the following simulations will concern RL polarization only.

6.5 Sensitivity Study

In this section, the sensitivity of a GNSS reflected signal to forest biomass will be studied for various incidence angles, soil parameters and dbh distributions. The effects of incidence angle are reported in Figure 6.5 which shows that at the higher incidence angles the RL signal owns a large dynamic range, but it carries lower power which can result in a very low SNR. For this reason, low observation angles seem to be better suited to biomass monitoring, and we remark that for $\theta_i \sim 20$, the sensitivity of σ^0_{RL} although is lower than the one at higher angles, may reach an appreciable value of about 2 dB for an increase of $10 t ha^{-}1$. In order to appreciate the effects of soil parameters, Fig.6.6 reports the simulated power at $\sigma_i = 20$ for two different values of Soil Moisture Content and two different values of the height standard deviation. This plot confirms that the received power is stronger for lower biomass value and it shows that power decreases with decreasing soil moisture or with increasing roughness.

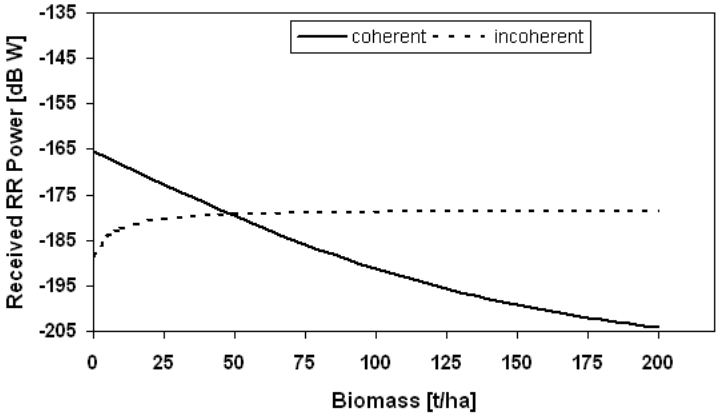

Figure 6.5: Received Power at RL polarization vs. the biomass of the Hawaii forest. The three curves correspond to three incidence angles (θ_i=0, 20 and 50°). σ_z=1.5 cm, SMC=15%, receiver antenna gain G=25 dB

However, the effects of all soil variables are low with respect to the dynamic range related to variations of forest biomass.

All previous simulations of GNSS-R measurements were performed assuming the Hawaii forest as a case study, i.e., using the same forest parameters used in Section 6.4.2 to compare the model results with the monostatic measurements reported in Imhoff (1995). In order to simulate different environmental conditions, in Fig.6.7 the effect of the forest dbh is studied. In particular, specular measurements were simulated concerning forests with a Gaussian dbh distribution but with different mean dbh. For the sake of simplicity, the trees were ideally supposed to be all of the same size, i.e., given a dbh_{mean} value, the standard deviation of dbh was taken to be equal to 1cm, and the biomass variation is obtained increasing the tree density. The simulations show that the sensitivity of the GNSS-R signal is dependent on the contextual forest parameters, i.e., dbh and density. In particular, for a given biomass, lower signal powers are received when the trees are very small and very numerous. The presence of larger and fewer trees (larger dbh_{mean} values) reduces attenuation and consequently the sensitivity to biomass, upon which it is strictly dependent. Nevertheless, the dynamic range of the RL polarized reflected power at low incidence angle remains larger than 10 dB, even in the worst case.

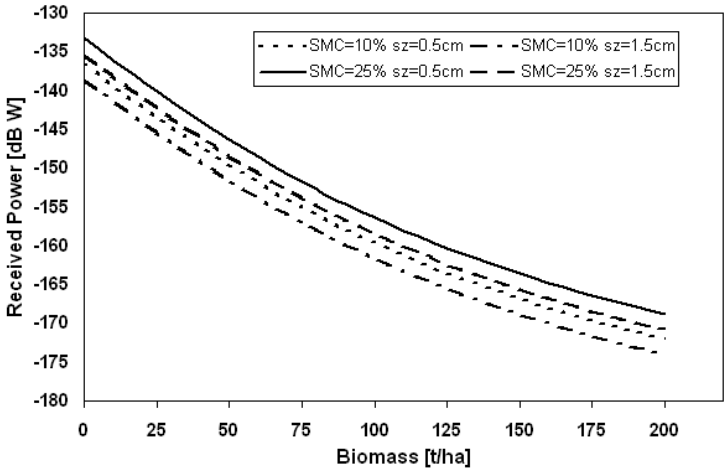

Figure 6.6: Received power at $\theta_i = 20$, RL polarization, vs. the biomass of the Hawaii forest. The curves correspond to different soil conditions as indicated in the legend

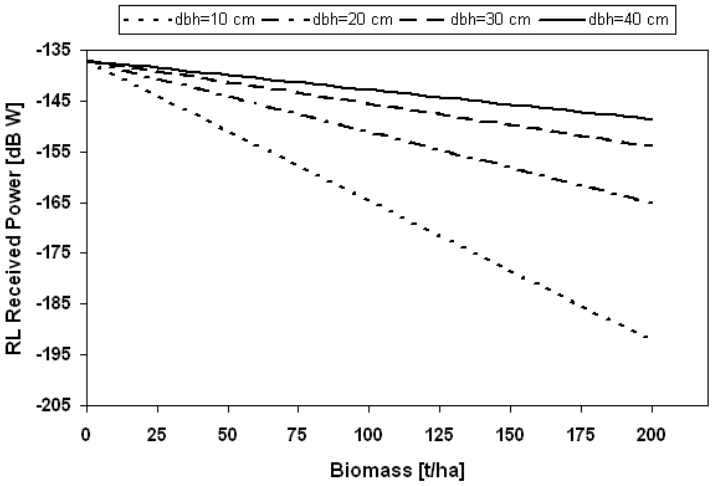

Figure 6.7: Received power at RL polarization vs. the biomass of forest with four different dbh_{mean}: 10, 20, 30, 40 cm, dbh standard deviation σ_{dbh}=1 cm. $\theta_i = 20$, σ_z=1.5 cm, SMC=15%

6.6 Conclusions

In this chapter, theoretical simulations of the specular scattering coefficient of forests were performed in order to evaluate the potential of the GNSS-R technique for biomass monitoring. A deciduous forest site in Hawaii, for which measurements were available in the literature, has been considered to test the monostatic simulations of the model and, then, to analyse the behaviour of the simulations in the specular direction. A simplified model able to take the GNSS circular polarization into account have been introduced and computations have shown that forests do not mask the RL coherent specular reflection from soil. This contribution turns out to be larger than incoherent scattering from the vegetation volume and the underlying soil, thus allowing to monitor forest biomass thanks to its attenuation effects. Depending on the observation angle and the forest density, the reflected power can be significantly high to be detected. In particular, specular measurements at low incidence angles and RL polarization are more suitable for forest applications, since they keep a significant sensitivity to biomass without reaching extremely low values of received power.

7

Summary & conclusions

Mapping and monitoring soil moisture and vegetation variables, such as biomass and Leaf Area Index (LAI), is important in the study of fundamental problems, such as global carbon cycle and climatic changes. From a physical point of view, the sensitivity of passive microwave measurements to soil and vegetation properties was proved by several theoretical and experimental investigations [Ulaby et al, 1986]. The main goal of this study was to obtain an improved understanding of L-band (f = 1.4 GHz, = 21 cm) forest emission, in view of (SMOS) soil moisture retrievals from heterogeneous pixels containing fractional forest cover.

Experiments using both ground based and airborne radiometers have provided an insight to the problem [Lang et al, 2001]-[Santi et al, 2001], but only a limited number of forests have been observed. Some experimental investigations, carried out over coniferous forests, or deciduous forests in cold climates, indicate that the effects of soil moisture variations on radiometric signatures are very low, even at L band [Guglielmetti et al, 2008], [Grant et al, 2007]. Other experiments in temperate climates indicate that a moderate sensitivity to variations of soil moisture exists, at least at L band [Santi et al, 2001], [Grant et al, 2010], [Rahmoune et al, 2010]. Since definitive conclusions have not yet been reached, it is useful to make further investigations, covering a variety of climatic conditions and forest environments.

To this end, L-band radiometric data were obtained from Airborne measurements in summer 2000 and winter 2002 in Tuscany (Italy) over various broadleaf forests, spanning a wide range of biomass, in June 2006 over dense forests in Finland made by the AMIRAS demonstrator. The analyses based on these experimental data were used to better understand forest emission and radiative transfer properties. Airborne L-band data were obtained during

the NAFE '05 campaign in South-East Australia in 2005. These data were used to investigate the sensitivity to the soil moisture variations under moderate forest cover.

7.1 Summary and Conclusions

As conclusions of this work, I started initialy with an introduction of the microwave modeling approaches used to monitor soil and vegetation properties, in particular for forestry applications by giving more information about the electromagnetic model developed at Tor University, with the recent refinements introducing the new aspects on litter and soil. Moreover, in the framework of SMOS project, a procedure has been developed to estimate the input dataset when only general information about forests is available. The model output have been compared against experimental data collected in various forest sites, the main conclusions can be drawn as:

- The reduction in sensitvity to soil moisture variations by crown attenuation depends not only on forest biomass but also on the average dimensions of forest elements (trunk and branches). For given bomass, higher values of attenuation are obtained in the presence of several trees with small trunk diameters. Further attenuation of soil emission is produced by litter and understory.

- For developed forests, the average trunk diameter plays a strong influence on the emissivity at L-band. This can be a problem in the application of retrieval algorithms based on simple models. On the other hand, it could give the opportunity to identify areas dominated by old large trees.

- It is confirmed that L-Band shows the best sensitivity to seasonal variations and forest biomass. However, the simultaneous availability of higher frequncies could be used as an alternative to infrared or surface temperature. This operational aspect can be the subject of future studies.

In a second step, we studied the effects of raistorm events in the Chaco forest as seen by the C Band channel of AMSR-E. The events were big (¿ 100 mm/day) and occurred after a dry period. We observed a significant change in PI after the rain event. Using ancillary data and considerations about the spatiotemporal characteristics of the observed signatures, we associated these changes in PI to a change in soil moisture. The results indicate that

there is some potential to monitor variations of SMC using AMSR-E signatures, at least in dry forests with moderate woody volume. Using the fisrt SMOS long term multitemporal signatures then after over the same forest site, we find a better sensitivity and the results are very promising, indicating that SMOS has the potential to retrieve soil moisture under forests with moderate biomass.

Finally and in order to evaluate the potential of the GNSS-R technique for biomass monitoring, theoretical simulations of the specular scattering coefficient of forests were performed. A deciduous forest site in Hawaii, for which measurements were available in the literature, has been considered to test the monostatic simulations of the model and, then, to analyse the behaviour of the simulations in the specular direction. A simplified model able to take the GNSS circular polarization into account have been introduced and computations have shown that forests do not mask the RL coherent specular reflection from soil. This contribution turns out to be larger than incoherent scattering from the vegetation volume and the underlying soil, thus allowing to monitor forest biomass thanks to its attenuation effects.

7.2 Future work

Validation of the inversion algorithm of SMOS soil moisture request (i) validation of the direct radiative transfert model on a variety of land covers and (ii) validation of the inversion algorithm to the SMOS scale.

Appendix A

Use of Amazon forest for SMOS Vicarious Calibration

A.1 Introduction

This Appendix reports some results of a study focused on the definition of an operational methodology to monitor the calibration of the innovative instrument "Microwave Image Radiometer using Aperture Synthesis (MIRAS)" by investigating the possibility to use natural targets on the Earth surface to obtain long term information on the MIRAS instrument calibration stability. The usage of natural targets to determine drifts in instrument measurements is commonly defined as "vicarious calibration" and its usefulness is demonstrated in previous studies.

In this study, a potential calibration area, such as Amazon forest is considered, and the temporal stability of its emission at L-band is investigated. The outcome of this study is to investigate the possibility of using it as a calibration site (Crapolicchio et al.2010).

A.1.1 Amazon forest

The Amazon rainforest is a wide uniform region characterized by very thick vegetation that attenuates TB variations due to soil moisture effects, even at the lower microwave frequencies. Previous studies over Amazon forest at L-band [Jackson et al., 2004], at C- band [Crapolicchio and Lecomte, 2003] and at higher frequencies [Brown and Ruf, 2005] indicate that the emissivity and the backscattering coefficient over this dense evergreen forest are almost constant in time and suggest that an extended domain in this region might be used as a calibration

site for SMOS. In order to give a first estimate of the temporal and spatial stability of the TB's over the Amazon rainforest, three years (2004 - 2006) of AMSR-E data, collected over a zone located between 2.5 degrees North and 5.0 degrees South in latitude, and 60.5 degrees West and 70.0 degrees West in longitude, were analyzed.

The Polarization Index (PI)

$$\mathbf{PI} = \frac{\mathbf{TB_v} - \mathbf{TB_h}}{0.5(\mathbf{TB_v} + \mathbf{TB_h})} \tag{A.1}$$

was selected as an indicator of vegetation thickness and it was used to identify within the large area the most stable zones. Two zones (1° x 1° degrees wide), covered by thick vegetation, were selected. These zones have an annual TB standard deviation lower than 0.50 K (see Table A.1, sixth row) and PI < 0.01 . Figure A.1 shows maps of TB standard deviation at 6.9 GHz and average PI for the three-year period. The selected stable areas are shown as white boxes.

Zone	1	1	1	1
Latitude	$[1, 2]$	$[1, 2]$	$[0, 1]$	$[0, 1]$
Longitude	$[-65.5°, -64.5°]$	$[-65.5°, -64.5°]$	$[-66.5°, -65.5°]$	$[-66.5°, -65.5°]$
Polarization	V	H	V	H
Mean Tb (K)	277.67	279.43	277.96	280.09
Std Tb (K)	0.43	0.44	0.46	0.44
Std Tb computed using ECMWF Soil Level 1 temperature (K)	0.43	0.42	0.34	0.35
Std Tb computed using ECMWF Skin temperature (K)	0.32	0.31	0.33	0.35

Table A.1: Mean and Tb standard deviation (std) in both polarizations (H and V) for the two zones

A first, simple calibration approach consists in assuming the TB value of selected zones to be constant, i.e. equal to the mean value computed over the three years. In this case, the fifth row of table A.1 gives the mean value (for the two zones and the two polarizations), while the sixth row gives the standard deviation, computed for the two zones and for the

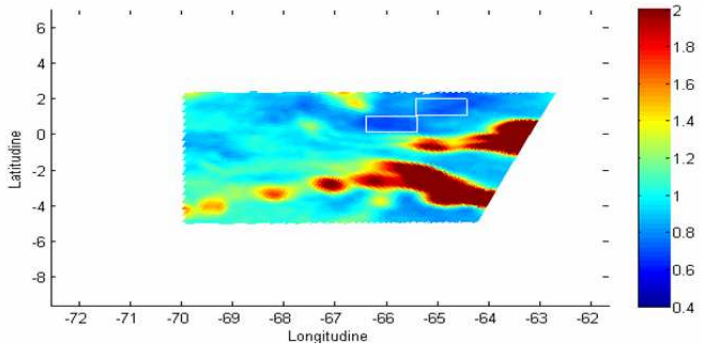

Figure A.1: Maps of Standard Deviation of Brightness Temperature (top) and Polarization Index (bottom) over the Amazon area derived from AMSR-E data at 6.9 GHz computed over a 3-years period (2004-2006). The white boxes show the two selected zones used for the statistical analysis in Table 4.2 and Table 4.3.

three-years, by taking the average value of TB as a reference. These values of std give an estimate of the calibration errors at C-band obtained when such a simple approach is adopted. A second, more advanced approach was based on the use of ECMWF data of Temperature, in order to improve the statistics. For both the two zones, a regression line between TB and ECMWF Temperature multitemporal values was first evaluated, and the residual std was then computed. The work was done by using both Soil Level 1 temperature (i.e. 7 cm depth) and skin temperature. The residual values of std are shown in Table A.1(seventh row for Soil level 1 temperature, and eighth row for Skin temperature). The improvement obtained by applying this approach is present in both H and V polarization. A better result is found if the skin temperature is used, and the total root mean square values for both areas are between 0.30 K and 0.33 K.

The third approach consisted in filtering the periodical trend recognized in the multitemporal (years 2004, 2005, 2006) values of TB. The multitemporal data were fitted by using an 8th grade polynomial. The periodical trend present in Figure A.2 is due to thermal cycle and leaf cycle during the year. The figure indicates that there is some yearly repeatability of TB's in the considered area. The residual values of standard deviation, after removing

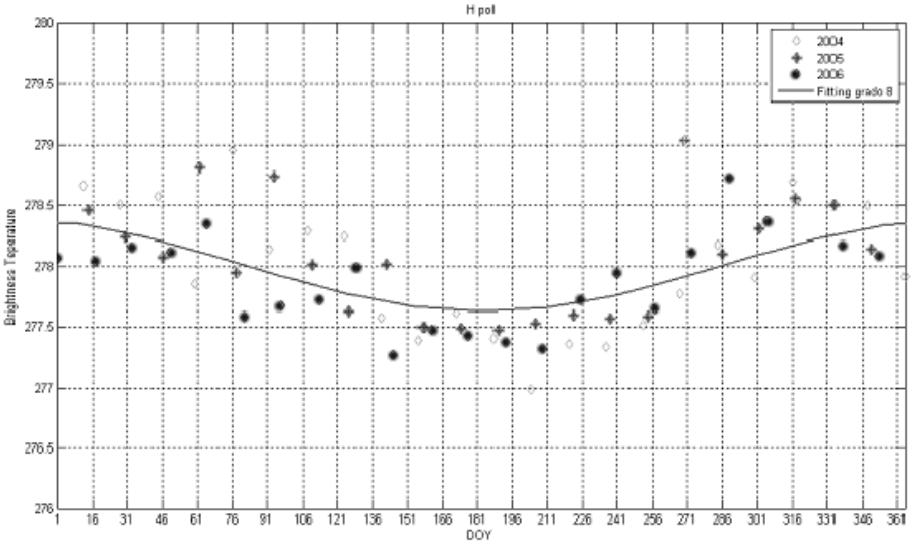

Figure A.2: Three-year annual trends (2004-2006) of AMSR-E brightness temperatures (K) at C band, H polarization and the 8th grade polynomial fitting (solid line)

this regular component, are shown in table A.2. Also these values are lower than the ones of Table A.1, especially at H polarization.

Residual Variability after Removing Periodic Component	
H	Std(Tb) = 0.30 K
V	Std(Tb) = 0.33 K

Table A.2: Tb standard deviation in both polarizations (H and V) for the two areas, after removing the periodic component.

Since L-Band spaceborne measurements are not available to assess the variability of the rain forest emission, the analysis performed on AMSR-E data at C-band has been extrapolated to L band by using the Tor Vergata model by Ferrazzoli and Guerriero [1996]. Main parameters required by the model are the wood-biomass, the leaf area index (LAI) and the soil moisture content (SMC).

A.2 Model simulations at L-Band

First, the emissivity of the rain forest at C-band has been estimated by running the model and comparing the model emissivity values with the AMSR-E ones. The a-priori values used

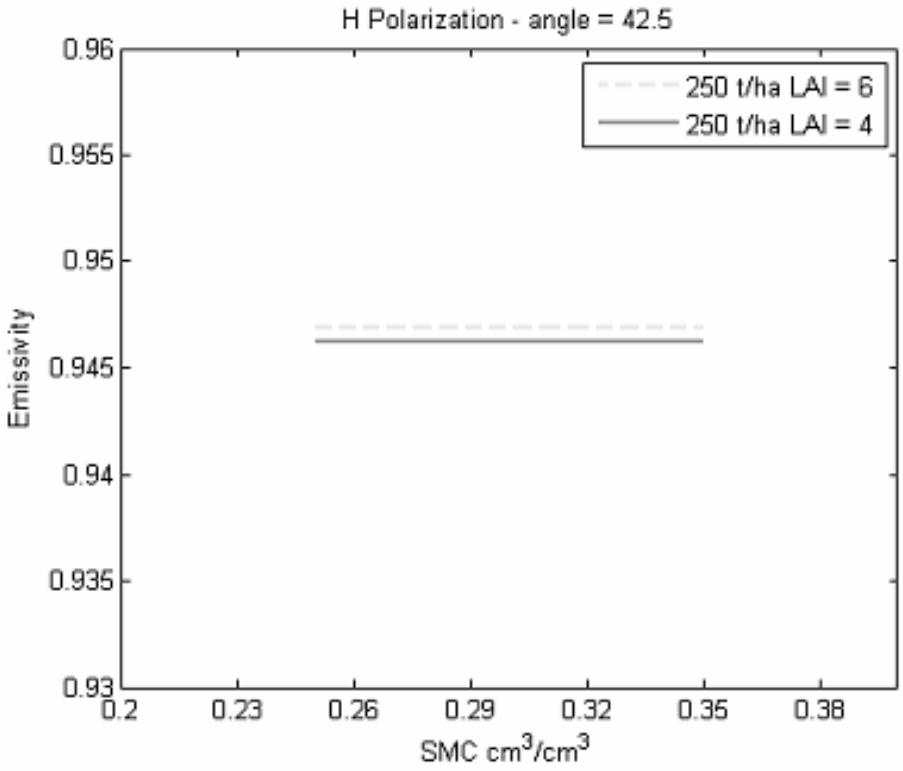

Figure A.3: Modelled emissivity at C band vs. soil moisture for LAI equal to 4 and 6, H polarization

for the input parameters are: woody biomass equal to 250 t/ha, LAI equal to 4 and 6, SMC in the range 25%-35%. These values were selected on the basis of ECMWF data of Soil Moisture over the considered zone and the forest structure and density. The results of the comparison between the model emissivity at H polarization and the emissivity computed from AMSR-E and ECMWF data are reported in Figures A.3 and A.4. In particular, Figure A.3 shows the simulated trend of emissivity vs. soil moisture for LAI equal to 4 and 6, at the AMSR-E frequency and viewing angle (55°). Figure A.4 shows, for the two selected zones, the multitemporal trends of emissivity, obtained as the ratio between measured brightness temperature and ECMWF skin temperature. The mean values of emissivity obtained from the Tor Vergata model and from the experimental data are close to each other, confirming both the good applicability of the model over the Amazon Rainforest. According to model simulations, emissivity variations due to changes in SMC and LAI at C band are low. Similar results have been obtained at V polarization.

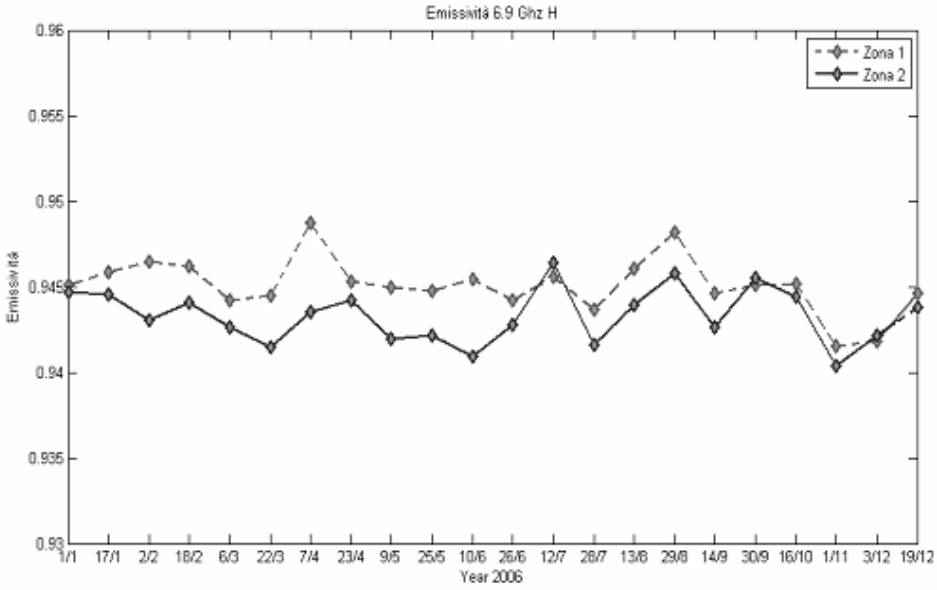

Figure A.4: Multitemporal trends of AMSR-E emissivity at C band, H polarization for the two selected zones.

Then, the model was run at L-band in order to analyse the emissivity variations due to the same LAI and SMC variations. Results, for an angle of 42.5° and at both polarizations, are shown in Figure A.5. It is found that realistic variations of LAI and soil moisture produce an emissivity variation of the order of 0.003 (corresponding to about ± 0.5 K).

The total variability of the TB's in the Amazon rainforest was estimated on the basis of the experimental data at C-band (AMSR-E) and the simulations at L-band. Two contributions were combined. The first contribution is equal to unpredictable variations observed in AMSR-E data, i.e. variations not related to periodic trends of temperature and LAI. We assume this component (E1) to be the same at L-band, and to be equal to the root mean square found in AMSR-E measurements. The second contribution (E2) is due to irregular and unpredictable variations related to SMC, which are negligible at C-band but can be appreciable at L-band, according to model simulations. The total error (ET) can then be expresses as:

$$\mathbf{E_T} = \sqrt{\mathbf{E_1^2} + \mathbf{E_2^2}} \tag{A.2}$$

The values of E1 are given in Table A.2, while E2 could be estimated from the performed simulations with Tor Vergata model (Figure A.5) considering LAI = 6 and an incidence angle of 42.5° by:

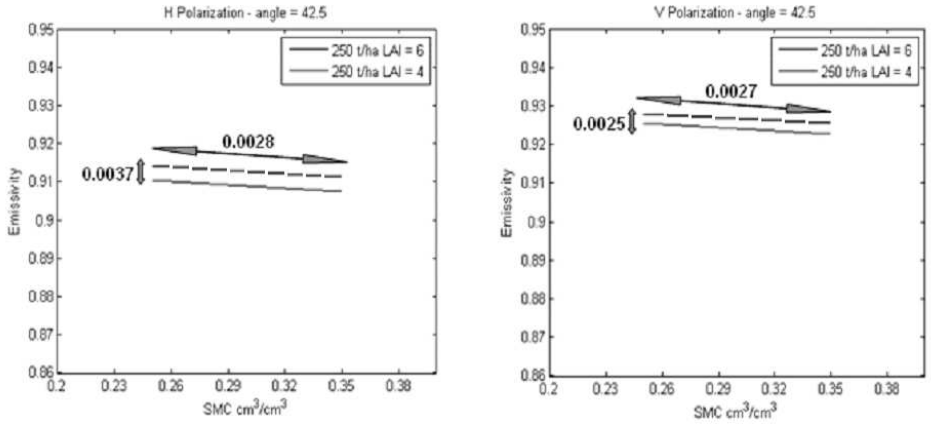

Figure A.5: Modelled emissivity at L band vs. soil moisture for LAI equal to 4 and 6 at H polarization (left panel) and V polarization (right panel).

The results are:

- TOTAL RMS ERROR = 0.50 K for H polarization
- TOTAL RMS ERROR = 0.48 K for V polarization

These estimated errors are below the instrument accuracy measured for the MIRAS instrument .

A.3 Conclusions

The Amazon Rain forest has been considered in this study as candidate target for the vicarious calibration of SMOS. Using C-band observed data, emissivity models, and previous studies available in the literature, the stability of the brightness temperature has been assessed and the effects of temporal variations can be partially reduced by using ECMWF information about temperature, or filtering the yearly periodic trend. The residual std of brightness temperature is below the SMOS instrument error.

Appendix B

Publications

B.1 Papers

- A.Della Vecchia, P. Ferrazzoli, L. Guerriero, R. Rahmoune, S. Paloscia, S. Pettinato, E. Santi, Modeling the multi-frequency emission of broadleaf forests and their components, IEEE Trans. Geoscience and Remote Sensing, vol. 42, pp. 260-272, 2010, doi: 10.1109/TGRS.2009.2029343.

- P. Ferrazzoli,R. Rahmoune, F.Moccia, F. Grings, M. Salvia, M. Barber, H. Karszenbaum, A. Soldano, D.Goniaski, G. Parmuchi, C. Montenegro, P. Kandus, M. Borro,The effect of rain and flooding events on AMSR-E signatures of La Plata Basin, Argentina IEEE Journal Of Selected Topics In Applied Earth Observations And Remote Sensing, March 2010, vol.3, n.1, pp. 81-90, 2010,doi:10.1109/JSTARS.2010.2040584.

- P. Ferrazzoli, L. Guerriero, N. Pierdicca, R. Rahmoune, Forest Biomass Monitoring with GNSS-R: Theoretical simulations Journal of Advanced Space Research (2010), doi:10.1016/j.asr.2010.04.025

- S.Pinori, R.Crapolicchio, M.Meloni, R.Rahmoune, P.Ferrazzoli, Soil Moisture and Ocean Salinity (SMOS) mission: system overview and contribution to vicarious calibration monitoring Italian journal of Remote Sensing, vol.40, n.1,2010.

B.2 Conference Proceedings

- J-P Wigneron , Y. Kerr , A. Mialon , N. Novello , F. Cabot , S. Delwart , F.Demontoux , M. J. Escorihuela , P. Ferrazzoli , A. Govind , J. P. Grant , D. Guyon, E. Jacquette , H. Lawrence , E. Lopez-Baeza, A. Mahmoodi, C. Mattar , S.Mecklenburg , C. Moisy, Sandra Monerris , R. Rahmoune, P. Richaume , P. de Rosnay , C. Rdiger , K. Saleh , M. Schwank , J. Sobrino, P. Waldteufel, "First evaluation of SMOS observations and Level-2 products over agricultural sites in temperate regions", The Third International Symposium on Recent Advances in Quantitative Remote Sensing, 27 September-1 October 2010, Valencia, Spain.

- R. Rahmoune, P. Ferrazzoli, L. Guerriero, "Development and refinement of a forest Emission Model comparisons tests with SMOS signatures", URSI-F 2010 Microwave Signatures Meeting, Florence, Italy, 4-8 October 2010.

- R. Chakraborty, R.Rahmoune, P. Ferrazzoli, "Monitoring flood events in Sundarban delta by microwave instruments", URSI-F 2010 Microwave Signatures Meeting, Florence, Italy, 4-8 October 2010.

- P. Ferrazzoli, L. Guerriero, R. Rahmoune, "RECENT ADVANCES IN THEORETICAL STUDIES OF L-BAND ACTIVE AND PASSIVE REMOTE SENSING OF FORESTS", International Geoscience and Remote Sensing Symposium, Hawaii, USA, 25-30 July 2010.

- M. Salvia, F. Grings, P. Ferrazzoli, R. Rahmoune, M. Barber, V. Douna, H. Karszenbaum, "MONITORING FLOODED AREA FRACTION IN FLOODPLAINS OF PARAN BASIN USING PASSIVE AND ACTIVE MICROWAVE SYSTEMS", International Geoscience and Remote Sensing Symposium, Hawaii, USA, 25-30 July 2010.

- Haydee Karszenbaum, Francisco Grings, Mercedes Salvia, Pablo Perna, Vanesa Douna, Vernica Barraza, Rachid Rahmoune, Paolo Ferrazzoli, "AMSR-E and Preliminary SMOS Observations of Vegetated Areas of La Plata Basin", Aquarius / SAC-D Science Team Meeting, July 1921, 2010, Bell Harbor International Conference Center, Seattle, Washington USA

- R. Rahmoune, P. Ferrazzoli, F. Grings, V. Douna, M. Salvia, H. Karszenbaum, "Sensitivity to soil moisture variations of microwave radiometric signatures over the Argentinian Chaco Forest", ESA living planet symposium, bergen, Norway, 28 June to 2 July 2010.

- R. Rahmoune, P. Ferrazzoli, M. Salvia, F. Grings, V. Douna, H. Karszenbaum, "Monitoring flooded areas in floodplains of Paran basin using microwave REMOTE SENSING", European Geosciences Union General Assembly, 02 07 May 2010, Vienna, Austria.

- R. Rahmoune, P. Ferrazzoli, J.P. Walker, J.P. Grant, "L-BAND EMISSION FROM A EUCALYPTUS FOREST IN VARIOUS SOIL CONDITIONS DURING THE NAFE CAMPAIGN", 11th Specialist Meeting on Microwave Radiometry and Remote Sensing of the Environment, Washington, DC, USA, 1-4 March 2010.

- P. Ferrazzoli, L. Guerriero, R. Rahmoune, A. Della Vecchia, "MODELING FOREST EMISSION: ELECTROMAGNETIC APPROXIMATIONS, TESTS, AND APPLICATION TO RETRIEVAL ALGORITHMS", 11th Specialist Meeting on Microwave Radiometry and Remote Sensing of the Environment, Washington, DC, USA, 1-4 March 2010.

- P. Ferrazzoli, R. Rahmoune, F. Grings, V. Douna, M. Salvia, H. Karszenbaum, "AMSR-E observations of rain and flood events over vegetated areas of La Plata Basin ", 11th Specialist Meeting on Microwave Radiometry and Remote Sensing of the Environment, Washington, DC, USA, 1-4 March 2010.

- R. Rahmoune, P. Ferrazzoli, F. Grings, M. Salvia, V. Douna, H. Karszenbaum, A. Soldano, D.Goniaski, G. Parmuchi, C. Montenegro, P. Kandus, M. Borro,AMSR-E observations of La plata Basin: interpretation using ancillary data and emission models, Earth Observation and Water Cycle Science Towards a Water Cycle Multi-mission Observation Strategy, 18 - 20 November 2009, ESA/ESRIN, Frascati, Italty.

- P. Ferrazzoli, R. Rahmoune, F. Grings, V. Douna, M. Salvia, H. Karszenbaum, "Sensitivity to soil moisture variations of AMSR-E C-Band Polarization Index over Chaco Forest", 5th Aquarius/SAC-D Science Meeting, Buenos Aires, Argentina, 21- 23 October 2009.

- R. Rahmoune, A. Della Vecchia, P. Ferrazzoli, L. Guerriero, F. Martin-Porqueras, A Large Scale Microwave Emission Model For Forests Contribution to the SMOS Algorithm, Workshop on SMOS-BEC on SMOS post-launch activities, 5 June 2009, Barcelona, Spain.

- P. Ferrazzoli, R. Rahmoune, F. Grings, M. Salvia, M. Barber, H. Karszenbaum, A. Soldano, D. Goniaski, G. Parmuchi, C. Montenegro, P. Kandus, M. Borro, Monitoring Rain and Flooding Events In De LA PLATA Basin Using AMSR-E Signatures, International Geoscience and Remote Sensing Symposium, Cape Town, South Africa, July 13-17, 2009.

- R. Rahmoune, A. Della Vecchia, P. Ferrazzoli, L. Guerriero, F. Martin-Porqueras, Refinements and tests of Microwave Emission Model for Forests, International Geoscience and Remote Sensing Symposium, Cape Town, South Africa, July 13-17, 2009.

- R. Rahmoune, A. Della Vecchia, P. Ferrazzoli, L. Guerriero, F. Martin-Porqueras, A Large Scale Microwave Emission Model For Forests Contribution to the SMOS Algorithm, European Geosciences Union General Assembly 2009, 19 24 April 2009, Vienna, Austria.

- R. Crapolicchio, S. Pinori, M. Meloni,R. Rahmoune, P. Ferrazzoli, A contribution to the vicarious routine calibration monitoring for the Soil Moisture and Ocean Salinity (SMOS) mission, European Geosciences Union General Assembly 2009, 19 24 April 2009, Vienna, Austria.

- S. Paloscia, P.Pampaloni, E. Santi, S. Pettinato, P. Ferrazzoli, R.Rahmoune, The effects of forest canopies and of the underlying soil moisture on microwave emission, European Geosciences Union General Assembly 2009, 19 24 April 2009, Vienna, Austria.

- R.Rahmoune, A. Della Vecchia, P.Ferrazzoli, L.Guerriero, Analisi Parametrica DellEmissione di Foreste In Banda L, Riunione Nazionale di Elettromagnetismo, Lecce, 15-19 Settembre 2008.

- R.Rahmoune,P. Ferrazzoli, Monitoring of level 1c brightness temperatures measured over Finland, AMIRAS flight , ESA/ESTEC Internal comunication, 23rd SMOS SAG meeting, Noordwijk, Netherlands, 21-22 May 2008.

- A. Della Vecchia, P. Ferrazzoli, L. Guerriero, R. Rahmoune,S. Paloscia, S. Pettinato, E. Santi, "Modeling the multifrequency emission of forests and their components", International Geoscience and Remote Sensing Symposium, Boston (USA), July 6-11, 2008.

- A. Della Vecchia, P. Ferrazzoli, L. Guerriero, R. Rahmoune, S. Paloscia, S. Pettinato, E. Santi, "Modeling the emission of Medirerranean forests and comparisons with experimental data", 10th Specialist Meeting on Microwave Radiometry and Remote Sensing of the Environment, Florence, 11- 14March2008.

Bibliography

[1] Abril, A., and Bucher, E. H.. **Overgrazing and soil carbon dynamics in the western Chaco of Argentina**. *Applied Soil Ecology, vol. 16, pp. 243-249*, 2001.

[2] Bartelink, H.H.. **Allometric relationships for biomass and leaf area of Beech (Fagus sylvatica L.)**. *Annals of Forest Science, 54(1), 3950*, 1997.

[3] Bartolozzi, L., I. Bovini, R. Boretti, F. Bussotti, E. Cenni, A. Chiarucci, A. Cozzi, V. De Dominicis, M. Ferretti, P. Grassoni, G. Landi, C. Leonzio,and G. Vignozzi,. **Forest ecosystem monitoring in Tuscany (Italy): Past activities, present status and future perspectives**. *J. Limnol., vol. 61, pp. 129136*, 2002.

[4] Berger, M. , Y. Kerr, J. Font, J.-P. Wigneron, J.-C. Calvet, K. Saleh, E. Lopez-Baeza, L. Simmonds, P. Ferrazzoli, B. van de Hurk, P. Viterbo, P. Waldteufel, F. Petitcolin, A. van de Griend, E. Attema, and M. Rast. **Measuring the moisture in the earth's soil–Advancing the science with ESA's SMOS mission**. *ESA Bull., vol. 115, pp. 4145*, 2003.

[5] Borchert, R.. **Soil and stem water storage determine phenology and distribution of tropical dry forest trees**. *Ecology 75, 1437-1449*, 1994.

[6] Cannell, M. G. R.. **Ed., World Forest Biomass and Primary Production Data**. *Academic, New York*, 1982.

[7] Champeaux, J., Kyung-Soo, H., Arcos, D., Habets, F., and Masson, V.. **Eco-climap II: A new approach at global and european scale for ecosystems mapping and associated surface parameters database using SPOT/VEGETATION data - first results**. *JProceedings of IGARSS* , 2004.

[8] Chauhan, N. S., R. H. Lang, and K. J. Ranson. **Radar modeling of a boreal forest**. *IEEE Trans. Geosci. Remote Sens., vol. 29, no. 4, pp. 627638*, 1991.

[9] Chiarucci, A., I. Bonini, and V. De Dominicis. **Vascular plant density**. *in Program MON.I.TO. (Monitoraggio Intensivo delle Foreste Toscane) Concepts, Structure and 1995 Results, Paper n.5 of the Monito Program, L. Bartolozzi, F. Bussotti, V. De Dominicis, and M. Ferretti, Eds. Bologna, Italy: Regione Toscana*, 1996.

[10] Choudhury, B.J.. **Monitoring global land surface using Nimbus-7 37 GHz data, theory and examples**. *International Journal of Remote Sensing, 10: 1579-1605*, 1989.

[11] Cozzi, A.. **Monitoring sites**. *in Program MON.I.TO. (Monitoraggio Intensivo delle Foreste Toscane) Concepts, Structure and 1995 Results, Paper n.5 of the Monito Program, L. Bartolozzi, F. Bussotti V. De Dominicis, and M. Ferretti, Eds. Bologna, Italy: Regione Toscana* , 1996.

[12] Della Vecchia, A., Saleh, K., Ferrazzoli, P., Gurriero, L. and Wigneron, J.-P.. **Simulating L-Band Emission of Coniferous Forests Using a Discrete Model and a Detailed Geometrical Representation.**. *IEEE Geoscience and Remote Sensing Letters, 3(3), 364-368.*, 2006a.

[13] Della Vecchia, A., Ferrazzoli, P., Giorgio, F. and Guerriero, L.. **A large scale approach to estimate L band emission from forest covered surfaces. Second Recent Advances in Quantitative Remote Sensing,** . *Jos A. Sobrino (Ed.), Servicio de Publicaciones, Universitat de Valencia, 925-930*, 2006b.

[14] Della Vecchia, A., Ferrazzoli, P., Wigneron, J.-P. and Grant, J.P.. **Modeling forest emissivity at L-band and a comparison with multitemporal measurements** . *IEEE Geoscience and Remote Sensing Letters, 4(4), 508-512.*, 2007.

[15] Della Vecchia, A.; Ferrazzoli, P.; Guerriero, L.; Rahmoune, R.; Paloscia, S.; Pettinato, S.; Santi, E.. **Modeling the Multifrequency Emission of Broadleaf Forests and Their Components**. *Geoscience and Remote Sensing, IEEE Transactions on ,vol.48, no.1, pp.260-272*, 2010.

[16] Droesen, W. J., D. H. Hoekman, H. J. C. van Leeuwen, J. J. van der Sanden, S. A. M. Bouman, D. Uenk, M. A. M. Vissers, and G. G. Lemoine. **MAESTRO 89 ground data collection Hosterwold/Speulderbos/Flevoland**. *Wageningen Agric. Univ., Wageningen, The Netherlands, Tech. Rep.*, 1989.

[17] Dobson, M.C., Ulaby, F.T., Hallikainen, M.T. and El-Rayes, M.A.. **Microwave Dielectric Behaviour of Wet Soil Part II: Dielectric Mixing Models**. *IEEE Transactions on Geoscience and Remote Sensing, 23, 35-46.*, 1985.

[18] Eom, H. and Fung, A.. **A scatter model for vegetation up to Ku-band**. *Remote Sensing of the Environment, 15:185200*, 1984.

[19] Ferrazzoli, P. and Guerriero, L.. **Passive microwave remote sensing of forests: a model investigation.**. *IEEE Transactions on Geoscience and Remote Sensing, 34(2), 433-443.*, 1996.

[20] Ferrazzoli, P., Guerriero, L. and Wigneron, J.-P.. **Simulating L-Band Emission of Forests in View of Future Satellite Applications.**. *IEEE Transactions on Geoscience and Remote Sensing, 40(12), 2700-2708.*, 2002.

[21] Ferrazzoli, P., Rahmoune, R., Grings, F. Douna, V., Parmuchi, G., Salvia, M., and Karszenbaum, H.. **AMSR-E observations of rain and flood events over vegetated areas of La Plata Basin**. *Proceedings of Microrad 2010 Symposium, Washington.*, 2010.

[22] Ferrazzoli, P., Rahmoune, R., F. Moccia, F. Grings, M. Salvia, M. Barber, H. Karszenbaum, A. Soldano, D. Goniadzki, G. Parmuchi , C. Montenegro, P. Kandus, M. Borro . **The effect of rain and flooding events on AMSR-E signatures of La Plata Basin, Argentina**. *IEEE Journal of Selected Topics in Earth Observations and Remote Sensing, doi: 10.1109/JSTARS.2010.2040584* , 2010.

[23] Fung, A.K.. **Microwave Scattering and Emission Models and Their Applications**. *Artech House, Norwood (USA).*, 1994.

[24] Gasparri, N.. **Efecto del cambio de uso de la tierra sobre la cobertura vegetal y la dinmica de biomasa del chaco semirido Argentino**. *PhD Thesis. Universidad Nacional de Tucumn, Argentina*, 2010.

[25] Gimnez, A. M., Moglia, J. G. **rboles del Chaco Argentino: gua para el reconocimiento dendrolgico**. *UNSE-SAyDS. Santiago del Estero,Argentina*, 2003.

[26] Grant, J.P., Wigneron, J.-P., Van de Griend, A.A., Kruszewski, A., Schmidl Sbjrg, S. and Skou, N.. **A field experiment on microwave forest radiometry: L-band signal behaviour for varying conditions of surface wetness**. *Remote Sensing of Environment, 109(1), 10-19*, 2007.

[27] Grant, J.P., Saleh, K., Wigneron, J.-P., Guglielmetti, M., Kerr, Y., Schwank, M., Skou, N. and Van de Griend, A.A.. **Calibration of the L-MEB model over a coniferous and a deciduous forest**. *IEEE Transactions on Geoscience and Remote Sensing, 46(3), 808-818.*, 2008.

[28] Grant, J.P., Van de Griend, A.A., Schwank, M. and Wigneron, J.-P.. **Observations and Modelling of a Pine Forest Floor at L-Band**. *IEEE Transactions on Geoscience and Remote Sensing, in press*, 2009.

[29] Guglielmetti, M., Schwank, M., Mtzler, C., Oberdrster, C., Vanderborght, J. and Flhler, H.. **Measured microwave radiative transfer properties of a deciduous forest canopy**. *Remote Sensing of Environment, 109(4), 523-532*, 2007.

[30] Guglielmetti, M., Schwank, M., Mtzler, C., Oberdrster, C., Vanderborght, J. and Flhler, H.. **FOSMEX: Forest Soil Moisture Experiments with Microwave Radiometry**. *IEEE Transactions on Geoscienxe and Remote Sensing, 46(3), 727-735* , 2008.

[31] Hallikainen, M. T., P. A. Jolma, and J. M. Hyyppa. **Satellite microwave radiometry of forest and surface types in Finland**. *IEEE Trans. Geosci. Remote Sens., vol. 26, no. 5, pp. 622628*, 1988.

[32] Jackson, T.J. and O'Neill, P.E.. **Attenuation of soil microwave emissivity by corn and soybeans at 1.4 and 5 GHz**. *IEEE Transactions on Geoscience and Remote Sensing, 28, 978-980*, 1990.

[33] Jackson, T.J. and Schmugge, T.J.. **Vegetation Effects on the Microwave Emission of Soils**. *Remote Sensing of Environment, 36, 203-212*, 1991.

[34] Jackson, T., Schmugge, T., and Wang, J.. **Passive microwave sensing of soil-moisture under vegetation canopies**. *Water Resources Research, 18:11371142*, 1982.

[35] Jenkins, J., Chojnacky, D., Heath, L., and Birdsey, R.. **Comprehensive database of diameter-based biomass regressions for north american tree species. Technical report, United States Department of Agriculture**. *http://www.fs.fed.us/ne. General Technical Report NE-319*, 2004.

[36] Jenkins, J. C., Chojnacky, D., Heath, L. S., and Birdsey, R. A.. **National-scale biomass estimators for united states tree species**. *Forest Science, 49:1226*, 2003.

[37] Karam, M. A., A. K. Fung, R. H. Lang, and N. S. Chauhan. **A microwave scattering model for layered vegetation**. *IEEE Trans. Geosci. Remote Sens., vol. 30, no. 4, pp. 767784*, 1992.

[38] Karam, M. A.. **A physical model for microwave radiometry of vegetation**. *IEEE Trans. Geosci. Remote Sens., vol. 35, no. 4, pp. 1045-1058*, 1997.

[39] Kasischke, E. S., N. L. Christensen, and E. M. Haney. **Modeling of geometric properties of loblolly pine tree stand characteristics for use in radar backscatter studies**. *IEEE Trans. Geosci. Remote Sens., vol. 32, no. 4, pp. 800-822*, 1994.

[40] Kerr, Y.H., Waldteufel, P., Wigneron, J.-P., Martinuzzi, J.-M., Font, J. and Berger, M.. **Soil Moisture Retrieval from Space: The Soil Moisture and Ocean Salinity (SMOS) Mission**. *IEEE Transactions on Geoscience and Remote Sensing, 39(8), 1729-1735*, 2001.

[41] Kerr, Y.H., Waldteufel, P., Richaume, P., Davenport, I., Ferrazzoli, P. and Wigneron, J.-P.. **SMOS Level 2 Processor for Soil Moisture, Algorithm Theoretical Based Document (ATBD). CESBIO, IPSL-Service d'Aronomie, INRA-EPHYSE, Reading University, Tor Vergata University**. *SO-TN-ESL-SM-GS-0001 Issue 3.a*, 2007.

[42] Kerr, Y.H, and E. G. Njoku. **A Semiempirical Model For Interpreting Microwave Emission From Semiarid Land Surfaces as Seen From Space**. *IEEE Trans. Geosci.Remote Sensing, vol. 28, pp. 384-393*, 1990.

[43] Kirdyashev, K.P., Chukhlantsev, A.A. and Shutko, A.M.. **Microwave radiation of the earth's surface in the presence of vegetation cover**. *Radiotekhnika, 24, 256-264* , 1979.

[44] Kruopis, N., J. Praks, A. N. Arslan, H. M. Alasalmi, J. T. Koskinen, and M. T. Hallikainen. **Passive microwave measurements of snow-covered forest areas in EMAC'95**. *IEEE Trans. Geosci. Remote Sens., vol. 37, no. 6, pp. 2699-2705*, 1999.

[45] Lang, R.H., P. de Matthaeis, D. M. LeVine, S. Bidwell, M. Haken, and N. Chauhan. **L-band radiometer measurements of coniferous forests**. *in Proc. Int. Geosci. Remote Sens. Symp., Honolulu, HI, pp. 1930-1932*, 2000.

[46] Lang, R.H., Utku, C., De Matthaeis, P., Chauhan, N. and Le Vine, D.M.. **ESTAR and Model Brightness temperatures over forests: effects of soil moisture**. *Proceedings of IGARSS 2001, IEEE International, 3, 1300-1302*, 2001.

[47] Macelloni, G., Paloscia, S., Pampaloni, P. and Ruisi, R.. **Airborne multifrequency L- to Ka-band radiometric measurements over forests**. *IEEE Transactions on Geoscience and Remote Sensing, 39(11), 2507-2513*, 2001.

[48] Macelloni, G., S. Paloscia, P. Pampaloni, R. Ruisi, and E. Santi. **Microwave radiometric features of Mediterranean forests: Seasonal variations** . *in Proc. Int. Geosci. Remote Sens. Symp., Toulouse, France, Jul. 21-25, 2003, vol. 3, pp. 16341636*, 2003.

[49] Martin-Neira, M., I. Cabeza, C. Prez, M. A. Palacios, M. A. Guijarro, S. Rib, I. Corbella, S. Blanch, F. Torres, N. Duffo, V. Gonzlez, S. Beraza,A. Camps, M. Vall-llossera, S. Tauriainen, J. Pihlflyckt, J. P. Gonzlez, and F. Martin-Porqueras . **AMIRAS–An Airborne MIRAS Demonstrator**. *IEEE Trans. Geosci.Remote Sensing, vol. 46, pp.705-716*, 2008.

[50] Mtzler, C.. **Seasonal Evolution of Microwave Radiation from an Oat Field**. *Remote Sensing of Environment, 31, 161-173*, 1990.

[51] Mtzler, C.. **Microwave Transmissivity of a Forest Canopy: Experiments Made with a Beech**. *Remote Sensing of Environment, 48, 172-180*, 1994a.

[52] Mtzler, C.. **Passive Microwave Signatures of Landscapes in Winter** . *Meteorology and Atmospheric Physics, 54, 241-260*, 1994b.

[53] Mtzler, C., Weber, D., Wthrich, M., Schneeberger, K., Stamm, C. and Flhler, H.. **ELBARA, the ETH L-band radiometer for soil moisture research**. *Proceedings of IGARSS 2003, IEEE International, 5, 3058-3060.*

[54] Mtzler, C. (Ed.), Rosenkranz, P.W., Battaglia, A. and Wigneron, J.-P.. **Thermal Microwave Radiation: Applications for Remote Sensing**. *IET Electromagnetic Waves Series 52, London, UK*, 2006.

[55] Njoku, E. G., T. L. Jackson, V. Lakshmi, T. Chan, and S.V. Nghiem.. **Soil Moisture Retrieval from AMSR-E**. *IEEE Transactions on Geoscience and Remote Sensing 41 (2): 215-229*, 2003.

[56] Paloscia, S and P. Pampaloni. **Microwave polarization index for monitoring vegetation growth**. *IEEE Trans. Geosci. Remote Sens., vol. 26, pp. 617621*, 1988.

[57] Paloscia, S, G. Macelloni, E. Santi, and T. Koike. **A multifrequency algorithm for the retrieval of soil moisture on a large scale using microwave data from SMMR and SSM/I satellites**. *IEEE Trans. Geosci. Remote Sens., vol. 39, pp. 1655-1661*, 2001.

[58] Paloscia, S., Pampaloni, P., Santi, E., Pettinato, S., Della Vecchia, A., Ferrazzoli, P. and Guerriero, L.. **Soil moisture effect on microwave emission of forest canopies**. *Proceedings of MICRORAD 2008, Microwave Radiometry and Remote Sensing of the Environment, 1-4*, 2008.

[59] Pampaloni, P.. **Microwave radiometry of forests**. *Waves in Random Media, 14, S275-S298*, 2004.

[60] Panciera, R., Walker, .P., Kalma, J.D., Kim, E.J., Hacker, J., Merlin, O., Berger, M. and Skou, N.. **The NAFE'05/CoSMOS data set: Towards SMOS soil moisture retrieval, downscaling and assimilation**. *IEEE Transactions on Geoscience and Remote Sensing, 46(3), 736-745*, 2008.

[61] Pellarin, T., Wigneron, J.-P., Calvet, J.-C., Berger, M., Douville, H., Ferrazzoli, P., Kerr, Y., Lopez-Baeza, E., Pulliainen, J., Simmonds, L. and Waldteufel, P.. **Two-Year Global Simulation of L-Band Brightness Temperatures Over Land**. *IEEE Transactions on Geoscience and Remote Sensing, 41(9), 2135-2139*, 2003a.

[62] Rahmoune, R., Ferrazzoli, P., Walker, J. P., and Grant, J. P.. **L-band emission from a Eucalyptus forest in various soil conditions during the NAFE campaign**. *Proceedings of Microrad 2010 Symposium, Washington*, 2010.

[63] Rahmoune, R., Della Vecchia, A., P. Ferrazzoli, L. Guerriero,F. Martin-Porqueras. **Refinements and tests of a microwave emission model for forests**. *in Proc of 2009 International Geoscience and Remote Sensing Symposium, Cape Town*, 2009.

[64] Saleh, K., Port, A., Guyon, D., Ferrazzoli, P. and Wigneron, J.-P.. **A forest geometric description of a Maritime Pine forest suitable for discrete microwave models**. *IEEE Transactions on Geoscience and Remote Sensing, 43(9), 2024-2034*, 2005.

[65] Santi, E., Paloscia, S., Pampaloni, P., and Pettinato, S.. **Ground-Based Microwave Investigations of Forest Plots in Italy**. *IEEE Trans. Geosci. Remote Sens., vol. 47, pp. 3016-3025.*, 2009.

[66] Schmugge, T.J., Wang, J.R. and Asrar, G.. **Results from the Push Broom Microwave Radiometer Flights over the Konza Prairie in 1985**. *IEEE Transactions on Geoscience and Remote Sensing, 26(5), 590-596*, 1988.

[67] Schmugge, T.J. and Jackson, T.J.. **Observations of coherent emissions from soils**. *Radio Science, 33(2), 267-272*, 1988.

[68] Schwank, M., Guglielmetti, M., Mtzler, C. and Flhler, H.. **Testing a New Model for the L-band Radiation of Moist Leaf Litter**. *IEEE Transactions on Geoscience and Remote Sensing, 46(7), 1982-1994*, 2008.

[69] Shutko, A. M., and A. A. Chukhlantsev. **Microwave radiation peculiarities of vegetative covers**. *IEEE Trans. Geosci. Remote Sens., vol. GRS-20, no. 1, pp. 27-29*, 1982.

[70] Teng, W. L., J. R. Wang, and P. C. Doraiswamy. **Relationship between satellite microwave radiometric data, antecedent precipitation index, and regional soil moisture**. *Int. J. Remote Sens., vol. 14, no. 13, pp. 2483-2500*, 1995.

[71] Ulaby, F., Moore, R. and Fung, A.. **Microwave Remote Sensing: Active and Passive**. *Vol. III: from Theory to Applications. Artech House, Dedham, MA*, 1986.

[72] Ulaby, F., K. Sarabandi, K. McDonald, M. Whitt, and M. C. Dobson . **Michigan microwave canopy scattering model**. *Int. J. Remote Sens., vol. 11, no. 7, pp. 1223-1253*, 1990.

[73] Yoshinobu Sato, Tomo'omi Kumagai, Atsushi Kume, Kyoichi Otsuki, Shigeru Ogawa. **Experimental analysis of moisture dynamics of litter layers - the effects of rainfall conditions and leaf shapes**. *Hydrological Processes, vol. 18, pp. 3007-3018*, 2004.

[74] Wang, J.R. and Choudhury, B.J.. **Remote sensing of soil moisture content over bare field at 1.4 GHz frequency**. *Journal of Geophysical Research, 86, 5277-5282*, 1981.

[75] Wigneron, J.-P., D. Guyon, J.-C. Calvet, G. Courrier, and N. Bruguier. **Monitoring coniferous forest characteristics using a multifrequency (5-90 GHz) microwave radiometer**. *Remote Sens. Environ., vol. 60, no. 3, pp. 299-310*, 1997.

[76] Wigneron, J.-P., Kerr, Y.H., Waldteufel. P., Saleh, K., Escorihuela, M.-J., Richaume, P., Ferrazzoli, P., de Rosnay, P., Gurney, R., Calvet, J.-C., Grant, J.P., Guglielmetti, M., Hornbuckle, B., Mtzler, C., Pellarin, T. and Schwank, M. . **L-band Microwave Emission of the Biosphere (L-MEB)**

Model: description and calibration against experimental data sets over crop fields.. *Remote Sensing of Environment, 107(4), 639-655*, 2007.

[77] Wilheit, T.T.. **Radiative Transfer in a Plane Stratified Dielectric**. *IEEE Transactions on Geoscience and Remote Sensing, 16(2), 138-143*, 1978.

Declaration

I herewith declare that I have produced this paper without the prohibited assistance of third parties and without making use of aids other than those specified; notions taken over directly or indirectly from other sources have been identified as such. This paper has not previously been presented in identical or similar form to any other Italian or foreign examination board.

The thesis work was conducted from October 2007 to December 2010 under the supervision of Professor Paolo Ferrazzoli and Professor Leila Guerriero at the Department of Computer Science, Systems an Production, Rome Tor Vergata University.

ROME,